Electrocaloric coolers based on ceramic multilayer capacitors

by

Alvar Torello Massana

A dissertation presented to the University of Luxembourg
for the degree of Doctor of Philosophy
in Physics and Material Sciences

Belval, Luxembourg, 2022

Examining Committee Membership

The following served on the Examining Committee for this thesis. The decision of the Examining Committee is by majority vote.

External Members	Dr. Jaka Tusek Assistant Profesor at Faculty of Mechanical Engineering University of Ljubljana
	Dr. Xiaoshi Qian Associate Professor, Department of Mechanical Engineering Shanghai Jiao Tong University
	Dr. Xavier Moya Assistant professor, Department of Material Science and Metallurgy University of Cambridge
Internal Members	Dr. Massimiliano Esposito Full professor in Theoretical Physics, Faculty of Science, Technology and Medicine University of Luxembourg
Supervisor	Dr. Emmanuel Defay Head of Unit Nanotechnology, Department of Material Research and Technology Luxembourg Institute of Science and Technology

Author's Declaration

I hereby declare that I am the sole author of this thesis. This is a true copy of the thesis, including any required final revisions, as accepted by my examiners.

I understand that my thesis may be made electronically available to the public.

Abstract

The following work investigates the development of heat pumps that exploit electrocaloric effects in Pb(Sc,Ta)0_3 (PST) multilayer capacitors (MLCs). The electrocaloric effect refers to reversible thermal changes in a material upon application (and removal) of an electric field. Electrocaloric cooling is interesting because 1) it has the potential to be more efficient than competing technologies, such as vapour-compression systems, and 2) it does not compel the use of greenhouse gases, which is crucial in order to slow down global warming and mitigate the effects of climate change.

The continuous progress in the field of electrocalorics has promoted the creation of several electrocaloric based heat pump prototypes. Despite the different designs and working principles utilized, these prototypes have struggled to maintain temperature variations as large as 10 K, discouraging their industrial development. In this work, bespoke PST-MLCs exhibiting large electrocaloric effects near room temperature were embodied in a novel heat pump with the motivation to surpass the 10 K-barrier. The experimental design of the heat pump was based on the outcome of a numerical model. After implementing some of the modifications suggested by the latter, consistent temperature spans of 13 K around 30 °C were reported, with cooling powers of 12 W kg^{-1}. Additional simulations predicted temperature spans as large as 50 K and cooling powers in the order of 1000 W kg^{-1}, if a new set of plausible modifications were to be put in place.

Similarly, these very same PST-MLCs samples were implemented into pyroelectric harvesters revisiting Olsen's pioneering work from 1980. The harvested energies were found to be as large as 11.2 J, with energy densities reaching up to 4.4 J cm^{-3} of active material, when undergoing temperature oscillations of $\sim$ 100 K under electric fields applied of 140 – 200 kV cm^{-1}. These findings are two and four times, respectively, larger than the best reported values in the literature.

The results obtained in this dissertation are beyond the state-of-the-art and show that 1) electrocaloric heat pumps can indeed achieve temperature spans larger than 10 K, and 2) pyroelectric harvesters can generate electrical energy in the Joule-range. Moreover, numerical models indicated that there is still room for improvement, especially when it comes to the power of these devices. This should encourage the development of these kinds of electrocaloric- and pyroelectric-based applications in the near future.

Acknowledgements

First and foremost, I would like to thank my thesis supervisor Emmanuel Defay, for what has been a very enjoyable and memorable road. I still remember how excited I was after you introduced me to the topic the first time we met. Thanks for having fueled my motivation throughout these years. Above all, I thank you for your guidance, mentoring and dedication. Being your student has resulted very easy and smooth. Thanks Manu for everything.

Secondly, I would like to thank Sakyo Hirose and his team in Murata Manufacturing, for his generosity and assistance in supplying all these PST-MLCs to us. Without these incredible samples, all this work could have not been possible. On a personal note, I would like to thank Sakyo for encouraging me to attend the MRS fall exhibition in Boston 2018 when I was still a master student. This experience was a game-changer and meant a lot to me.

I would also like to thank my beloved EC team members, with whom I shared almost everything that happened either in the office or in the lab, for their team spirit and friendship.

- To Youri, who has been the best companion I could have imagined. Thanks for your work ethics and dynamics, for bringing always a smile to work. And thanks as well for all the moments we shared, the “Mocktels” at Coyote, the million tennis classes... it has been a real pleasure.
- To Pierre, from whom I learnt tons (and not always at a work level), for his “colossal” help and assistance in the automatising of measurements and set-ups, but also for his always appreciated scientific insights and comments.
- To Veronika, for her kindness, dedication and discipline. Working with you has been easy at the same time than enjoyable and exciting. Thanks for all the discussions (professional and personal) that we had over the last two years.
- To Romain, who taught me almost everything in the lab when I first arrived. We only worked together for a year, but your assistance, support and mentoring meant a lot.
- To Uros, Ashwath and Junning, for all the discussions and assistance in the different experiments that we performed together.

More broadly, I would like to thank all my group colleagues from FMT: to Cosme, Christina, Naveen, Sanguita, Alfredo, Hugo, Constance, Carlos and many more. Thanks for all these moments we spent together in the canteen, conferences, summer schools, after-works, dinners, celebrations, etc. You have always been kind to me and made the work place a pleasant and easy-going environment. I thank you guys for that!

També m'agradaria donar les gràcies a tots aquells que han format part d'una forma o altra de la meva educació. Això inclou a tot el professorat del CEIP Mare Nostrum, de l'IES Josep Pla i de la facultat de física de la Universitat Autònoma de Barcelona. Tampoc voldria deixar de mencionar la meva educació musical a l'acadèmia Escayola i al Conservatori del Liceu de Barcelona. En especial, el meu sincer agraïment al Sergi Gallardo, per ser més que un professor, i al Xavi Álvarez, per transmetre'm la seva passió per la investigació i esdevenir la primera pedra d'aquest trajecte. Special thanks as well to the professors from my Masters at the University of Luxembourg, whom I think of very highly. To Susanne, for her devotion and giving me the possibility to work as her student assistant; to Phil, for all the interesting and fruitful discussions; and to Andreas, for his guidance and support when I first arrived to Luxembourg.

A mis amigos "luxemburgueses" Andres, Kobi y Acerina. Que bonito fue conoceros en Unival II ese otoño de 2016 y compartir con vosotros todos estos años y momentos. Como los primeros encuentros en Belval, la noche de las vías del tren, las cenas con "Jarabe de Palo" y todos esos cánticos a 4 voces... "repetimos"? Gracias de todo corazón a los tres por haberme dado alas siempre que lo he necesitado.

Als meus anys amics de carrera, al Pau, a l'Arnau, a l'Adrià, al David, al Bernat i a l'Emili. Gràcies a tots pels moments viscuts i per ser tan macos i ben parits. Gràcies per fer-me de far: xerrar amb vosaltres sempre ha estat sempre un estímul addicional.

Als meus amics de tota la vida, per ser qui són i per ser els més grans. Al Bruno, a qui dec hores i hores d'escolta i ajuda; a l'Albert, per les voltes al barri "intentant posar llum a la foscor"; al Javi, per veure el got sempre mig ple; al Miguel, per veure'l sempre ple del tot; a l'Óscar, per ser el més divertit de la colla, al Pol, que disfruta de la vida com ningú, i al Gerard, per ser el meu "germà" gran. Gràcies de per ser-hi sempre companys. No cal dir quant d'orgullós em sento de tenir-vos.

Al tiet Ferran, a la tieta Isabel, a l'Albert i a la Maria, pel seu suport en els moments complicats. Les paelles a Collsuspina i els Sant Esteves plegats no havien tastat mai tan bé com en els últims cinc anys:)

Danke an meine deutsch-amerikanische "Familie", die mir geholfen hat, mich in einem fremden Land heimich zu fühlen, und mit denen ich so viele besondere Momente und Erlebnisse teilen konnte. Especially to Josef and Lynn, for "hosting" me I-do-not-know how many weekends, and all the fun we had. Thank you guys for all your help and assistance, it has been massive.

A tots els de casa, a la Maria del Mar i al Guille, a la Iaia, a la Marta, al Pol, a la tieta Roser i al tiet Pep, per fer-me sentir sempre el vostre escalf i a prop vostre. Que especial i reconfortant han estat totes les tornades, Nadals, caps de setmana... Recordo amb molta emoció el sopar de comiat que vam fer abans que marxés per primer cop a Luxembourg, i la presència de tots vosaltres a l'aeroport l'endemà. Gràcies de tot cor per ser-hi sempre i cuidar-me tant.

To Natalie, my love and life companion, my dearest, my true sunshine. Thanks for every bit we have shared together, for all the adventures, for all that is to come. I felt (and feel) your support and help every single day. A big part of this work is yours.

Als meus pares, al Carles i la Montse, per donar-m'ho tot i per fer-me sempre feliç. Gràcies per tota l'estima, esforç i educació. Gràcies per tant. Aquesta tesi no hagués estat possible sense vosaltres.

Table of Contents

List of Figures

List of Tables

Nomenclature

Characters

Symbol	Description	Unit
C_v	specific heat capacity at constant volume	$\mathrm{m}^2 \cdot \mathrm{s}^{-2} \cdot \mathrm{K}^{-1}$
C_p	specific heat capacity at constant pressure	$\mathrm{m}^2 \cdot \mathrm{s}^{-2} \cdot \mathrm{K}^{-1}$
k	thermal conductivity	$\mathrm{kg} \cdot \mathrm{m} \cdot \mathrm{s}^{-3} \cdot \mathrm{K}^{-1}$
T	temperature	K
t	time	s
p	thermodynamic pressure	$\mathrm{kg} \cdot \mathrm{m}^{-1} \cdot \mathrm{s}^{-2}$
$\hat{p}$	hydrostatic pressure	$\mathrm{kg} \cdot \mathrm{m}^{-1} \cdot \mathrm{s}^{-2}$
$\boldsymbol{V}$	velocity vector	$\mathrm{m} \cdot \mathrm{s}^{-1}$
u	x component of velocity	$\mathrm{m} \cdot \mathrm{s}^{-1}$
v	y component of velocity	$\mathrm{m} \cdot \mathrm{s}^{-1}$
w	z component of velocity	$\mathrm{m} \cdot \mathrm{s}^{-1}$
C_R	coefficient of restitution	1
Re	Reynolds number	1
Pr	Prandtl number	1
Ma	Mach number	1
α	thermal diffusivity	$\mathrm{m}^2 \cdot \mathrm{s}^{-1}$
μ	dynamic viscosity	$\mathrm{kg} \cdot \mathrm{m}^{-1} \cdot \mathrm{s}^{-1}$
ν	kinematic viscosity	$\mathrm{m}^2 \cdot \mathrm{s}^{-1}$
γ	heat capacity ratio	1
ρ	density	$\mathrm{kg} \cdot \mathrm{m}^{-3}$
τ	cycle period	s
τ_w	waiting time	s
τ_t	thermalisation time	s

Operators

Symbol	**Description**
O	order of magnitude
Δ	difference
∇	gradient operator

Abbreviations

Acronym	**Description**
AER	Active Electrocaloric Regenerator
BC	Barocaloric
BTO	Barium titanate
CFD	Computational fluid dynamics
EC	Electrocaloric
eC	Elastocaloric
EH	Energy Harvesting
FEM	Finite Element Methods
MC	Magnetocaloric
MLC	Multilayer capacitor
mC	Mechanocaloric
PEEK	Polyvinylidene fluoride
PMN	Lead magnesium niobate
PST	Lead scandium tantalate
PP	Parallel plates
PVDF	Polyvinylidene fluoride
PEEK	Polyether-ether-ketone

Chapter 1

Introduction

1.1 Contextualization and motivation

Plenty of energy conversion processes are still based today on the combustion of fuel fossils such as coal, oil, and gas [13]. Examples of these kinds of energy conversions are the production of electricity by thermal power plants, the operation of most of our transportation means (cars, trucks, and planes), or the thermal management of living spaces, including the heating of water and stoves. These processes generate CO_2 emissions that accumulate at the atmospheric layers and trap the infrared radiation coming from the sun, altering the planet's natural greenhouse (GH) effect [14]. Other well-known GH gases are nitrous oxide N_20, which are massively used in fertilizers, and hydrofluorocarbons (HFCs), which constitute the refrigerants in most cooling systems [15]. Even though the number of emissions of these gases is minor in comparison to carbon dioxide, they possess greater greenhouse effects (in some cases a thousand or tens of thousands times more [15, 16]). The continuous, disproportional growth of humankind's activities has notably increased the overall concentration of GH gases in the atmosphere, yielding a temperature rise of our planet by at least 1.1 °C in comparison to the average values that were historically reported before the industrial revolution (1750) [17]. This phenomenon, commonly known as global warming (GW), constitutes one of the main causes of climate change, entailing catastrophic consequences to the species and people's livelihoods like the melting of polar ice caps (rising the sea levels), acidification of the oceans, extreme weather conditions, or an increase in the number of natural disasters, including floods, typhoons, or earthquakes, to name a few [18].

To mitigate these effects, some nations in the world have committed to limit their GH emissions by 2050 by turning some of the aforementioned combustion processes into electrical engines, while powering them with low-carbon electricity, ideally coming from green, renewable energy sources [19]. To complete the puzzle, action must be taken in currently dominant cooling systems based on the compression and expansion of powerful GH gases (HFCs) as well [20]. Especially if we bear in mind that, in our increasingly warming planet, the demand and need for cooling will notably rise in the coming years. But so will the amount of HFCs emissions, entering into a detrimental, vicious loop: the higher the cooling activity, the warmer the planet becomes, and so on and so forth [20]. To stop this, the Kigali Amendment to the Montreal Protocol has urged the replacement of harmful HFCs by natural refrigerants with a lower or ideally zero global warming potential (GWP) in more energy-efficient systems [21]. By doing so, it is believed that an increase of 0.4 °C of GW could be avoided by 2100. This is equivalent to saving up to 210-460 gigatonnes of carbon dioxide over the next four decades, or up to four to eight years of total annual global greenhouse gas emissions (if we consider levels from 2018) [20]. However, the use of some of these natural refrigerants (like CO_2 or ammonia) still entails other side effects, such as flammability, the handling of high pressure, or toxicity. In addition, the currently dominating vapor compression systems are prone to reduce their efficiency by more than half (from $\sim$ 60% to 20–30%) when their size is reduced. It is clear, thus, that a new generation of more efficient cooling systems free of GH emissions is in huge demand.

In recent years, materials displaying reversible entropy changes subjected to modifications on magnetic, electric, and mechanical fields have been identified as excellent candidates to replace current cooling systems [5, 12, 22–27]. These materials are typically labelled as magnetocalorics (MC), electrocalorics (EC) and mechano-calorics (mC), depending on the kind of interaction that they are sensitive to [28–32]. The last splits into elastocalorics (eC), if the compressive and tensile stresses are uniaxially applied, or barocalorics (bC), if hydrostatic pressure is applied instead. These so-called "caloric" effects are interesting because 1) they do not deploy any kind of greenhouse gases, and 2) the amount of work that is required to trigger them is low compared to the amount of heat that is exchanged, which makes them energy-efficient [33]. Among the four different caloric families, magnetocalorics is by far the most mature of them, and more than 40 prototypes have been proposed over the last 50 years now [10, 34]. The first MC heat pump was designed by Brown in 1975 [35], who applied the concept of heat regeneration to notably enlarge the cooler's temperature span (temperature difference between the hot and cold side of a cooling device). He measured initially 47 K of temperature span when driving MC effects of 14 K in Gd plates at the applied magnetic field of 7 T. Shortly after, he obtained 80 K in a similar study [30]. Since then, MC heat pumps based on active regeneration have shown no difficulties to repeatedly display $\Delta T_{span} > 20$ K and cooling powers of > 1000 W kg^{-1} of active MC material [34]. Examples of that are given by Bahl et al. [36], with a temperature span of 25.4 K or a cooling power of 1010 W in a 2.8 kg gadolinium (Gd) based prototype, and Jacobs et al. [37], whose prototype based on 1.52 kg of La(Fe,Si)$_{13}$H was able to show a maximum cooling power of 3042 W. Despite these convincing performances, the high costs of benchmark MC material Gd and the required permanent magnets have challenged and limited the commercial development of MC coolers. Elastocalorics, on the contrary, are found in an earlier stage of research and development. They exploit martensitic phase transitions in shape memory alloys of nickel- and copper-based compounds, displaying adiabatic temperature changes $|\Delta T| \approx 20 - 40$ K [38–40] and $|\Delta T| = 12 - 15$ K [41, 42], respectively, under applied strains < 10% [43]. Like MC, eC demonstrators have been able to show competitive cooling. Examples of this are the active regenerator proposed by Tusek et al. [22] in 2016, reporting a heating power density of 800 W kg^{-1} at a temperature span of 15.1 K, or the recent work of Snodgrass and Erikson [44], exhibiting a no-load temperature span of 28 K. Nevertheless, these performances are limited by the short-fatigue life and hysteresis of eC compounds, and the large sizes of the associated drivers and system design, challenging their industrialization [43]. Though barocalorics constitute the most embryonic of the caloric families, they have already shown enormous potential by displaying entropy changes comparable to those of standard commercial fluid refrigerant R134a ($|\Delta S| = 520$ J kg^{-1} [45]). These are $|\Delta S| = 445$ J kg^{-1} K^{-1} in plastic crystal neopentylglycol (NPG) $(CH_3)_2C(CH_2OH)_2$ at a pressure $|p| = 0.25$ GPa [23] and $|\Delta S| = 120$ J kg^{-1} K^{-1} in trinuclear spin-crossover complex Fe_3 $(bntrz)_6$ $(tcnset)_6$ [46] at $|p| = 0.26$ GPa. The associated adiabatic temperature change of these materials was $|\Delta T| \sim 35$ K in both cases.

Similarly, electrocalorics exploit paraelectric (PE) to ferroelectric (FE) phase transitions in ferroelectrics, where polarization is more susceptible to be varied and pyroelectric coefficients are large. EC effects have been identified in the antiferroelectric (AFE) – FE phase transition as well, displaying converse EC effects (meaning that the application of an electric field generated negative temperature changes instead [47–49]). EC materials are particularly interesting among the other caloric families because 1) they can make direct use of electricity, 2) the costs of applying electric fields are low and 3) they can be scaled in small devices. In addition, they are prone to increase the overall device efficiency, as has been already experimentally demonstrated by recovering up to 70 % of the electrical charge [26, 50].

Even though the first observation of EC effects dates back to 1930 in the Rochelle salt [51], it was not until 20 years later (1950) that a quantitative measurement was provided in potassium dihydrogen phosphate (KDP) [52]. During the 1950s decade, the effect had only been observed at very low temperatures and hence it was considered only as a cryogenic cooling technology. An example of this is KCl, that showed a $|\Delta T| = 0.5$ K at 2 K and applied field 41 kV cm^{-1} [53]. In the 1960s, ceramic perovskites such as $BaTiO_3$ [54] or $Pb(Zr,Ti)O_3$ [55] provided similar EC effects though at room temperature and above, envisioning the developing of coolers in more familiar places like habitable spaces or to cool food. For many years, the highest EC effect was seen in $Pb_{0.99}Nb_{002}(Zr_{0.75}Sn_{0.20}Ti_{0.05})_{0.98}0_3$, exhibiting $|\Delta T| = 2.6$ K near 430 K and under the application of $20 - 30$ kV cm^{-1} [56]. The discovery of giant EC effects $|\Delta T| \sim 12$ K in $Pb(Zr_{0.95},Ti_{0.05})O_3$ thin-films [57] in 2006, and in ferroelectric polymer ferroelectric poly(vinylidene fluoride triuoroethylene) thin-films two years later (2008) [58], stirred up the topic, leading to an increase of the research conducted at both material and device level. Recently, direct observations of $|\Delta T| = 5.5$ K and $|\Delta T| = 7.5$ K have been reported at room temperature in $Pb(Sc,Ta)0_3$ multilayer capacitors [12] and PVDF films [59] at the applied fields of 290 kV cm^{-1} (close to breakdown) and 500 kV cm^{-1} (about 20% of the breakdown), respectively.

Unlike MC and eC, EC demonstrators have encountered difficulties to display temperature variations larger than 10 K. The first EC prototype was proposed in 1989 by Sinyavsky [6, 60]. It consisted of two blocks made of bulk $Pb(Sc_{0.5}Ta_{0.5})O_3$ (PST) parallel plates in which a dielectric heat transfer fluid was displaced through. Under an applied field of 15-25 kV cm^{-1}, the material showed $|\Delta T| = 1.4 - 1.8$ K and a temperature span of 5 K was measured in the device. Later on, in 1995, the authors proposed an upgraded version of their prototype consisting of 400 g of bulk PST [61]. This device provided a temperature span of 8 K. When pushing the field close to the breakdown, the authors claimed 12.7 K, though this could not be sustained because the samples underwent failure shortly after. It was not until two decades later (2012) that the second EC prototype was attempted [62]. This device exploited serendipity observation of EC effects in commercial doped $BaTiO_3$-MLCs [63] to build a device that, contrary to previous caloric prototypes, was not based on the circulation of a heat transfer fluid. Instead, a motorized stage was used to displace cyclically a single BTO-MLC between a heat sink and a heat source. The intrinsic $|\Delta T|$ of the material was 0.4 K under 300 kV cm^{-1} of applied electric field and the maximum temperature difference between sink and source was observed to be 1 K. In 2013, another solid-state based EC actuator was presented based on the oscillatory movement of bespoke PVDF-MLCs through stainless-steel plates, mimicking passive heat regeneration principles [64]. At the applied field of 1000 kV cm^{-1}, the material exhibited $|\Delta T| = 2.25$ K, which was translated into 6.6 K of temperature difference in the device. In 2015, a fourth EC cooling device was proposed by Plaznik et al. [7] revisiting the work of Sinyavsky. The EC material consisted of $[Pb(Mg_{1/3}Nb_{2/3})O_3]_{0.9}$ $[PbTiO_3]_{0.1}$ (PMN-10PT) relaxor ceramic, displaying a $|\Delta T| = 0.9$ K at 50 kV cm^{-1}. The maximum temperature span measured in the device under these conditions was 3.3 K. An upgraded version of this work was published a few years later including cooling power measurements and numerical models. The maximum cooling power measured was 16 W kg^{-1} of active EC material [65]. Back in 2015, the first EC prototype based on the action of heat switches was proposed [66]. The EC material consisted of commercial BTO-MLCs, exhibiting adiabatic temperature changes $|\Delta T| = 0.5$ K under the application of 277 kV cm^{-1} fields. Such a system was able to display a maximum heat flux of 36 mW and a temperature difference around 0.3 K. Commercial doped BTO-MLCs of the same kind were used as well in 2016 in another fluid-based prototype [67] utilizing 150 of these samples. The device followed passive regeneration and used a pneumatic piston to displace the BTO-MLCs through a silicone oil fluid column, reaching a maximum temperature span of 0.15 K. In 2017, Ma et al. presented a novel design in which electrostatic interaction was used to displace a PVDF-MLC between a heat sink and a heat source [9]. The authors reported an unprecedented cooling power density of 2800 W kg^{-1} that yielded a coefficient of performance (COP) of 13. The maximum temperature difference between the heat sink and source was 2.8 K at the applied field of 667 kV cm^{1}.

The main reason behind these low temperature spans is the rather low temperature variations that EC materials display (< 5 K). However, MC heat pumps, which suffer from the same issue, have successfully solved that by exploiting aforementioned heat regenerative cycles [10, 34, 68]. Even though these cycles have been deployed in EC coolers too, EC materials are poor thermal conductors (ceramics and polymers, $\lambda = 0.1 - 1$ W m^{-1}), challenging heat regeneration. Moreover, these coolers compel the use of dielectric fluids with very poor thermal properties.

During the course of this dissertation, the idea occurred to us of investigating the pyroelectric properties of bespoke PST-MLCs and revisit Olsen's work on heat energy harvesting. This was motivated by 1) the excellent electrocaloric characteristics these samples showed, as well as 2) the promising results that were obtained with our EC prototypes. Due to the valuable findings, a chapter dedicated to it has been added at the end.

1.2 Research questions

The following list defines the research questions of this doctoral dissertation:

(in the field of electrocalorics)

- Can EC coolers display temperature variations larger than 10 K? If so, how?

(in the field pyroelectric pyroelectric heat energy harvesting)

- Can pyroelectric harvesters produce electrical energy in the Joule range?

1.3 Thesis objectives

The following list defines the goals and objectives of this doctoral dissertation:

(in the field of electrocalorics)

- **A 10 K-temperature span EC cooler**. To design, develop and characterize a heat pump based on bespoke PST-MLCs able to reach at least 10 K of temperature span.
- **Numerical modelling of the experimental design**. To develop a numerical modelling with finite element methods to identify the weaknesses of the experimental design and provide modifications with superior performances.
- **Investigation of heat transfer coefficient of caloric coolers**. To define the heat transfer coefficient of EC regenerators and analyse its influence on the performance of such coolers.

(in the field of pyroelectric heat energy harvesting)

- **A 1 J energy harvester**. To design, develop and characterize an energy harvester based on PST-MLCs able to produce 1 J of electrical energy.
- **Numerical modelling of the experimental design**. To develop a numerical modelling with finite element methods to study the heat transfer of the experimental design and provide modifications with lower thermalization times for superior power values.

1.4 Structure and content

The following work is structured into seven chapters. While Chapter 1 serves as an introduction to the thesis, Chapter 2 provides the basics on EC and EC materials, the thermodynamics of EC based cooling prototypes, and the numerical modelling of EC coolers. Chapter 3 reviews the state of the art of EC coolers by summarizing the design and performances of all the devices developed to date. The majority of these works are prior to the beginning of this dissertation, except Pei's [26] and Schwarz's [25] prototypes. Chapter 4 shows the design, development and characterization of our active electrocaloric regenerators and presents numerical models that predict future performances. Chapter 5 investigates the relationship between the heat transfer coefficient of caloric regenerators and their regeneration factor by merging theoretical expressions from the literature and analysing more than 50 experimental caloric prototypes. That includes electrocalorics, but also elastocalorics and magnetocalorics. Chapter 6 is complementary to this dissertation and explores the potential of excellent EC materials when the actuation is reversed: instead of generating a stable temperature gradient from changes in the polarization, electrical energy is produced from oscillatory temperature variations in time. Chapter 7 provides conclusions and perspectives, summarizing the main results and outcome, and serving guidance and prospects for future works to follow.

The content of this dissertation is mainly adapted from my three first author publications "Giant temperature span in electrocaloric regenerator" [5], "Heat exchange law in caloric regenerator" [69] and "Electrocaloric coolers, a review" [70], as well as my shared first authorship "A 10 Joule-pyroelectric harvester", which is currently under review, and my first-author contribution to the book chapter "Basics of design and modelling of regenerative electrocaloric coolers" [71], which is expected to be published soon. The dissertation follows a "cumulative" style with one single unified format. All chapters start with a short introduction explaining their structure and content. The nature of each section is also detailed, specifying whether text has been explicitly taken from any of my publications, and in which way I may have edited it. My contributions to the work are also enumerated, indicating what parts were not utterly performed by me, if any.

Chapter 2

Basics of EC coolers: materials, cycles and modelling

This chapter overviews the basics of EC coolers. Section 2.1 explains the physics of the electrocaloric effect. Section 2.2 introduces the main EC materials and EC objects. Section 2.3 details the schematics and figures of merits of a cooling device. Section 2.4 focuses on the thermodynamics of these coolers and the principles that are used to amplify their temperature span. Section 2.5 reviews the modelling of active electrocaloric regenerators and Section 2.6 details the insights of a particular one utilizing finite elements software.

The text in Section 2.2 is the same as that of my first author publication "EC coolers, a review" [70]. The text in Sections 2.4, 2.5 and 2.6 is the same as that of my first author contribution to the book chapter "Basics of design and modelling of regenerative electrocaloric coolers" [71]. The text in Sections 2.1 and 2.3 has been created and added for completeness.

2.1 The electrocaloric effect

The electrocaloric effect refers to reversible thermal changes in a material driven by modifications of the applied electric field. This is displayed in Figure 2.1, which plots the temperature of an EC material (in red) and the corresponding field applied (inset in blue) as a function of time. In the step AB, the electric field is changed from 0 to 65 kV cm^{-1} and the temperature of the sample increases 2.4 °C. Similarly, in the step CD the field is removed and the material is cooled down by 2.4 °C. In the intermediate steps BC and DA, the field remains constant and the material comes back to its initial temperature by exchanging heat with the surroundings. The reason behind this temperature-electric field relationship lies on the entropy changes induced by the application (or removal) of an electric field. From a thermodynamic point of view, the total entropy differential is given by:

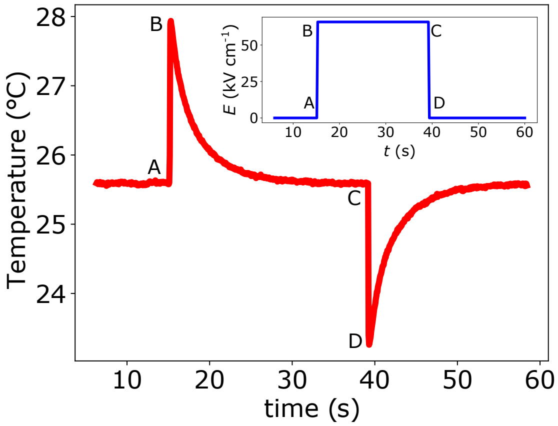

Figure 2.1 **EC effect of a PST-MLC |** In red, the temperature of a PST-MLC sample, measured with an IR camera. In the inset, the electric field applied to the sample (in blue) by means of a sourcemeter. The letters ABCD correspond to the steps of a Brayton cycle: two adiabatic legs (polarization AB and depolarization CD) and to isofield legs (temperature relaxation in BC and DA).

$$dS\,(T,E) = \left(\frac{\partial S}{\partial T}\right)_E dT + \left(\frac{\partial S}{\partial E}\right)_T dE \tag{2.1}$$

If the field is applied under isothermal conditions ($dT = 0$), and if we make use of the thermodynamic Maxwell relation $\left(\frac{\partial S}{\partial E}\right)_T = \left(\frac{\partial P}{\partial T}\right)_E$, the total entropy variation can be expressed as:

$$S(T,E_f) - S(T,E=0) = \Delta S = \int_0^{E_f} \left(\frac{\partial P}{\partial T}\right)_E dE \tag{2.2}$$

where P is the polarization of the sample and the term $\left(\frac{\partial P}{\partial T}\right)_E$ is the pyroelectric coefficient. If, instead, the field is applied adiabatically ($dS = 0$), and we consider $\left(\frac{\partial S}{\partial T}\right)_E = \frac{c_E}{T}$, with c_E the specific heat at constant applied electric field, the resulting temperature variation is

$$\Delta T = -\int_0^{E_f} \frac{T}{c_E}\left(\frac{\partial P}{\partial T}\right)_E dE \tag{2.3}$$

Equation (2.3) provides a physical description of the electrocaloric effect and describes analytically its temperature-electric field change dependence. It also suggests that electrocaloric materials must display pyroelectric effects, i.e., changes in the polarization of the material when the temperature is varied, and that the resulting temperature change is proportional to the pyroelectric coefficient. Ferroelectrics, a subgroup of pyroelectrics which display spontaneous polarization that can be switched with the application of an electric field, are interesting EC materials because they display phase transitions (from their ferroelectric to paraelectric phase) in which the pyroelectric coefficient is large.

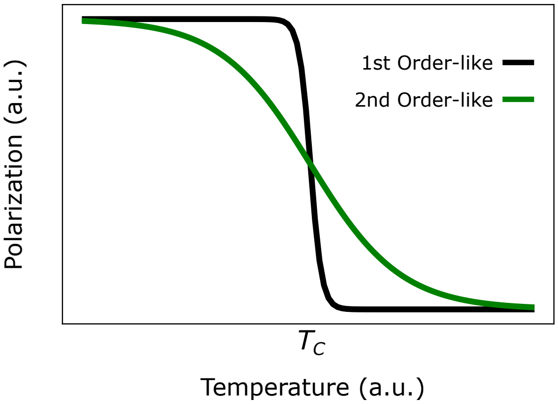

Figure 2.2 **Polarization vs temperature in a ferroelectric** | In black, a first-order-like behaviour, in green, a second-order-like one.

The character of these phase transitions (Figure 2.2) has interesting connotations in the EC performance, as can be deduced from eq. (2.3): first-order transitions favour larger EC effects, though in a narrower temperature range, and second-order transitions display smaller EC effects, but in a wider temperature range (Table 2.1).

Table 2.1 **Comparison of the EC performance between first and second-order phase transitions**

Phase transition	ΔT_{EC}	ECE temperature range
First-order	larger, $\left(\frac{\partial P}{\partial T}\right)_E >> 1$	$\left(\frac{\partial P}{\partial T}\right)_E \neq 0$ in narrower T_{span}
Second-order	smaller, $\left(\frac{\partial P}{\partial T}\right)_E > 1$	$\left(\frac{\partial P}{\partial T}\right)_E \neq 0$ in wider T_{span}

Equations 2.2 and 2.3 are typically used to report electrocaloric effects from *PE*-loops at different temperatures. These are commonly known as indirect methods, because they do not require direct measurements of heat or temperature. Direct observation of heat and temperature are possible with calorimetry, via Differential Scanning Calorimetry (DSC), or either contact or non-contact thermometry, such as thermocouples or infra-red (IR) imaging. Note that in order to display temperature variations with EC effects, adiabatic conditions must be ensured. These conditions can be experimentally triggered if the electric field is applied in a shorter time scale than the thermal relaxation time constant of the system, as shown in Figure 2.1.

2.2 Electrocaloric objects and materials

To trigger EC effects, a voltage difference is needed to be applied between two adjacent electrode plates that contain the EC material. Generally, there are three different structures in which these electrode plates can be arranged (Figure 2.3): bulk, thin-films, and multilayer capacitors (MLCs). Hereunder, more details on these structures is provided, underlining their pros and cons, and debating their suitability for the development of EC coolers.

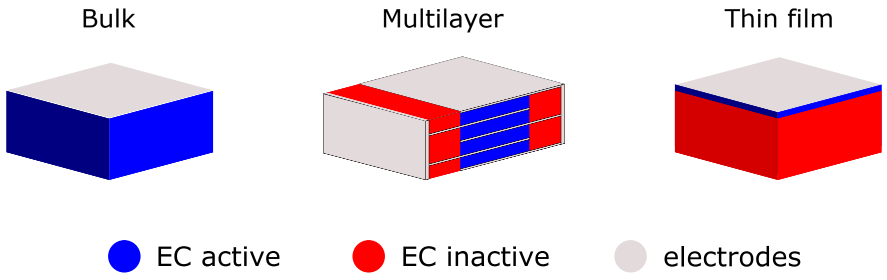

Figure 2.3 **Graphical representation of the three most common EC objects |** On the left, bulk, in the middle a multilayer capacitor structure (MLC) and on the right a thin film with its substrate. The red and blue areas correspond respectively to inactive and active EC regions. Whereas in the MLC these inactive regions correspond to the EC material itself, in thin films they represent the substrate where the films are grown onto.

2.2.1 Bulk configuration

"Bulk" structures consist of macroscopic flat samples with electrodes plates deposited at bottom and top surfaces (left object in Figure 2.3). The electrode deposition is usually done with techniques such as spin coating or sputtering, although simpler proceedings, such as handmade painting with conductive paste, epoxy, or similar conductive coatings, are possible as well. The main advantage of the bulk configuration is that the electrodes can easily cover almost the entire sample surface. Hence, the electric field is applied everywhere, and the sample is said to be nearly 100% electrocaloric active. The relatively large sample size generates a substantial amount of heat that can be directly measured either by Differential Scanning Calorimetry (DSC), when the ECE is triggered isothermally, or by thermometry, when triggered adiabatically (thermocouples, thermistor, Infrared imaging. . .) [72–74]. Similarly, the object is handy and easy to be integrated into practical devices. The main disadvantage of EC bulk structures though is that the distance between the electrodes is large ($> 100\ \mu$m). This implies the application of high voltages (> 1 kV), which challenges the experimental set-up and safety. Typical bulk materials reporting large EC effects are ferroelectric perovskite ceramics, such as $PbSc_{0.5}Ta_{0.5}O_3$ (PST), (1-x)$Pb(Mg_{1/2}Nb_{2/3})O_3$ – x$PbTiO_3$ (PMN-100xPT), $PbZr_{0.95}Ti_{0.05}O_3$ (PZT) or $BaTiO_3$ (BTO) [75–80]. These kind of samples have been already implemented in a few EC coolers [7, 60, 61, 65].

2.2.2 Thin-films

A solution to decrease the applied voltage is shortening the distance between electrode plates by growing thin films (right object in Figure 2.3). Thin films are layers of the EC material ($< 10\ \mu$m) grown on a substrate which typically is a few orders of magnitudes thicker. While one of the electrodes (< 100 nm) is deposited at the very top of the EC film, the other one can either be the substrate itself (if it is conductive) or a conductive thin layer that is placed between the substrate and the EC film. Because of the very low thickness of the films, much high electric fields can be easily induced at relatively low applied voltages (< 10 V) and larger EC effects are thus triggered. In fact, it was precisely works on thin films that lead to the discovery of giant EC effects (> 10 K) in 2006 and 2008 [57, 58], which served to revive the topic. Since then, similar performances have been achieved in the aforementioned ferroelectric ceramics and the organic ferroelectric polymer polyvinylidene difluoride (PVDF) [81–86]. Because of the fast thermalization and low amount of heat produced, EC effects in thin films are normally characterized by indirect methods [30]. A few direct measurements in thin films have been reported though, through high-resolution calorimetry [87] or highly-sensitive thin-film resistance thermometry with the so-called “3-omega” technique [88, 89]. On the other hand, direct characterization of ECE in thin films by thermometry is challenging because: a) film substrates impose non-adiabatic conditions and b) the temperature relaxation time is too short to be captured by the instrumentation currently available. To our knowledge, no works on the latter have been reported. In addition, the handling of thin films is challenging and far-fetched, what makes them today unfeasible for realistic devices in which the continuously cooling of a macroscopic object is required.

2.2.3 Multi-layer capacitors (MLCs)

There is a third kind of object that lies in between bulk and thin films: the multi-layer capacitor (MLC) configuration (centered object in Figure 2.3). MLCs consist of an engineered-like structure constituted of EC thick films (between a few µm up to 50 µm) piled up with electrodes in between. The electrode sheets are connected in parallel through electric terminals, which are usually placed at the sides (Figure 2.3). Although the overall resulting object is macroscopic, with dimensions that fall typically in the millimeter or even centimeter range, reasonable voltages (< 1 kV) are sufficient to trigger large ECEs, which is convenient and safer. While the resultant active volume is less than the overall sample volume (around 50 – 80% of the total volume, where negative and positive inner electrodes overlap) [12, 90], the quantity of heat generated is large enough to be directly measured and make use of it [12, 90–92]. Moreover, the metallic electrodes can conduct heat very efficiently thanks to thermal conductivity, roughly one hundred times larger than in EC ceramic layers, promoting heat exchange [90]. The latter can be improved thanks to the electric terminals as well [93]. On top of that, MLCs are extremely reliable, as they have been initially developed to act as large values capacitors and are currently used in plenty of electronic devices. In addition, they are less fragile than bulk thanks to their inner electrodes. The main drawback of this kind of structure though is that commercially available MLCs have not been developed for EC purposes yet and they exhibit rather poor EC effects (< 1 K) [63, 93]. To our knowledge, only the corporation Murata Manufacturing have fabricated bespoke EC MLCs [12, 93] and only for scientific and collaborative purposes. All in all, MLCs mainly based on the common EC materials PST, PMN, BTO and PVDF have proved to be the most convenient and practical objects for cooling applications, having been now exploited in several EC devices and achieving the best performances so far [5, 25, 26, 50, 62, 66, 67, 94].

2.3 Schematics and figures of merits of a heat pump

Heat pump technologies, such as refrigerators and air conditioners, are thermal engines that have the capability to transport heat from a colder location to a warmer one. In order to do that, work needs to be provided, as dictated by the second law of thermodynamics (Figure 2.4). Note that a heat pump can be either used as a heater, if thermal contact is made with the hot side, or as a cooler, if done with the cold side. The performance of these kinds of devices is typically characterized with three different magnitudes: 1) the temperature span, 2) the cooling power, and 3) the coefficient of performance (COP).

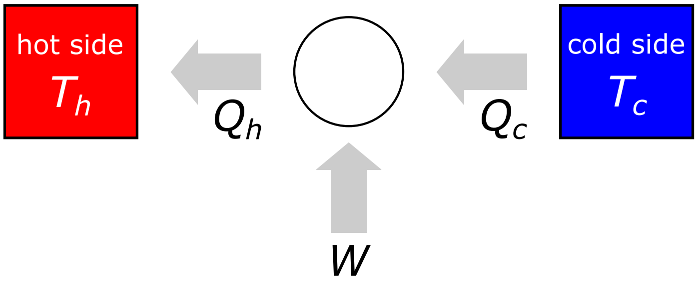

Figure 2.4 **Schematics of a heat pump** | Heat is pumped from the cold side to the hot side. To do so, work W needs to be supplied.

2.3.1 Figures of merit

Temperature span The temperature span in a heat pump refers to the difference between the average temperature of the hot side T_h (where heat is being pumped to) and the average temperature of the cold side T_c (where heat is being pumped from):

$$T_{span} = T_h - T_c \tag{2.4}$$

Cooling power The cooling power of a heat pump (that is used as a cooler) is related to its cooling capacity, i.e., how much heat can be pumped from the cold side per unit of time. It is typically expressed as:

$$\dot{Q}_C = \int \dot{m}_r c_{r,p} dT_c \tag{2.5}$$

where $\dot{m}_r$ and $c_{r,p}$ are the mass rate and specific heat of the refrigerant, respectively, and T_c the temperature of the cold side. Similarly, if the heat pump is used for heating purposes, the heating power refers to the heat flux arriving to the hot side, and is:

$$\dot{Q}_H = \int \dot{m}_r c_{r,p} dT_h \tag{2.6}$$

where T_h refers to the temperature of the sink.

Coefficient of Performance The coefficient of performance (COP) of a heat pump refers to its efficiency. It compares either the cooling or heating power with the work W needed to run the cycles:

$$COP_c = \frac{\dot{Q}_C}{W} \tau \tag{2.7}$$

$$COP_h = \frac{\dot{Q}_h}{W} \tau \tag{2.8}$$

where τ is the cycle period. Like all thermal engines, the COP has a theoretical limit given by the Carnot cycle. This is:

$$COP_{Carnot,c} = \frac{T_c}{T_h - T_c} \tag{2.9}$$

$$COP_{Carnot,h} = \frac{T_h}{T_h - T_c} \tag{2.10}$$

Because COP < COP$_{Carnot}$, it is common to report the ratio between the actual COP of a cooling device and the corresponding COP$_{Carnot}$. This can be defined as the relative COP (COP_r), which is usually referred to as exergy efficiency of second law efficiency:

$$COP_r = \frac{COP}{COP_{Carnot}} \tag{2.11}$$

2.4 Regenerative principles and thermodynamic cycles of EC prototypes

Despite the progress in the development of electrocaloric (EC) materials, electrocaloric effects (ECE) experimentally observed to date have produced adiabatic temperature variations of only a few degrees [12]. Considering that temperature spans of at least 15-20 K are required for actual cooling applications such as air conditioning [95], EC devices are still bounded to employ thermodynamic cycles able to amplify the magnitude of the EC effects, and this is typically done with regenerative cycles [96] like heat regeneration or by cascaded or multi-staged systems. Because these cycles are not specific for EC, they are reviewed here from a more generic point of view.

2.4.1 Heat regeneration

Heat regeneration has been by far the most widely studied cycle to amplify caloric effects, especially in magnetocalorics (MC), where more than 50 prototypes have been developed following this principle [34, 97]. Even though MC materials have recently proven to display colossal adiabatic temperature changes (50 K) [98] at extremely high magnetic fields, the cost of applying such fields is too high, and practical adiabatic temperature changes lie usually in the range from 1 K to 5 K. With this range, heat regenerators are a must. Regenerative heat pumps have been developed as well in elastocalorics [22, 44, 99], despite their higher adiabatic temperature changes (>10 K) [100], and so it has been the case in electrocalorics (EC) [5–8, 67], where lower EC effects are typically measured (< 5 K) [12, 75], even at very high applied electric fields.

Although heat regenerative cycles were initially proposed by Stirling in the 19th century, it was not until 1975 that Brown applied them for the first time in a practical caloric heat pump based on MC materials [35]. The cycle that Brown proposed consisted in displacing the caloric material throughout a heat transfer fluid column and 1) activating the corresponding magnetic field (the material generates heat) at the top of the column while 2) removing it (the material absorbs heat) when the material reaches the bottom of the column (Figure 2.5a). When doing so, heat was stored in the heat transfer fluid so it could be re-used to pre-heat (or pre-cool) the material before the caloric effect was triggered again. As a result, a temperature gradient was built in the fluid column that could exceed the adiabatic temperature change of the material by a factor of 6. This is known as passive regeneration, in which the entire caloric material undergoes the same thermodynamic cycle because the potential thermal gradient that can be created in the material is negligible compared to the gradient stabilized in the heat transfer fluid column. A few years later, Steyert [101] first and then Barclay and Steyert [102] presented an evolution of Brown's work that they

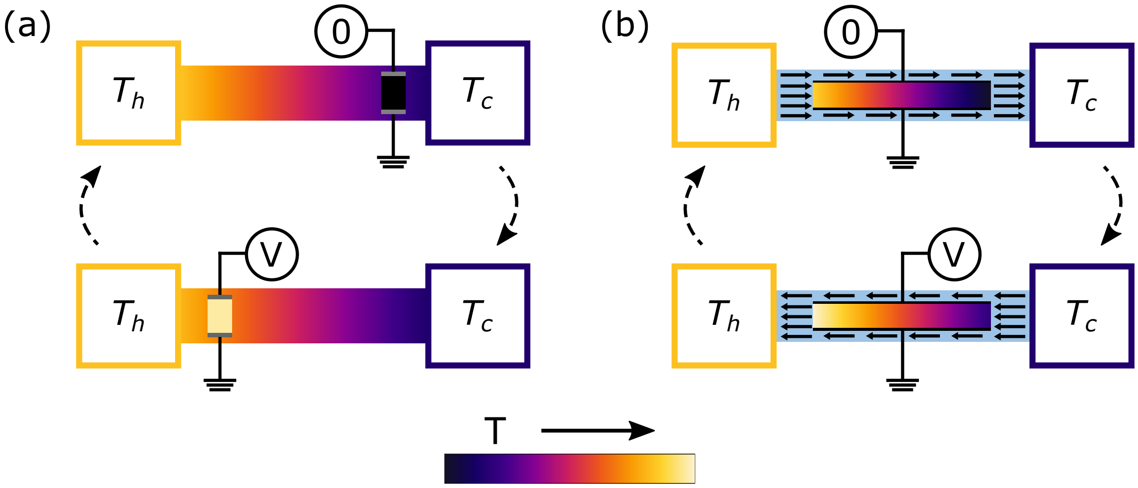

Figure 2.5 **Passive and active heat regeneration diagrams** | (a) passive heat regeneration, where an EC material is moved throughout a fluid column, and (b) active heat regeneration, where a fluid is moved through a caloric material back and forth. Modified from Bhasi Nair's PhD thesis [1].

called active regeneration. The main difference in active regeneration is that the heat transfer medium is moved through the caloric material back and forth synchronously with the activation and deactivation of the caloric effect while the caloric material remains static (Figure 2.5b). As a result, a temperature gradient is created alongside the caloric material, and each infinitesimal point is said to undergo its own thermodynamic cycle. To allow circulation of the fluid through the caloric material, the latter needs to be assembled in a porous-like geometry such as parallel plates, sphere-beds, or cylinders. Other assemblies are possible too and will depend mostly on the nature and characteristics of each caloric family. For instance, in electrocalorics, parallel plates are a common assembly because it is convenient and easy due to the electrode plate terminals. In elastocalorics (eC), cylinders and parallel plates are usually employed. More information on active and passive heat regeneration can be found elsewhere [10, 103].

2.4.2 Cascading

Another possibility for cooling devices to amplify caloric effects to reach the desired temperature spans are cascading (or multistage) devices [25, 26]. The idea of cascading systems is to pump heat through a series of stages containing the caloric material (Figure 2.6), that are found in between a heat source and a heat sink. To force heat being pumped from the source to the sink, consecutive stages are set to operate in anti-phase. This means that when the corresponding field is applied ($E > 0$) to stages s: s_1, s_3, s_5, $s_7 \ldots$, no field is applied ($E = 0$) to stages s_2, s_4, s_6, s_8..., and vice versa. In addition, a thermal contact (symbolized by the black ring in the figure) is established between two consecutive stages

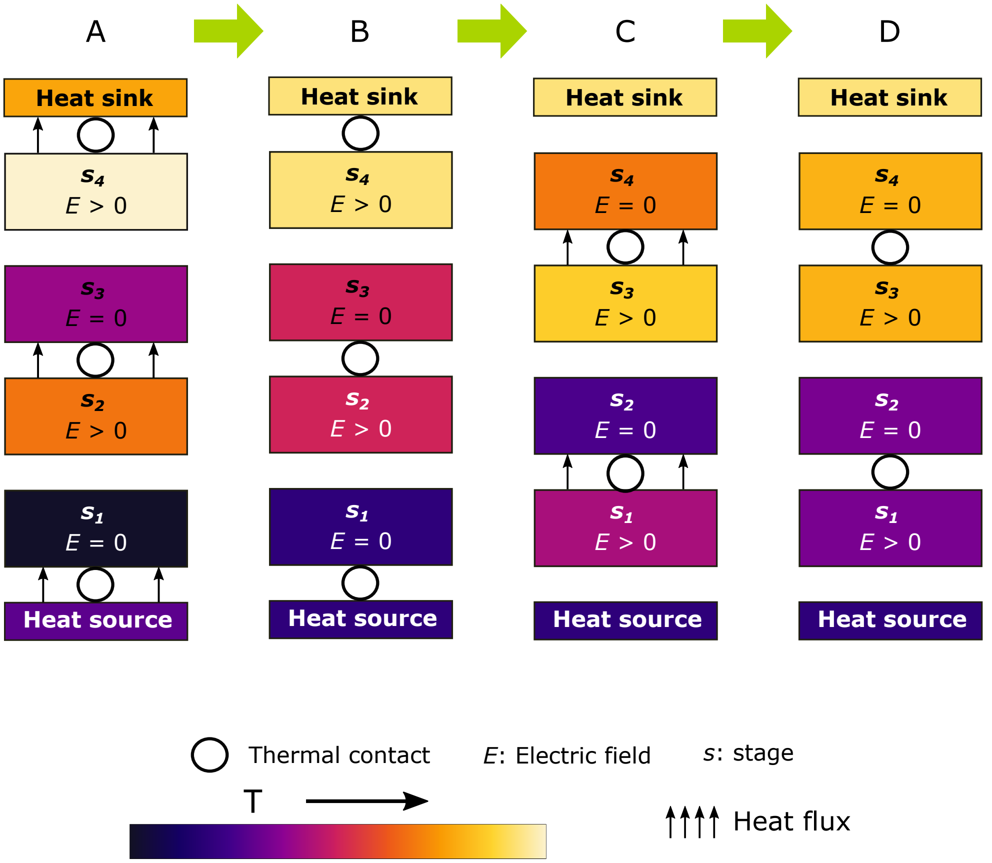

Figure 2.6 **Sketch of a four-stage (s_1-s_4) cascading system and its cycle steps (A, B, C, D)** | The black ring represents thermal contact between adjacent stages and the colour scale is to represent the temperature gradient. Note that the consecutive stages operate in anti-phase.

when the field is applied to the lower-indexed stage s_n (within this notation, s_1 is next to the source, and s_N is next to the sink). To make thermal contact between stages, a fluid can be circulated between them. This, for instance, has been the case in a recent eC prototype which achieved a record T_{span} of 28 K [44]. Another possibility is simply by physically contacting the adjacent stages, as shown by [25, 26]. Heat switches are interesting for these purposes because they can conveniently create or extinguish thermal roads [66, 104].

2.4.3 Thermodynamic cycles of fluid-based active regenerators

Here we are going to describe the thermodynamic cycles of the most common kind of caloric prototypes—active regenerators. As described above, the operation of active regenerators involves application of the corresponding conjugate field (magnetic, electric field, uniaxial stress, or hydrostatic pressure) and oscillatory displacement of a heat transfer substance through the caloric material. Normally, this heat transfer substance is a fluid, but there are as well some active regenerators based on solid-solid interactions. Although the description of active regenerators is very similar for all the caloric families, we focus here only on those utilizing EC materials and a fluid (fluid-based active electrocaloric regenerators (AER)). In EC, application and removal of an electric field induces polar entropy variations that are translated into temperature differences if adiabatic conditions are respected. The cycle steps of an AER are described in Figure 2.7, where the colour legend stands for the temperature difference with respect to the initial temperature. These steps are:

- Polarization of the EC material - an electric field is applied homogeneously to the EC material. The EC material undergoes the EC effect and warms up.
- Displacement of the heat transfer fluid from the cold side to the hot side. When the cold fluid passes through the EC material, heat transfer occurs heating up the fluid and cooling down the EC material.
- Depolarization of the EC material – the electric field is removed from the EC material. The EC material undergoes the EC effect and cools down.
- Displacement of the fluid from the hot side to the cold side. When the warm fluid passes through the EC material, heat is transferred. The fluid cools down and the EC material heats up.

Depending on how we apply the electric field, on how we displace the heat transfer fluid and how we couple these two operations, the AER cycle is going to resemble a different kind of thermodynamic cycle. For instance, if we apply the electric field fast enough (heat is generated faster than it can escape) and adiabatic conditions are fulfilled, the cycle is said to resemble the Brayton cycle[1], and, hence, is identified as a Brayton-like cycle. If, otherwise, the electric field is applied slowly enough (the generated heat escapes at the same rate) and isothermal conditions are fulfilled, the cycle is said to resemble the Ericsson cycle[2], and, similarly, called an Ericsson-like cycle. Note that Ericsson cycles must be regenerative cycles because otherwise there is no heating or cooling of the material. Even though the reversible behaviour of Ericsson cycles makes them more efficient, Brayton cycles permit achieving higher temperature spans, and the latter are more often considered in experiments.

Sometimes, limitations of experimental set-ups do not permit having the fluid idle in the polarization and depolarization steps. Instead, the fluid is constantly moved, and it changes

---

[1] In gas turbines, a Brayton cycle is formed by two adiabatic legs, in which the air of the compressor is compressed and expanded at constant entropy, and two isobaric legs, where heat is added and rejected at constant pressure.

[2] In gas turbines, an Ericsson cycle consists of two isothermal legs, in which the air is compressed and expanded at constant temperature, and two isobaric legs, in which heat is added and rejected at constant pressure.

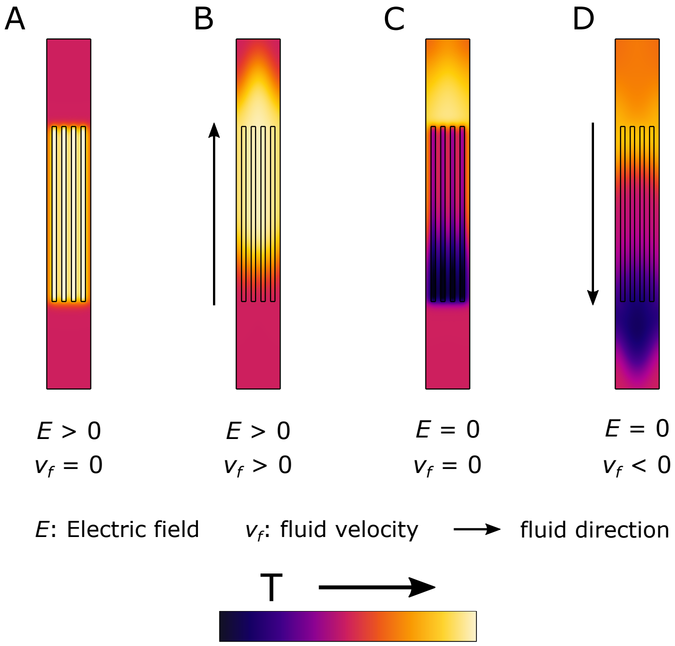

Figure 2.7 **Illustration of the AER thermodynamic cycle steps (A, B, C, D)** | In A, the EC material is polarized ($E > 0$) and heats up (due to the ECE), while the fluid remains static. In B, the fluid is displaced from the cold side to the hot side, while the electric field E remains constant. The fluid absorbs heat from the EC material and heats up, while the EC material cools down. In C, the electric field is removed with depolarization of the EC material, and it cools down (thanks to the ECE) while the fluid stays static. And in D, the fluid is displaced from the hot side to the cold side at $E = 0$. The fluid releases heat to the EC material and is cooled down, while the EC material heats up.

only its flow direction. Because the fluid movement increases heat transfer, the adiabaticity is reduced, and we refer to these cycles as Ericsson-Brayton-like cycles.

The three exemplified cycles are shown in Figure 2.8, where electric field (thin line) and fluid volume flow rate (thick line) profiles are plotted as functions of time. The plane shaded area corresponds to the heat generated or absorbed due to the EC effect whereas the striped-shaded area corresponds to the total amount of fluid displaced. Specifics of each cycle step for the three described cycles are collected in Table 2.2, which has been adapted from [10]. Note that step-like profiles do not have to be necessarily the case, and other kinds of functions with smoother shapes can be attempted when describing the electric field and fluid displacement time-dependent profiles. Note as well that in the Ericsson-Brayton-like cycle proposed in Figure 2.8, the electric field and the fluid displacement are completely synchronized. A certain phase shift can be introduced as well.

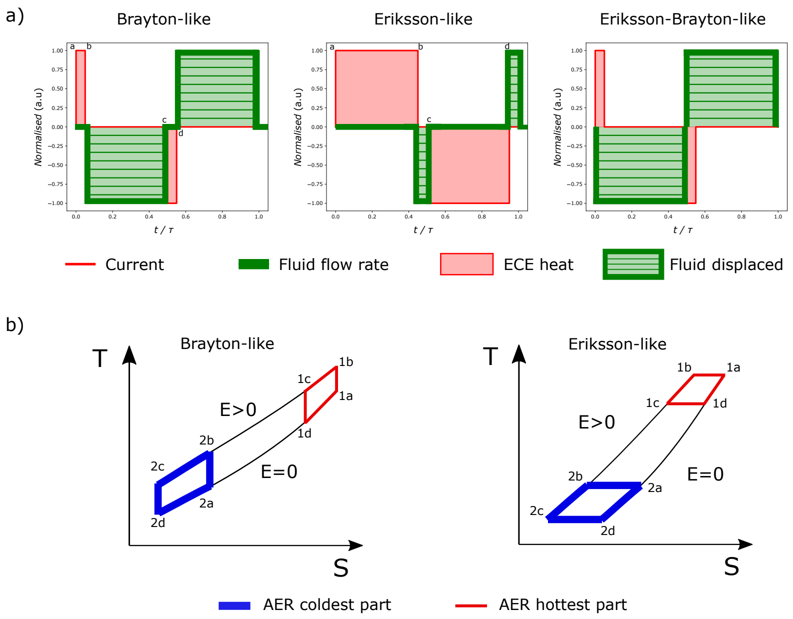

Figure 2.8 **Flow rate, current and *T-S* diagrams of different AER cycles |** a) Normalized profiles of electric current and fluid volume flow rate associated with different thermodynamic cycles: (left) Brayton-like, (middle) Ericsson-like, and (right) Ericsson-Brayton-like. The amount of heat generated by the ECE is given by the plane-shaded aera, whereas the amount of displaced fluid is represented by the striped-shaded one. b) Temperature-Entropy ($T-S$) diagrams for the Brayton-like and Ericsson-like cycles of an AER. The lower branch is at zero applied electric field ($E = 0$, whereas the upper one is at $E > 0$. The thin-line loop (1a-1b-1c-1d) corresponds to the thermodynamic cycle of the hottest part of the AER, whereas the thick-line one (2a-2b-2c-2d) corresponds to the coldest part.

Table 2.2 **Comparison of AER thermodynamic cycles |** Adapted from "Magnetocaloric energy conversion: from theory to applications" [10]. The different steps of Ericsson-like, Brayton-like, and Ericsson-Brayton-like cycles for active electrocaloric regenerators (AER) are described.

Cycle steps	Ericsson-like	Brayton-like	Ericsson-Brayton-like
1	Isothermal polarization	Adiabatic polarization	Adiabatic polarization + isofield cooling of EC material
2	Isofield cooling of EC material	Isofield cooling of EC material	Isofield cooling of EC material
3	Isothermal depolarization	Adiabatic depolarization	Adiabatic depolarization + isofield heating of EC material
4	Isofield heating of EC material	Isofield heating of EC material	Isofield heating of EC material

2.5 Numerical modelling of an AER

Fluid-based AER are the most common kind of caloric cooling devices. Although they have been mostly exploited in MC, their design has been frequently utilized in EC coolers as well. In this section, some insights are provided on the numerical modelling of AERs in a more general view. The content of this section has been inspired by Chapter 4 of the book "Magnetocaloric energy conversion" [10], where numerical modelling of active magnetic regeneration and its mathematical description are described in detail. Although the core material and applied field are different, the principles and operation of MC and EC regenerators (and elastocalorics ones) are the same in many ways.

2.5.1 Mathematical and physical description

When describing mathematically the operation of an AER, there are some assumptions that shall be discussed first. Although some of these approximations are based on passive regeneration works, some others can be considered as well in other kinds of cooling devices that do not follow an AER design. These assumptions are:

- Parasitic heat transfer losses towards surroundings may be neglected (see more details in Section 2.5.4).
- The only heat source and heat sink in the AER is the electrocaloric effect.
- The heat produced by the EC effect may be linear with respect to the time needed to apply the electric field (see Section 2.5.2).
- There is no fluid leakage nor porosity of structural and surrounding elements.
- The electrocaloric material plates are homogeneous, flat and the fluid channels even.
- The heat transfer fluid does not experience any phase change.
- The heat transfer fluid is incompressible and thus it does not undergo any kind of compression or expansion.
- There is no dead volume.
- Radiative heat transfer is negligible and, hence, neglected.
- The Reynolds number Re is lower than 2100 and the fluid follows a laminar flow (see Section 2.5.3).
- The fluid velocity at the fluid wall is naught (no-slip boundary condition).

- Only heat transfer by advection (heat traveling with the oscillatory fluid motion) is considered. Heat convection (heat transport from differences in fluid densities and gravitational effects) is neglected so that the temperature profile across the regenerator is symmetric with respect to its vertical centre.
- Heat generated by viscous effects is neglected for parallel-plates assemblies.

The physics that govern the operation of fluid-based EC devices such as AERs are heat transfer in solids, heat transfer in fluids and fluid dynamics. In solids, heat transfer occurs via heat conduction. This is described by Fourier's law and the continuity equation, such that:

$$\rho_s c_s \frac{\partial T_s}{\partial t} = \nabla(k_s \nabla T_s) + q_{ECE} + q_{HT} \tag{2.12}$$

where ρ, c, k, T are the density, specific heat, thermal conductivity and temperature, respectively, and the subindex s is for solids. The right-hand side term $\dot{q}_{EC}$ in eq. (2.12) accounts for the heat generated and absorbed by the EC effect and is developed in more detail in Section 2.5.2. In a fluid, heat transfer is described instead by:

$$\rho_f c_f \left(\frac{\partial T_f}{\partial t} + u \nabla T_f \right) = \nabla(k_f \nabla T_f) + \dot{q}_{vis} + \dot{q}_{HT} \tag{2.13}$$

where the convection term $u\nabla T_f$ has been added, with u being the fluid velocity vector, and the viscous heating terms $\dot{q}_{vis}$. The subindex f is used to denote fluids. In 2D or 3D models, the fluid velocity profile can be determined by solving the well-known Navier-Stokes equation by coupling it with the heat transfer equations. On the other hand, the term $\dot{q}_{HT}$ refers to the heat transfer (or the heat flux) between the solid and the heat transfer fluid, which can be expressed by Newton's law of cooling:

$$\dot{q}_{HT}(x,t) = h \frac{A_{HT}}{V} \left(T_s(x,t) - T_f(x,t) \right) \tag{2.14}$$

where h, A_{HT} and V are the heat transfer coefficient, the heat transfer area, and the volume of the solid or fluid, respectively. In 2-D and 3-D models, adding an additional boundary condition describing the heat transfer at the surface is typically more appropriate. When doing that, the term $\dot{q}_{HT}$ is removed from Equations 2.12 and 2.13. The boundary condition that is applied instead specifies that the thermal flux at the interface must be the same either when it comes from the fluid or when it comes from the solid. This is shown by:

$$k_s \left| \frac{\partial T_s}{\partial y} \right|_{y=h} = k_f \left| \frac{\partial T_f}{\partial y} \right|_{y=h} \tag{2.15}$$

where y represents the direction normal to the fluid-solid interface and h the position of the interface.

On the other hand, the term $\dot{q}_{vis}$ stands for the viscosity heating effects occasioned by the pressure drop of the fluid flow. Depending on our system, these effects may be neglected and hence, the term removed from equation 2.13. This is for instance the case of ordered structures, such as parallel-plate AER, which are common in EC and can be represented by 2D models. Differently, in packed-beds structures (common in MC), viscous effects play an important role, and a non-negligible amount of mechanical energy is degraded into heat. In this situation, $\dot{q}_{vis}$ must be included. If the reader would like to find more details on 1D models, or further considerations in the physical description such as the fluid maldistribution, hysteresis losses and heat transfer and fanning factor corelations, visit chapter 4 in the "Magnetocaloric energy conversion" book [10].

To characterize any cooling system, the temperature span, the cooling power, and the coefficient of performance (COP) need to be evaluated (Section 2.3). The temperature span is defined as the average temperature difference of the hot and cold side. In an AER, this is the difference between the average temperature of the fluid entering and leaving the AER in the hot side and that of the one entering and leaving the cold side of the AER. Regarding the cooling power (and heating power) of the AER, these are described by:

$$\dot{Q}_C = f\int_0^{\tau_f} \dot{m}_f c_{p,f}\big(T_{f,c,in}(t) - T_{f,c,out}(t)\big)dt \tag{2.16}$$

$$\dot{Q}_H = f\int_0^{\tau_f} \dot{m}_f c_{p,f}\big(T_{f,h,in}(t) - T_{f,h,out}(t)\big)dt \tag{2.17}$$

where f the cycle frequency, $\dot{m}_f$ is the mass flow rate of the fluid, $c_{p,f}$ the specific heat of the fluid, $T_{f,c,in}$ and $T_{f,c,out}$ the temperature of the fluid when it enters and exits the AER at the cold side while are $T_{f,h,in}$ and $T_{f,h,out}$ those at the hot side. Finally, the coefficient of performance (COP) is defined as the ratio of the cooling power (if cooling cycles are run) and total amount of work needed to operate the AER:

$$COP = \frac{\dot{Q}_C}{W_{EC} + W_{pump}}\tau \tag{2.18}$$

where W_{EC} represents the amount of work required to run the EC effect and W_{pump} the work of the pump. The latter can be expressed as:

$$W_{pump} = \frac{\dot{m}_f \Delta p \tau_f}{\rho_f \eta_{pump}} \tag{2.19}$$

where Δp is the pressure drop, η_{pump} the pump's efficiency and τ_f the period of the fluid flow.

2.5.2 Modelling the EC effect

There are different approaches to define the EC effect in a numerical model. In eq. (2.12), the contribution of the EC effect is represented by the term $\dot{q}_{EC}$, which is seen as an external heat source applied to EC material domains. Alternatively, the EC effect can be defined more abruptly by imposing a temperature change at the polarization and depolarization steps in the temperature variable as follows:

$$T_{s,fi} = T_{s,i} \pm \Delta T_{ad} \tag{2.20}$$

where $T_{s,i}$ and $T_{s,fi}$ are the solid initial and final temperatures, and ΔT_{ad} is the adiabatic temperature change due to polarization and depolarization. This second approach is limited to Brayton cycles because it assumes that the heat transfer between the EC material and the heat transfer fluid is blocked during the polarization and depolarization legs, which it is not necessarily the case. Utilizing the former description ($\dot{q}_{EC}$) is a more precise approach, especially in 2D and 3D models, where a temperature distribution is established in the EC material along the normal flow direction because of the heat exchange with the heat transfer fluid, regardless if the latter is static or in motion. In an FEM software (see Sections 2.6 and 4.3), it is more convenient to consider the $\dot{q}_{EC}$ approach by manually adding an external heat source at caloric material domains. Note that the applied heat source needs to have a time dependence that permits periodically bringing (and removing) heat to (from) the system at desired time steps. An example of such a heat source is given in Figure 2.9, where the heat source power P is represented by a step function, normalized to the maximum value, P_{max}, and represented as a function of time, which is also normalized by the cycle period τ. The shaded areas $P_{max} \times t_{charge}$ correspond to the heat generated by the EC material when the field is applied and to the heat absorbed by the material when the field is removed. These two heat contributions can be defined as follows:

$$Q_{gen} = \int_0^{t_{charge}} P(t)dt \tag{2.21}$$

$$Q_{abs} = \int_{\frac{\tau}{2}}^{\frac{\tau}{2}+t_{charge}} P(t)dt \tag{2.22}$$

The ECE can be measured experimentally either with a calorimetry [75] (Differential Scanning Microscope (DSC)), if the field is apply isothermally (one directly measures the heat flux), or with thermometry (thermocouple, Infrared camera, etc.), if the field is applied

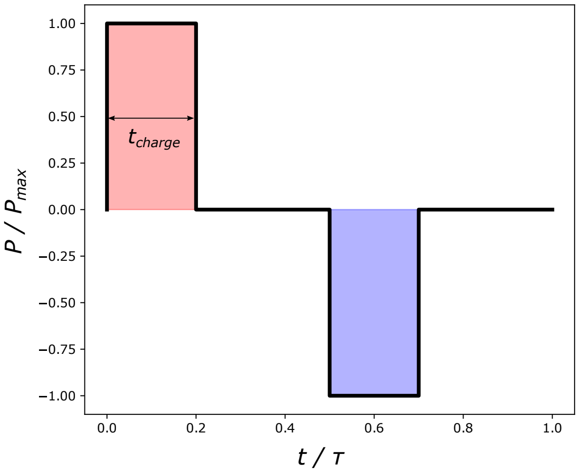

Figure 2.9 **Heat source power P as a function of time t |** The axes are normalized with respect to the maximum power and the cycle period τ. The width of the heat pulse t_{charge} relates to the time of charging of the EC material (voltage being applied from 0 to $V > 0$).

adiabatically and a temperature difference is measured instead [12, 86]. If the latter is used, the heat generated (and absorbed) can be calculated by $Q \cong mc_p \Delta T_{ad}$ [75], where m is the mass, c_p is the specific heat and ΔT_{ad} is the adiabatic temperature change. Another possibility to measure the heat is by employing indirect methods [30, 105], where PE-loops are measured instead. This yields:

$$\Delta Q = -T \int_{E_{min}}^{E_{max}} \left(\frac{\partial P}{\partial T} \right)_E dE \tag{2.23}$$

in which $\partial P / \partial T$ is the pyroelectric coefficient, T the temperature and E the electric field (more information on the different measurements of EC effects can be consulted in [27, 28, 30, 74]). The profile of the heat source power P in Figure 2.9 follows a step function and assumes that the ECE is proportional to the applied electric field. This is not how it is in reality, especially for nonlinear EC materials with a sharp first-order phase-transition such as lead scandium tantalate [75], but it serves as a fair and convenient approximation. Within this profile, the power is simply $P = Q/t_{charge}$. The more adiabatically this heat pulse is applied (for instance, by lowering t_{charge}), the more precise the approximation is. However, other power P profiles can be defined trying to reach more accurate representations. Figure 2.10 shows some examples following linear, quadratic cosine and exponential functions. In all these examples, the ECE is applied at the beginning of the cycle, $t = 0$, and removed at half of the cycle, $t = \tau/2$. This does not have to be necessarily the case, and a certain phase shift can be introduced depending on the thermodynamic cycle one wants to reproduce. A customized function emulating time evolution of the adiabatic temperature change of an EC

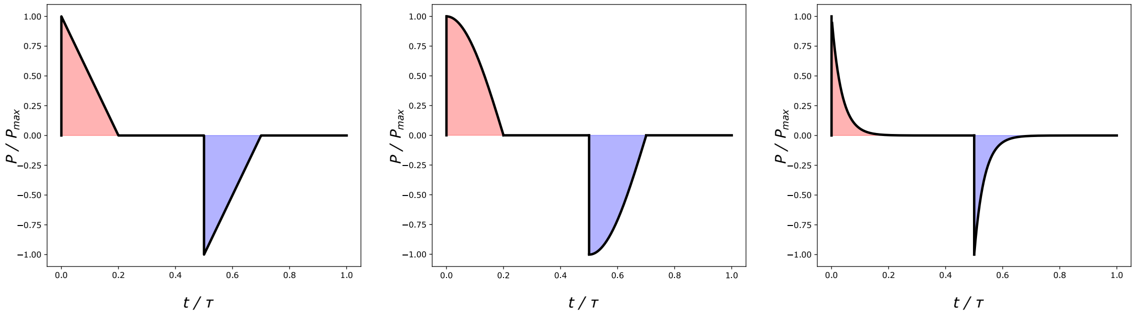

Figure 2.10 **Time profiles of the heat source power P describing the ECE |** The plot in the left follows a linear function, the plot in the centre corresponds to a quadratic cosine, and the right one follows an exponential function. Other profiles resulting from interpolation of experimental points, piecewise or analytical functions are possible.

material is possible as well, although it is more elaborated and less straightforward. In that case, the ECE of the material would need to be simulated first without the action of a fluid, and an appropriate heat pulse curve that fits the time evolution of the adiabatic temperature change would need to be found.

2.5.3 Fluid displacement considerations

The archetypal AER structure utilizes the circulation of a heat transfer fluid to pump heat from the cold to the hot side. To simulate that numerically, the so-called Navier-Stokes equation needs to be solved. The non-linearity of this differential equation makes the numerical integration of the solution more prone to divergence compared to other physical modules (for instance, heat transfer where the Fourier equation is solved). In this regard, problems with too high Reynolds numbers can compromise the integration of the solution. Another source of divergence is abrupt changes in the velocity (or fluid volume flow rate f_r) profile. This can be, for instance, the case of the oscillatory fluid motion required to operate an AER, which is experimentally best described with the step function displayed in Figure 2.11a. In this case, the fluid volume flow rate takes only two values, $+f_{r,max}$ and $-f_{r,max}$, and the discontinuities in this profile (at $t = 0$ and $t = \tau$) may be an issue for the numerical integration. To promote the convergence of the solution and facilitate its integration, smoothing the step function with mathematical treatment or using instead other functions such a sinusoidal (Figure 2.11b) or a Gaussian are good alternatives. Likewise, the shaded areas in Figs. 2.11a and 2.11b times $f_{r,max}\tau/2$ give the amount of the displaced fluid volume $V_{f,d}$. By making semi-cycle distinctions, this can be express as:

$$V_{f,d+} = \int_0^{\tau/2} f_r(t)dt \tag{2.24}$$

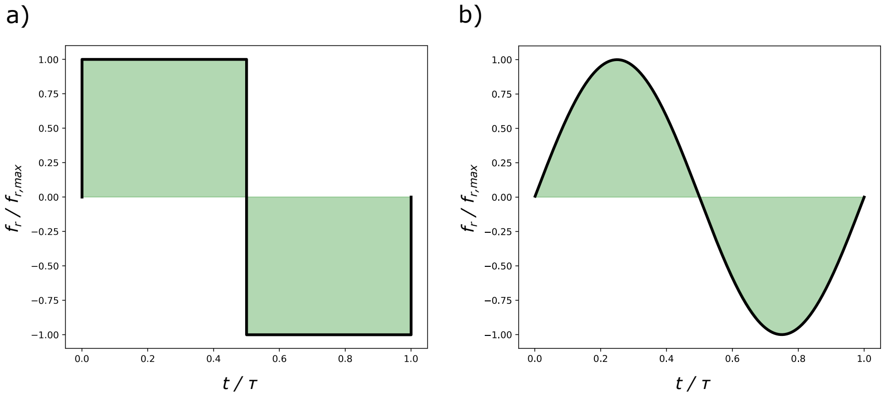

Figure 2.11 **Fluid volume flow rate f_r profile as a function of time t** | Both variables are normalized with respect to the maximum fluid volume flow rate $f_{r,max}$ and to the cycle period τ. The shaded area times $f_{r,max}\tau/2$ represents the amount of fluid displaced. The profile in a) follows a step function, a typical behaviour of pumps in a real experiment. The profile in b) follows a sinusoidal. Its smoother shape facilitates integration and allows the software to converge on a numerical solution.

$$V_{f,d-} = \int_{\tau/2}^{\tau} f_r(t)dt \tag{2.25}$$

where the subscripts + and – represent the direction of the fluid flow. No matter what is the chosen function, the latter will need to be adjusted in the model so that $V_{f,d+/-}$ matches the experimental value. Also, note that for the sake of symmetry, the net fluid volume to be displaced in the entire cycle must be 0, yielding:

$$\oint_{0}^{\tau} f_r(t)dt = 0 \tag{2.26}$$

and the amount of fluid displaced in the first half of the cycle must be opposite to that in the second half, which reads:

$$V_{f,d+} = -V_{f,d-} \tag{2.27}$$

Like for the EC effect, other functions describing the fluid volume flow rate can be used. Sometimes, the experimental profile itself does not follow a step-function, but rather a ramp, etc. The aim of numerical models is to reproduce the experimental phenomena as precisely as possible compromising the computational efficiency the least.

2.5.4 Heat losses considerations

Most models based on active regenerators assume no heat losses to the surroundings [97] by imposing adiabatic conditions at the exterior walls, i.e., no heat flux is allowed to cross

Table 2.3 **Typical values of convective heat transfer coefficients, h, under various conditions |** From Chapter 14 in [11].

Flow type	h (W m^{-2} K^{-1})
Air, free convection	2.5 – 25
Air, forced convection	10 – 500
Liquids, forced convection	10 – 15000
Boiling water	2500 – 25000
Condensing water vapor	500 – 100000

them. This is described by:

$$qn = 0 \tag{2.28}$$

where q and n are, respectively, the heat flux and normal vectors. As the first approximation, adiabatic conditions are acceptable because neglecting heat losses promotes creation of a temperature gradient in the device. However, if our purpose is to build predictive models, accounting for the heat losses to the surrounding becomes more relevant. Note that heat losses are more pronounced when housing and surrounding elements have higher thermal conductivities than the used heat transfer fluid and EC materials or at low cycle frequencies (that is, typically below ~ 0.1 Hz in EC devices). To include heat losses to the surroundings, we must add a heat flux at the exterior walls of our model. This heat transfer flux is proportional to the temperature difference of the wall and the surroundings and can be described with the following equation:

$$q = h(T_{ext} - T) \tag{2.29}$$

where q is the heat transfer flux, T_{ext} is the temperature in the laboratory, and h is the heat transfer coefficient, which must be determined experimentally. Table 2.3 displays typical values of h for different scenarios. Its value can go from 1 W m^{-2} K^{-1} to 100000 W m^{-2} K^{-1}, mostly depending on the surroundings (whether it is air, water, etc.) and on whether the corresponding fluid is driven or not (forced convection, free convection). A common situation in the lab would be air with free convection, with h being found in the range 2.5 – 25 W m^{-2} K^{-1} [11]. Additionally, including passive surrounding elements (such as holders, frames, housing, etc.) in the model is recommended to properly describe the heat losses, especially when a non-negligible amount of heat is absorbed by these parts.

2.6 Finite element software for AER modelling

FEM software, such as COMSOL Multiphysics or ANSYS, are well-suited tools to model EC devices thanks to their capability to solve physical phenomena in complex and elaborated structures. In addition, these structures are relatively easy to implement thanks to software's custom CAD-like geometry creation modules, allowing operations (merging, union, difference) of well-known regular shapes (squares, cylinders, rectangles, circles) in all three dimensions (1D, 2D, 3D). Besides, choosing the physical phenomena and boundary conditions of each domain selection is easy and convenient, and so it is the coupling of different phenomena that may coexist. This is a common scenario in fluid-based coolers, where the heat transfer and computational fluid dynamics (CFD) are deployed and coupled.

2.6.1 Getting started

The diagram in Figure 2.12 shows a typical FEM workflow model, displaying the different steps to be taken. First, the space dimensions must be selected. This typically ranges from 0D to 3D, and our choice will strongly depend on symmetries of our problem. In the case of an AER, 3D representations would be most suitable. However, 3D models require a lot of meshing points and are computationally very demanding. Thus, 2D representations of AER are interesting to be considered for more efficient computations, though it assumes that the width of the EC plates and fluid channels are infinite. This assumption is not true in reality, because the width of the EC plates is similar to the length and height of the AER. However, it is still an interesting approximation to consider. Note though that heat losses in the dimension that is not accounted for will not be considered in any case, and hence these models become more challenging to be predictive, requiring the fitting of more parameters.

The physics involved in an AER are heat transfer in solids, heat transfer in fluids and fluid dynamics. We can couple these phenomena by selecting either a laminar flow (if the Reynolds number $Re < 2100$) or a turbulent flow (if $Re > 2100$) in the conjugate heat transfer module [106]. The Reynolds number is given by:

$$Re = \frac{\rho u L}{\nu} \tag{2.30}$$

where μ, ρ, u, and L are the fluid viscosity, the fluid volumetric density, the fluid velocity and the geometry characteristic length, respectively. While heat transfer must occur in all geometry domains, the fluid dynamics module is only applied in the fluid selections. This is an important feature to double-check to avoid bugs and computation issues. Also, note that the "Heat transfer in solids and fluids" module does not allow the displacement of fluids, and hence, it is useless for a dynamic AER model if it is not coupled with a laminar or turbulent flow.

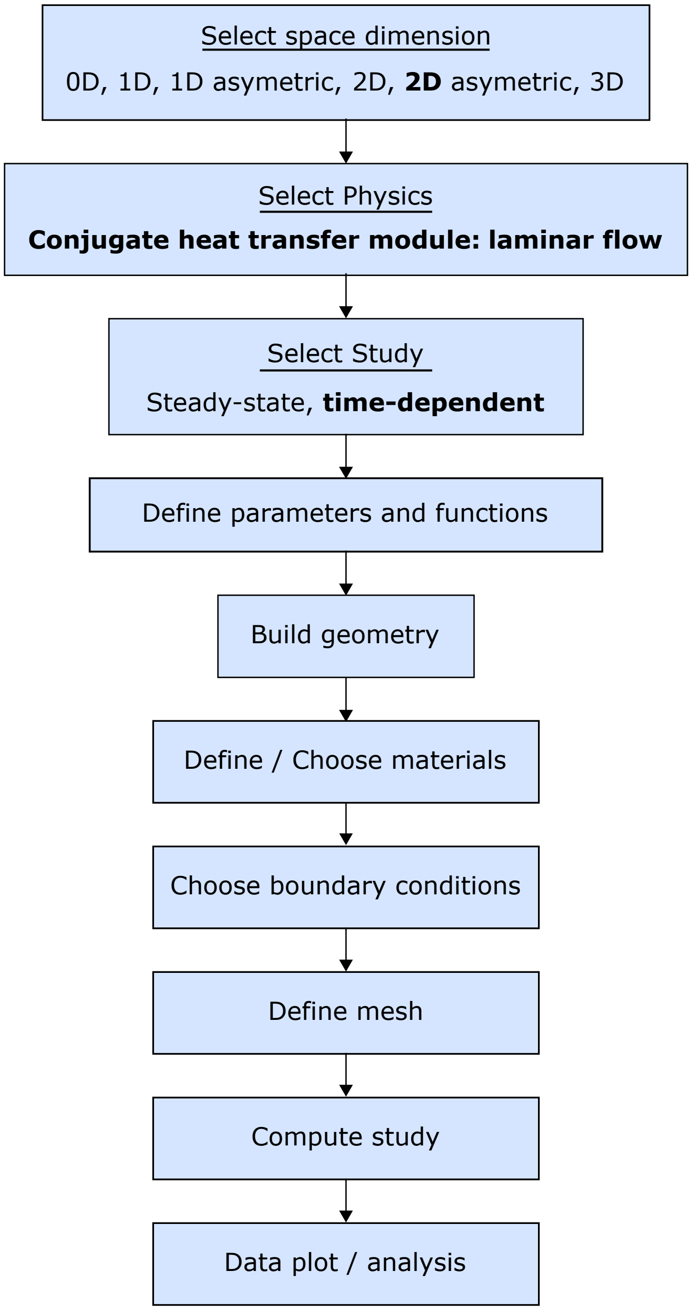

Figure 2.12 **Typical FEM diagram workflow.**

The following step consists of the kind of study to be run. General kinds include steady-state or time-dependent studies. Because the EC effect and fluid displacement obey time-dependent functions, the performance of an AER is better described with a time-dependent study. This allows one to visualize how heat is transferred from the EC material to the heat transfer fluid (and vice versa) and observe the creation of a gradient throughout heat regeneration. It is difficult to know initially at what time step the steady state will be reached, i.e., when the temperature difference between the hot and cold side of the AER becomes constant. Regarding the time-step of the calculation, the software will choose it automatically according to the model needs. It is possible as well to manually specify it. Note that time-dependent events like the EC effect might sometimes happen in a lower time frame than the integration time step, and hence will be completely neglected. In order to avoid that, it is recommended to manually set a constant time step $5 - 10$ times lower than the EC effect heat pulse duration (labelled in previous sections as t_{charge}), so that the solver can properly reproduce any defined profile. In addition, it is possible to force the solver to follow the defined time step more strictly. More elaborated solutions, as a time-dependent time-step or introducing “Events” are possible as well.

2.6.2 Defining the parameters

Although not necessary, it is extremely convenient to define all the model parameters. This includes material properties, such as thermal conductivity and specific heat but also geometrical variables, constants, or other magnitudes. By defining the parameters, the model becomes more robust and user-friendly. Moreover, if done properly, it becomes very straightforward to implement modifications of geometry, such as increasing length or height of a geometry entity, without causing distortions to the global one. Table 2.4 serves as an example of how this parameter definition looks like in the software.

Table 2.4 **Example of the definition of parameters in a COMSOL file**.

Name	Expression	Value	Description
Period	6 [s]	6 s	Cycle period duration
Flow_rate	25e-3 [L/min]	4.167e-7 m^3 s^{-1}	Maximum fluid volume flow rate
N_cycles	150	150	Total number of cycles
T_tot	Period*N_cycles	900 s	Total time duration

2.6.3 Building geometry

The AER architecture consists of a porous-like assembly of the EC material submerged in a fluid column. In EC, the porous-like structure consists typically of a parallel plate matrix because it is convenient and easy, even though other EC material assemblies should be in principle possible. A 2D representation of this structure is shown in Figure 2.13.

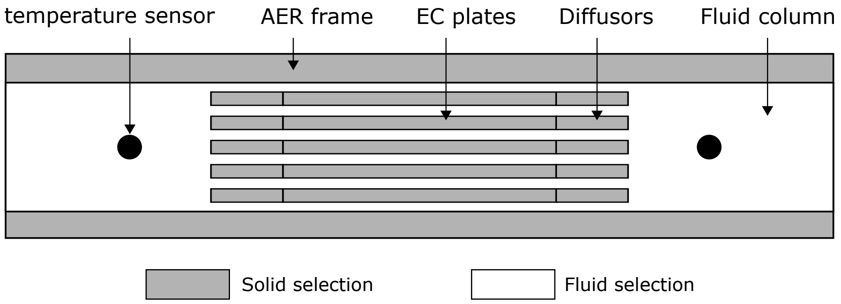

Figure 2.13 **A 2D representation of the AER parallel plate-based architecture |** It includes the EC material plates, the fluid column, the AER frames, the fluid diffusors (to ease the fluid pressure drop), and the temperature sensors (black circle). The grey shaded areas correspond to solid selections in the simulations, whereas the white area corresponds to fluid.

The necessary elements to model an AER are the fluid column and the EC material plates. Other elements, such as frames, holders, fluid diffusors, or shapes emulating the temperature sensors may be included for a better description of the experiment but they are not strictly necessary to simulate the operation of an AER. As already mentioned, the AER geometry is possible to be defined in 2D (if one assumes infinite length in the out-of-plane direction of the model), or in 3D. Because of the more demanding computation that 3D simulations entail, AER 2D representations are normally a good enough starting point. Note that it would not be the case if the plates were cylindrical or if other assemblies, such as sphere-beds, were used.

2.6.4 Defining materials

All geometrical domains need to be associated with a certain material. To do so, one needs to define the required material physical properties. For example, if a selection is subjected to heat transfer phenomena, the material properties needed to be defined are specific heat c_P, thermal conductivity k and volumetric density ρ. If fluid dynamics are involved, fluid viscosity μ is required too. These properties can take a constant value (a parameter), or a function, in case they depend on other variables (such as temperature or time, for instance). If these properties depend on a variable that is also involved in a differential equation (e.g., temperature in a heat transfer problem), the differential equation will become non-linear and its integration results more demanding to converge. This is the case as well in other terms of the heat transfer equation (external heat sources, for instance).

2.6.5 Initial values, boundary conditions and physical features

Before running the model, the initial values of the variables, boundary conditions and additional physical features need to be defined. In our AER example, we are going to set initial values of temperature (usually room temperature) and fluid velocity at 0 m s^{-1}. Secondly, we add a heat source at the EC plate domains to simulate the EC effect. Moreover, the user has to decide whether adiabatic conditions are to be set at the exterior walls, which is the default feature, or a heat flux instead, if heat losses to the surroundings are considered. Finally, an outflow boundary condition must be added at both fluid inlet and outlet. This is an open boundary condition that states that the only heat transfer occurring across the boundary is by convection, which is typically a good approximation in heat transfer models with fluid. As mentioned, the user has to specify in the heat transfer module which domains are solid and which domains are fluid. Likewise, it is important not to forget to apply laminar flow only to fluid domains, which might not necessarily be the case by default. Also, fluid inlets and outlets need to be added manually so that the motion of the fluid is monitored properly. In the inlet settings, we can define fluid inlet either as velocity (by specifying a normal flow velocity or a velocity field), as a pressure drop (we can choose to suppress fluid backflow), as a fully developed flow (by specifying an average velocity, a fluid flow or an average pressure), or as a mass flow. For the outlet boundary condition, it is preferable to set it with a pressure $p = 0$ Pa. If not, the continuity equation, which states that the fluid volume flux must be conserved, can be challenged, and the convergence of the integration can be compromised.

2.6.6 Mesh

Defining a proper mesh of points is an important feature of any numerical model because these are the points where equations are going to be integrated and a solution computed. Note that it is important to find the right balance between a) having enough points (so that the physical description is correct) and b) the minimum possible (so that our computation is more efficient). With FEM software, we can tune the element size parameters, such as the maximum element size, the minimum element size, the maximum element growth rate, as well as the shape of the mesh (rectangular, triangular, etc.) among other features.

Chapter 3

State of the art of EC prototypes

This chapter summarizes the performance and design of all EC coolers proposed to date. These prototypes are sorted into two main categories: those based on the circulation of an external fluid (Section 3.1) and those that utilize exclusively solid elements (Section 3.2); simultaneously, each prototype work is clustered into subsections according to the team or laboratory that produced it. Before the detailed description of each cooling device, a general analysis of fluid and solid-based prototypes is presented at the beginning of each section, highlighting their main achievements and pros and cons. Section 3.3 summarizes some numerical models of EC devices as well. The text of this chapter has been entirely taken from my first-author publication “EC coolers, a review” [70]. The electrocaloric prototypes in [5], [25] and [26] were published during the course of this dissertation. The last electrocaloric prototype in Section 3.1.3 [5] is described later in more detail as it constitutes the core of Chapter 4.

3.1 Fluid-based electrocaloric coolers

Prototypes utilizing a heat transfer fluid to pump heat are the most common kind of caloric coolers (including MC, EC and eC), and their vast majority are based on the active heat regeneration principle [5, 22, 34, 97].

Up to now, fluid-based EC prototypes have shown the best performances in terms of temperature spans and regeneration factors, proving that temperature differences larger than 10 K are possible. These kinds of prototypes remain still today the handiest ones because their principle is well known, thermal contacts are maximized by default and their structure is easier and simpler to implement. In addition, the resulting coolers are robust, what makes their industrial development more plausible. On the other hand, cooling powers in fluid-based prototypes have been scarcely reported, and those who did, did not show competitive figures. The reason is mainly due the dielectric fluids in use, exhibiting poor thermal properties that limit heat transfer. The utilization of water instead (which requires electric insulation of the EC samples and connections) is key to raise these values and reach performances in the same order than MC and eC devices, where cooling powers around $100 - 1000$ W kg^{-1} of caloric material have already been reported. In addition, thinner and more regularly shaped EC samples should enhance heat transfer, allowing for higher cycle frequencies and minimizing the contributions of parasitic heat losses. Similarly, prototypes' efficiency in fluid-based prototypes has not been investigated yet and magnitudes such as COP and COP / COP_{Carnot} have not been reported. The disadvantages of fluid-based prototypes are 1) the volume of inactive heat transfer fluid lowers performance and requires the presence of a pump, 2) higher cycle frequencies, which require large flow rates, are challenging to deploy because of the fluid nature and potential turbulence, which may enhance heat transfer but promotes degradation of the temperature gradient at the same time, and this is not desired. Despite these limitations, there is enough evidence to consider that fluid-based prototypes have still room for improvement, and that their performances have not reached yet their limit.

3.1.1 Moskov Power Engineering Institute prototypes

The first EC prototype dates from 1989 [60]. It was developed by Sinyavsky's team in Moskov Power Engineering Institute (MPEI) in collaboration with Shebanov, from Latvian State University. The EC material was 20 x 10 x 0.5 mm bulk plates of $Pb(Sc_{0.5}Ta_{0.5})O_3$ (PST) with an ordering degree of Scandium and Tantalum anions $\Omega = 0.8 - 0.9$. The material displayed a ΔT_{ad} of $1.3 - 1.5$ K under the application of $E = 25$ kV cm^{-1} at its optimal temperature $T_{op} = 274$ K. The EC prototype itself consisted of two main blocks, each made of 10 of PST plates, structured in a parallel plate matrix of 2 rows and 5 columns, with each block having a total PST mass of 7 g. A gap of 0.5 mm was set in between the PST plates to let a heat transfer fluid flow through. The two blocks operated with a 180° out of phase electric field and were connected in series in a closed fluid tubing with heat exchangers in between the blocks, as depicted in Figure 3.1.2a. The heat transfer fluid was Helium, which pressure was set at 0.8 MPa. The direction of the fluid circulation was alternated simultaneously with the applied field cycle, as required by the regenerative principles. The authors called their method quasi-regeneration. This device was able to build a temperature difference between the heat exchangers (temperature span) of 2 K and a cooling power of 10 mW for an electric field strength $E = 15$ kV cm^{-1} and a cycle frequency f of $3 - 5$ Hz.

An upgraded version following the same design and principle was presented a few years later, in 1995 [6, 61]. The PST plates where thinner (0.3 mm), and the total PST ceramic mass was increased (35 g). The fluid slits were thinner as well (0.05 mm) by using copper wires as spacers in between the plates. The heat transfer fluid was replaced by hexane, permitting higher electric fields to be applied. The resulting device produced a maximum temperature span of 5 K for an electric field of 60 kV cm^{-1}, which is about twice as large as the EC effect displayed by the EC material (considering that $\Delta T_{ad} = 1.5$ K at $E = 25$ kV cm^{-1}). In the same publication, the authors disclosed: "at their present time, a new model of a large scale electrocaloric cooler had been assembled". This new device consisted of a single unit of 400 g, made of 0.3 mm thick PST plates "modified by different elements" to achieve different optimum temperatures, similar fluid slit size (0.06 mm) and the same heat transfer fluid (hexane), but with a larger cross-section (11 x 11 mm) and a longer total length (300 mm). Preliminary results reported a temperature span of almost 8 K for an applied electric field of 15 kV cm^{-1} and a fluid flow rate of 2.5 cm^3 / cycle. The authors claimed that when increasing the field from 15 to 18.5 kV cm^{-1} (and we understand that keeping constant the other parameters as well, but this is not explicitly mentioned), they measured a temperature span of 12.7 K. Cooling power values were not reported for any of the two last versions. Regarding the electric consumption, 750 W were required to induce an electric field of 25 kV cm^{-1} in the material (unfortunately, the power for the electric fields of 15 and 18.5 kV cm^{-1} in the experiment was not disclosed). According to their calculations, the authors explained that such an electric field of 25 kV cm^{-1} (which was too high to be applied experimentally) should produce a temperature span in the device larger than 15 K. Up to now, this is the last communication that Sinyavsky's team disclosed on electrocaloric cooling and further works confirming these preliminary results have not been reported yet.

3.1.2 University Ljubljana prototypes

After the discovery of giant ECE in ceramic and polymers thin films in 2006 and 2008 [57, 58],the electrocaloric community underwent a renaissance that triggered the development of more EC devices [5, 7–9, 25, 26, 62, 64, 66, 67]. Andrej Kitanovski's group attempted in 2015 the first Slovenian EC prototype, which followed the principle of active regeneration [7]. The device was based on bulk $0.9\mathrm{Pb}(\mathrm{Mg}_{1/3}\mathrm{Nb}_{1/3})\mathrm{O}_3 - 0.1\mathrm{PbTiO}_3$ (PMN-10PT), presented in rectangular plates of $20 \times 10 \times 0.2$ mm^3 and stacked in a parallel plate matrix of 10 rows and 3 columns of these plates. The space between the rows for the fluid to flow through was set to 0.1 mm and the heat transfer fluid was dielectric silicone oil. For an applied electric field $E = 50$ kV cm^{-1} and a cycle frequency of 0.75 Hz, the device showed a maximum temperature span of 3.3 K, which is more than 3 times the ECE magnitude (around 1 K at room temperature). The authors showed as well the results of a 2D based dynamic numerical model which simulated the active electrocaloric regenerator (AER) performance of other heat transfer fluids. Their model showed that, by using deionized water, enlarging the AER length to 0.2 m and increasing both cycle frequency to 1.25 Hz and applied electric field to 118 kV cm^{-1}, the device should reach a temperature span of 14 K, which means a regeneration factor of almost 10.

In 2018, a very similar device was presented accompanied with a more detailed numerical modelling[65]. The experimental device consisted of 45 identical bulk PMN plates, distributed in a parallel plate matrix of 9 rows and 5 columns, with a total length of 110 mm (Figure 3.1.2b). In between the plates, 0.125 mm fluid slits were set. Contrary to the previous design, a heat exchanger was placed at the hot end of the AER (by means of a copper tube) and a thin-film heater in the cold end of the AER as a heat load to report on cooling power. This device achieved a maximum temperature span of 3.3 K for an applied electric field of 57 kV cm^{-1}, very similar to their design from 2015, for a cycle frequency of 0.65 Hz and the ratio of the fluid displaced over the total regenerator fluid volume, v^*, of 0.2. When turning the heat load on, with the same frequency but a $v^* = 0.4$, a maximum cooling power of 16 W kg^{-1} (of electrocaloric material) was measured at the same applied field, reducing thus the temperature span down to 1 K. The numerical modelling consisted of a 2D transient simulation of the AER's performance and included the effect of electric-polarization hysteresis and the effect of the irreversibility of the system for electric-energy recovery. Their model showed that, whereas the cooling power remained unchanged, the *COP* decreased between 10 and 15% when electric hysteresis was included in the model. This result was unexpected by the authors because of the slim hysteresis loop of PMN in comparison to other EC materials, such as $BaTiO_3$ or PVDF [78, 107], highlighting the need to include these irreversibility to properly predict the efficiency of AER cooling devices. The model showed as well that by assuming 100% electric charge recovery, the *COP* was enhanced by a factor of 10. The study ended with an experimental verification of the numerical modelling, for which heat losses to the surrounding where considered. Even though the experimental data was not match because none of the parameters was adjusted to do so, the model was able to properly describe the trends of the temperature span versus v^* parameter and cooling power versus temperature span graphs.

3.1.3 Luxembourg Institute of Science and Technology prototypes

The first cooler from Luxembourg Institute of Science and Technology (LIST) was presented in 2016 [67]. It was conceived to validate the basic principle of passive regeneration, i.e., to create a thermal gradient in a fluid column. The prototype was based on commercially available Zr-doped $BaTiO_3$ (Zr-BTO) MLCs, each being 3.2 x 2.5 x 2 mm^3 and 0.087 g, which exhibited an ECE of 0.54 K at 200 V. Three plates of 5 x 10 BTO-MLCs (making a total of 150 MLCs) were attached to copper foils and displaced throughout a fluid column containing dielectric fluid silicone oil (Figure 3.1.2c). The movement of the plates was

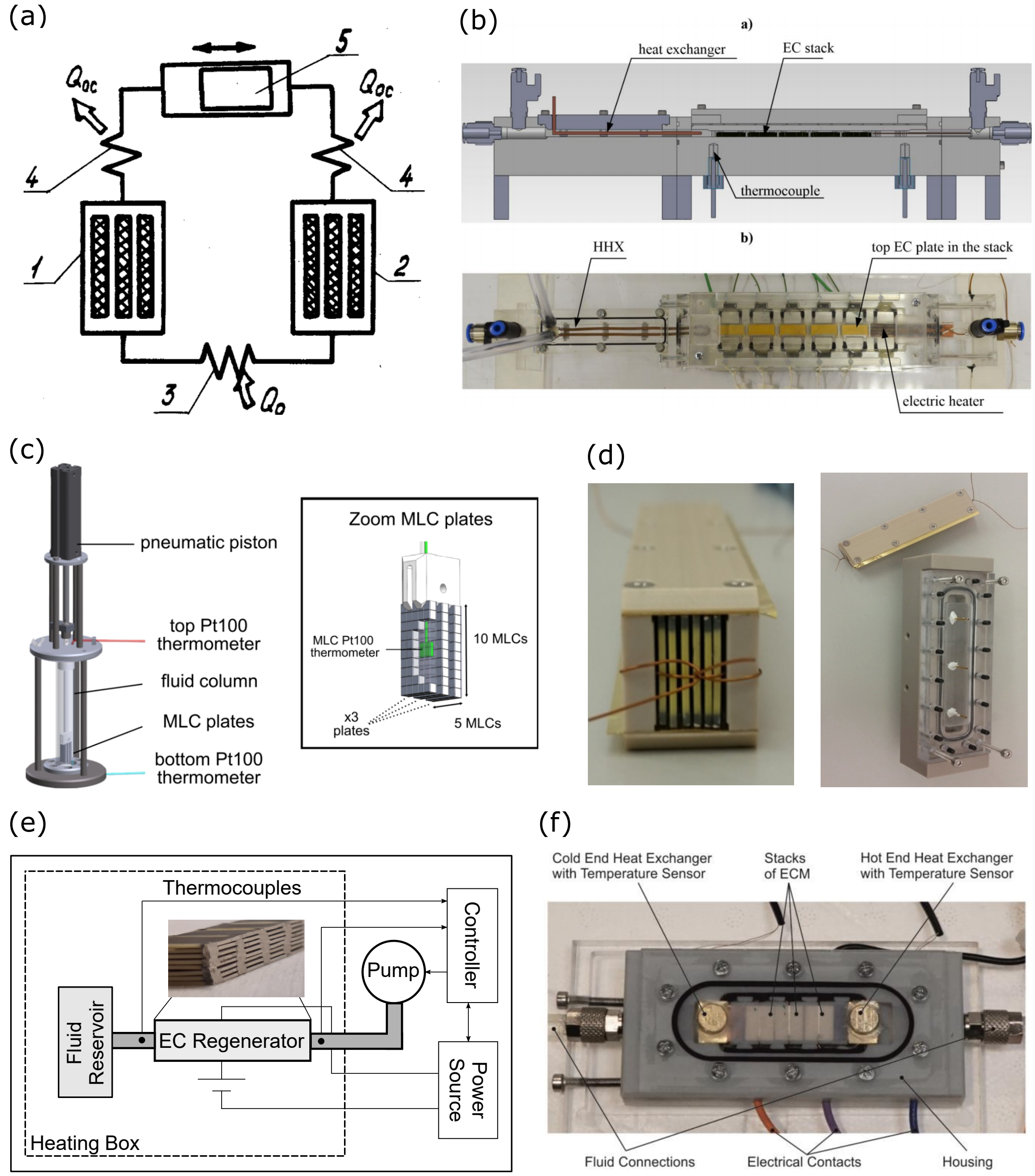

Figure 3.1 **Fluid-based EC prototypes |** (a) Sketch of Sinyavsky's first prototype, based on modified-PST plates with hexane as a heat transfer fluid. The two blocks worked in an anti-phase fashion (called quasi-regeneration by the authors). Such a device achieved a temperature span of 5 K. (b) Zenithal image of U. Ljubljana's prototype, with 5 EC stacks, each formed by 10 PMN-PT plates, and the hot side heat exchanger (HHX) and the electric heater in the cold side. (c) LIST's first device based on passive regeneration with commercial BTO-MLCs and silicone oil. (d) LIST's first active regenerator based on PMN-MLCs from Murata. The figure on the left shows the PMN-MLC matrix, whereas the image on the right shows the EC capsule that sealed and thermally insulated the system. (e) LIST's second active regenerator, with 128 0.5 mm thick PST-MLCs from Murata and silicone oil. The simplification of the structure and reduction of the inactive mass allowed the device to reach 13 K of temperature span. (f) Blumenthal's prototype based on customized PMN-MLCs and silicone oil. More details about these prototypes can be consulted in Table 3.1.

carried out with a pneumatic piston. Thermocouples placed at the top and bottom of the fluid column measured a maximum temperature span of 0.13 K when 200 V were applied to the 150 EC samples, which is an electric field $E = 200$ kV cm^{-1}. As described in detail, the thermodynamic cycle the device underwent consisted of a modified Brayton cycle, constituted of 2 adiabatic legs, two iso-field legs in stationary position and two iso-field legs during the plate's movement. According to the authors, the optimal frequency of 25 mHz was a clear indicator of the poor heat exchange of the overall system, which forced the duration of the iso-field legs to be excessively long (37 s) in comparison to the adiabatic legs (1.3 s), and justified the low regeneration factor (< 1), even though their hypothesis of creating a thermal gradient in a fluid column was successfully proved.

An active electrocaloric regenerator (AER) inspired by previous works was attempted in 2017 [7, 61], with a parallel plate matrix of 10 columns and 6 rows of PMN-MLCs fabricated by Murata Electronics Ltd (Figure 3.1.2d) [90, 91]. Each MLC was 10.4 x 7.2 x 1 mm^3. This parallel plate matrix was assembled within a rectangular casing formed by 4 polyether ether ketone (PEEK) plates, with grooves symmetrically spaced to support the MLCs in two of these plates. Bespoke shaped brass plates were placed at the edges of the grooves to ensure mechanical locking of the MLCs and provide electrical connection at the same time. The resulting cell was fitted into an outer PEEK housing that provided sealing and thermal insulation. A maximum temperature span of 1.4 K was measured in the AER at 700 V ($E = 180$ kV cm^{-1}), which triggered $\Delta T_{ad} = 1.6$ K in the material. Despite the improvements with respect to the first design, such as utilizing a larger EC material mass with higher EC effects, heat exchange was still compromised because of MLCs' large thickness and fluid slits irregularities (Figure 3.1.2d).

Recently, an evolution of this AER has been carried out with thinner PST-MLCs (0.5 mm) [5]. The final parallel plate matrix consisted of 128 samples, distributed in 8 rows and 16 columns (Figure 3.1.2e). The fluid slits between the PST-MLCs rows were set to 0.25 mm. Fluid slits irregularities were still present because of the uneven and curved shape of the EC samples at such low thickness, but improved in respect to the previous device. The design was based on a 2D finite element model, which provided important insights on the role of thermal insulation and inactive mass. As a result, none of the structural pieces and EC housings parts from the previous prototype were utilized. Instead, double-sided tape stripes were used to assemble the parallel-plate matrix and silver paste applied at the PST-MLCs electrode terminals to connect all MLCs in parallel. A polyolefin hose was used to encapsulate the AER and minimize dead volume, simplifying as much as possible the overall design. Polyurethane foam was eventually applied to improve thermal insulation. This prototype produced a temperature span of 13 K after 2000 s of operation for an applied voltage $V = 600V$ (E = 160 kV cm^{-1}). This result, which entails a regeneration factor of 6, remains today the maximum temperature span ever observed in an EC cooler. An extra AER, made of 8 columns and 4 rows of 1 mm thick PST-MLCs and a wire at the cold side, was built to collect cooling power values reaching 12 W kg^{-1} (of electrocaloric material) for a temperature span of 0 K. The same numerical modelling was adjusted to predict the performances of this AER. This model foresees that, by thinning the MLCs down to 0.2 mm, by utilizing water as heat transfer fluid and by utilizing better ordered PST in the MLCs activated close to their current breakdown field (ECE of 5.5 K) [12], a maximum temperature span of almost 50 K and a maximum cooling power of 850 W kg^{-1} (of active EC material) should be obtained. This outcome is similar to Kitanovski's model, stressing out the importance of utilizing water as a heat transfer fluid and increasing the sample breakdown in order to be able to apply higher EC effects without compromising the viability of the samples.

3.1.4 Leibniz Universität Hannover prototypes

The last European fluid-based EC cooler to be described was developed by Blumenthal and Raatz in 2018 (Figure 3.1.2f) [8]. The authors presented a new AER based on PMN-8PT MLCs with the aim to produce a small-scale desktop cooling device, robust, reliable and able to display a temperature span larger than 1 K. Their approach was based on the well-known V-Model (a standard tool in engineering systems and software development) in which the classification of device types, influencing factors and numerical simulation methods are integrated altogether to identify favorable geometrical and operating parameters. The PMN-8PT MLCs samples were 10 x 8 x 0.45 mm^3, with 47 μm-thick inner ceramic plates. They were fabricated in IKTS Fraunhofer. The AER parallel plate matrix consisted of 3 columns x 5 rows, structured with 3D-printed supports and housing. Even though ideal fluid spacing derived by their model was 0.19 mm, a larger one of 0.3 mm was experimentally introduced to diminish the effect of uneven plates, fragile electrical joints, and electrical shorts due to enclosed air bubbles. The fluid was a dielectric silicone oil. To increase the device's practical lifetime, the cooler was operated only at low electric fields $E = 32$ kV cm^{-1}. At this applied field, the material showed an ECE of 0.39 K and the device a maximum temperature span of 1.12 K when optimized (cycle frequency of 0.3 Hz and 80% of fluid displaced). This corresponds to a regeneration factor of 3, in agreement with previous works based on the same principle and utilizing similar materials [7, 65]. The authors emphasized as well that after more than 2000 h of operation, the device was still able to operate without any failures, proving its robustness.

Table 3.1 **Summary of the features and performances of all experimental EC fluid-based coolers proposed to date.**

Inst.	Ref.	EC material	m_{EC} [g]	E [kV cm^{-1}]	ΔT_{ad} [K]	Fluid	ΔT_{span} [K]	q_c [W kg^{-1}]	q_c [W L^{-1}]
MPEI	[60]	PST bulk	14	15	1.5a)	Helium	2	0.7	6
MPEI	[6]	PST bulk	35	60	-	Hexane	5	-	-
MPEI	[61]	PST bulk	400	18.5	1.5	Hexane	12.7	-	-
U. of Ljubljana	[7]	PMN bulk	10	50	0.9	Silicone Oil	3.3	-	-
U. of Ljubljana	[65]	PMN bulk	14.6	57	1	Silicone Oil	3.3	15c)	122c),e)
LIST	[67]	BTO-MLCs	13	200	0.5	Silicone Oil	0.16	-	-
LIST	*	PMN-MLCs	35	175	1.7	Silicone Oil	1.4	-	-
LIST	[5]	PST-MLCs	42	160	2.2	Silicone Oil	13	12d)	105d)
LIST	[5]	PST-MLCs	42	160	2.2	Silicone Oil	13	12d)	105d)
U. Hannover	[8]	PMN-MLC MLCs	4.5	32	0.39	Silicone Oil	1.12	-	-
UTRC	[108]b)	PVDF-MLCs	-	1500	8.9	Air	8.4	-	-

*a) for an E = 25 kV cm^{-1}; b) not peer-reviewed; c) for a T_{span} = 1 K; d) for a T_{span} = 0 K, obtained with a different prototype of m = 19 g and E = 37.5kV cm^{-1}; e) We used PMN bulk density of 8.13 g cm^{-3} [109];

3.1.5 United Technologies Research Center prototypes

In the last years, the United Technologies Research Center has been developing fluid-based EC devices for both cooling and heating purposes. The project, founded by the U.S. Department of Energy's Office of Energy Efficiency and Renewable Energy (EERE), has not been published in peer-review journals, but a summary report is available online describing their progress and results [110]. In this document, Annapragada et al. showed that their heat pump was based on inexpensive polymer EC materials able to display a ΔT_{ad} = 8.9 K at 43°C and close to breakdown field (1500 kV cm^{-1}). Under such conditions, their device was able to cool ambient air by 8.4 °C (the hot side did not change its temperature because of a hot bath). However, this temperature span of 8.4 °C could not be maintained because the high electric field led to electric breakdown in some of their samples. Unfortunately, more details on the experimental parameters and geometric dimensions were not disclosed.

3.2 Solid-based electrocaloric coolers

Although nine solid-based prototypes have already been presented, they remain a less common and known type in the caloric materials field. Their performances in terms of temperature span have not been as impressive as the best fluid-based, with none of them crossing yet the 10-K barrier (though 8.7 K have been recently reported). However, the amount of active mass used in these works has been exceptionally low (cf Table 3.2) and higher temperature spans are soon expected if researchers make it possible to stack more stages in their prototypes. On the other hand, the lack of a fluid media has permitted conducting more accurate and reliable analysis on cooling power (and thus efficiency), reporting up to 2800 W kg^{-1} of EC material and $COP \sim$ 10 ($COP_{Carnot} \sim$ 10%). These numbers are equivalent to the ones displayed by the best eC and MC coolers.

Of particular interest are the multistage and cascading designs, which seem to be the most adequate working principle for solid-based devices because they do not require any external element to pump heat and the activation mechanisms have negligible power consumption. While these approaches are unique and very promising, the engineering of their designs is complex and delicate, and there are still some limiting factors that should further be improved such as the high thermal resistance typically seen in solid-solid interfaces due to poor thermal contact. A solution to that are flexible surfaces bounded by electrostatic attraction, as PVDF can provide, but even in these cases heat transfer remains limited by the low thermal conductivity of EC materials [95]. Higher thermal conductivities should enable employing higher cycle frequencies and lowering the contributions of parasitic heat losses. At the same time, the latter can be reduced by developing better insulation, such as vacuum surroundings. To increase cooling power, thicker samples could be needed, although this implies higher applied voltages if multilayers samples are not contemplated and degradation of heat exchange [95].

3.2.1 University of California prototypes

After the discovery of serendipity EC effects in commercial $BaTiO_3$-based MLCs [63], the department of mechanical and aerospace engineering of University of California designed a solid-state refrigerator based on these same samples. The device consisted of a single stage, formed by one BTO-MLC, oscillating between a heat source and a heat sink thanks to the action of a motorized z-stage, as depicted in Figure 3.2.5a. The key element of their work were switchable liquid-based thermal interfaces, which permitted fast and reliable heat transfer between the EC MLC and the source/sink. These thermal interfaces were formed by dispensing glycerin droplets onto previously patterned hydrophilic islands (diameter < 1 mm) on the backside of the heater and the top surface of the heat sink. A constant Joule-heating current kept the heater temperature at 27 °C, while the heat sink was maintained at 25.7 °C (they did not mention how). For an applied frequency of 0.3 Hz and an electric field of 300 kV cm^{-1} (which induced an EC effect in the BTO-MLC of 0.5 K), the temperature of the heater was cooled down by 1 K (26 °C). Considering that 15 mW of Joule-heating were applied at the heater and that the mass of 1 single BTO-MLC is around 0.1 g, we can deduce a cooling power of 160 W kg^{-1} of EC material. The authors explained that their experimental results were supported by a 1-D numerical model, though the latter was not displayed.

3.2.2 Penn State University prototypes

In 2013, Qiming Zhang's group from Penn State presented the first solid-based regenerator [64]. This device consisted of 0.25 mm thick rectangular EC modules that were sandwiched in between four 0.5 mm thick stainless-steel plates (Figure 3.2.5b). The inner structure of these EC modules was made of 24 PVDF 8 µm-thick films (similar to MLCs), with gold sputtered electrodes. Glued thin silver wires were then connected to them to carry electric current. Ultimately, the films were glued on top of each other with epoxy resin, forming a 1-micron layer in between the films. The overall EC module showed 2.5 K of adiabatic temperature change at 35 °C under an electric field of 1000 kV cm^{-1}, which differs from the more than 20 K of temperature change that thinner films of the same PVDF displayed under 1600 kV cm^{-1} [82]. According to the authors, the reason for that was the inactive mass (electrodes, wires, glues, resins, etc.) that the EC module encloses. The resulting device followed then the principle of passive regeneration, in which the stainless-steel plates were moved back and forth through the EC modules synchronously with the activation and deactivation of the EC effect. As a result, a 6.6 K temperature span was measured between the ends of the stainless-steel plates at a frequency of 1 Hz and an electric field of 1000 kV cm^{-1}, which corresponds to a regeneration factor of 2.6.

A second solid-solid EC device from Qiming Zhang's group was proposed in 2017, utilizing commercial Y5V ceramic MLCs [94]. The device consisted of a novel regenerative design formed by two adjacent rings (Figure 3.2.5c), each constituted of 12 trapezoid-like shaped MLCs (named EC elements in the figure, with the bases of these trapezoids being 12 and 5 mm, the height 5 mm and the thickness 0.46 mm). Fixed heat exchangers were placed at the ring ends representing the hot side (red coloured, where heat is rejected) and the cold side (blue coloured, where heat is absorbed). To accomplish solid to solid regeneration, 1) the two rings are rotated in opposite direction and 2) the electric field is only applied in the regions where the EC elements rotate from the fixed hot heat exchanger to the fixed cold heat exchanger (highlighted semicircle in the figure). Since the rotation direction is different for each ring, these highlighted areas become complementary to each other, as depicted by the right image of Figure 3.2.5e. Such device displayed an EC effect of 0.9 K at 200 V (E = 165 kV cm^{-1}), and the maximum temperature difference between the hot and cold heat exchangers measured was 2 K at a rotation speed of 5 rounds per minute.

3.2.3 Palo Alto Research Center prototypes

David Schwarz's group in the Palo Alto Research Center (PARC) has been developing solid-based EC coolers since 2015. In their first prototype, a heat-switch-based electrocaloric cooler utilizing commercial BTO based MLCs was presented (Figure 3.2.5d) [66, 104]. The active part of the device consisted of a 4 x 5 BTO-MLC array (labelled EC module in the figure), with each BTO-MLC being 3.3 x 1.9 x 2.6 mm^3. Bespoke heat switches were placed in between the EC module to pump heat from a source (a resister heater on the top of the structure) to a sink (copper block at the very bottom). To change the conductance of the heat switch from a high to a low value, the match and mismatch of patterned grooved silicon parts (blue elements in the figure) was attempted by displacing an actuator that attached with a hook, as depicted by the figure. As a result, the BTO-MLCS are in thermal contact either with the heat sink or the heat source depending on the position of the actuator. In the figure, the blue elements representing the heat switch are matched between the BTO-MLCs and the copper block (heat sink). At an applied electric field of 277 kV cm^{-1} and a temperature change in the EC module of 0.5 K, such a cooler was able to build a maximum temperature difference between heat source and sink of 0.3 K. This value is understandable since no regeneration nor multi-staging was performed to enlarge the temperature span. When activating the heater, a maximum cooling power of 36 mW was observed at 0 K temperature span (q_c = 19 W kg^{-1}). In addition, the device showed a robust and reliable performance by being able to operate > 10 h without failure.

With the aim to improve the temperature span of their device, the same group presented a new device based on the cascading principle (Figure 3.2.5e) [25]. This time, the EC material was PST-MLCs from Murata (each 10.4 x 7.2 x 1 mm^3) that showed an EC effect of 2.5 K at the applied electric field E = 108 kV cm^{-1}. The design of the cooler consisted of two rows of PST-MLCs, thermally coupled, so that heat could be easily transferred from one to the other. The top row had 5 PST-MLCs and the bottom one 4. In addition, the latter contained aluminum plate-fin heat sinks (hot end, yellow square) and left side (cold end, gray square) to facilitate achieving stable temperatures at the right side. A miniature fan was placed at the hot side to facilitate the release of heat when reporting on cooling power. In the figure, the PST-MLCs are represented either by black squares (meaning that no field is applied) or red squares (a field is being applied). To pump heat from the source to the sink, the PST-MLCs were moved laterally relative to one another as the polarizing electric field was switched. At the applied field of 108 kV cm^{-1}, a temperature difference between the heat sink and the heat source of 5.2 K was measured at no-load conditions for a frequency of 0.15 Hz. Even though the prototype's temperature span did not cross the 10 K barrier, it is rather impressive to see that such performance was only achieved with 4.5 g of EC material (9 PST-MLCs of thickness 1 mm). Evidently, higher temperature spans could be easily achieved by inserting more PST-MLCs in the row. To achieve maximum temperature span, hot and cold ends were fully insulated and the fan in the hot side removed. To measure the cooling power, an electric heater was attached to the cold end and the fan was activated so that the temperature of the sink (hot side) was maintained near ambient temperature. Under these conditions, the corresponding maximum cooling power (temperature span T_{span} = 0 K) measured was 85 mW. It is important to notice as well that the PST-MLCs used were not optimized for such design. Hence, fabricating PST-MLCs with the same form factor as the previously used commercial BTO-MLC and orienting the electrode plates parallel to the heat transfer direction should substantially improve the performance [25]. Finally, a COP / COP_{Carnot} of 20% was reported from a linearized efficiency model derived in the paper, which, when considering Brayton cycles, was reduced to 11.5% (assuming 95% of charge recovered) and 15.5% (with 98% of the charge recovered). Their calculations excluded the mechanical work required to move the reciprocating system, which was considered negligible because it is orders of magnitude smaller than the other work contributions. The authors finalized the article mentioned that "Our estimate of the COP / COP_{Carnot} of the current design (. . .) shows that up to 56.4% may be achievable with the existing PST material. These values could make our system competitive with vapor compression cooling".

3.2.4 Luxembourg Institute of Science and Technology University of Cambridge prototypes

In 2018, Defay's group in Luxembourg Institute of Science and Technology developed a solid to solid-based EC device with the collaboration of the University of Cambridge. Although the main goal of the device was to enhance the overall device efficiency by recovering the charge employed in the EC effect, it is also another example of solid-solid EC prototype [50]. The device, which is sketched in Figure 3.2.5f, consisted of two plates, each containing 12 commercially BTO-based MLCs, that oscillated alternately in between two copper heat sinks and a copper heat load thanks to the action of a motor (slapping machine). In such scenario, the load could be cooled by 0.26 K because 1) heat regeneration was not implemented and 2) the used MLCs exhibited a low EC effect (0.3 K at 70 V), whereas the temperature of the heat sinks (T_h) remained to be the starting temperature because each sink was sufficiently massive [50]. The measured heat pumped was 113 mJ per half cycle, which corresponds to a cooling power of 12.7 W kg^{-1} considering that each plate had a total mass of 0.68 g and period 26.46 s (13.23 s each half cycle). After including and electric circuit to recover the charge by transferring the charge from two capacitors that operated in anti-phase, the measured *COP* of the device increased almost a factor of three, from 2.9 to 8.4.

3.2.5 University of California prototypes

Pei's group in the University of California presented in 2017 an EC prototype that did not require the circulation of a fluid nor the presence of extra solid elements to pump heat [9]. Instead, they made use of electrostatic interaction to quickly move a flexible EC element between a heat source and a heat sink, as the two images in Figure 3.2.5g display. The EC element (EC polymer in the figure) consisted of two 30 µm-thick PVDF layers of area 7 x 3 cm^2 sandwiched in between electrodes (active area of 5 x 2 cm^2) with one side clamped at the heat sink and the other at the heat source. When the field is applied, electrostatic interaction brings the film in contact to the heat sink (top image in Figure 3.2.5g). When the field is removed, the film remains in contact with the heat source thanks to its flexibility (bottom image in Figure 3.2.5g). By doing this, almost the entire surface of the EC polymer stack is successfully put in thermal contact with either the sink or the source. Hence, heat flow and cooling power are maximized. At the applied field of 667 kV cm^{-1} (2000 V), such a device was able to reach a cooling power of 2800 W kg^{-1} (about 150 times higher than previous works) and a measured *COP* of 13 without recuperating the energy in the depolarization process (the electric work was measured with an oscilloscope). Considering that the temperature span was 1.4 K, this supposes a COP / COP_{Carnot} ratio 6.1%. When the aluminum heat sink and heat source were replaced by carbon nanotube–coated polyethylene terephthalate (PET) films (thickness of 100 mm), the temperature span increased to 2.8 K [9], although the values of cooling power and *COP* were not reported in this case.

In 2020, an upgraded version of this work was presented [26]. The authors developed a cascade EC cooler with the aim to increase the temperature span of their previous device. In addition, the authors also integrated energy recovery to enhance the overall efficiency. The device consisted of four units of EC polymer stacks with the same electrostatic actuation described above, placed one on top of the other (Figure 3.2.5h). A heat flux sensor was attached between the heat source and the EC polymer laminate. To measure maximum cooling power, a fin cooler was attached to the heat source, and a thick Aluminum block (6.3mm) was the heat sink. Differently, to measure the maximum temperature span ($q_c = 0$), the loads were removed, and the bottom steel shim electrodes were replaced with thermally less conductive polyethylene terephthalate (PET) films. To pump heat from the source to the sink 1) adjacent EC polymer stacks were operated in an anti-phase manner (in the figure, field applied to the EC polymer stacks in red, and not applied to the ones in blue, and vice versa), 2) the system oscillated between the two states shown in the images in Figure 3.2.5h. Furthermore, with this anti-phase operation, charge can be transferred from one EC unit to the adjacent one, permitting the efficiency to be enhanced as shown previously [50]. By doing so, the authors could recover up to 70% of the electric work, reducing it from 29.2 mW cm^{-2} to 8.76 mW cm^{-2}. For an electric field applied of 600 kV cm^{-1} ($V = 3000$ V), each EC unit displayed an adiabatic temperature change of 3.0 K, and the device was able to amplify it by showing a maximum temperature difference (no load conditions) between the heat sink and the heat source of 8.7 K, which is remarkable considering that only four layers of PVDF with a total EC mass of 0.92 g were used (here we assume that each polymer stack has the same mass of 0.23 g reported in their previous work) [9]. After obtaining a good agreement between experimental data and simulations, their model predicted temperature spans of respectively 12 K and 14 K for six- and eight-layer prototypes. Returning to the 4-layer device, a maximum cooling power of 90 mW cm^{-2} (2140 W kg^{-1}, considering a total polymer stack area of 21.6 cm^2 from their previous work) [9] was measured at 0 K temperature span, and the corresponding *COP* was 10.4. For a temperature span of 2.7 K, the cooling power was 78.5 mW cm^{-2} (1850 W kg^{-1}) and the *COP* 9.0 (COP / COP_{Carnot} = 8%). A numerical modelling based on real device operation scenarios showed that the COP / COP_{Carnot} ratio peaked at 12% for a temperature span of 6 K and a *COP* of 6. In comparison, their simulations showed a maximum COP / COP_{Carnot} of 3.8% for the unit device, different than the 6% reported in their previous work [9]. In all *COP* calculations, the authors assumed the charge recovery of $\sim$ 70% that they showed beforehand.

Recently, Pei's group has proposed self-actuating EC fibers as a new potential kind of cooling device [112]. The fibers are composed of spray-coated PVDF on a conductive fiber that acts as core electrode. The outer electrode is obtained by coaxially coating single-

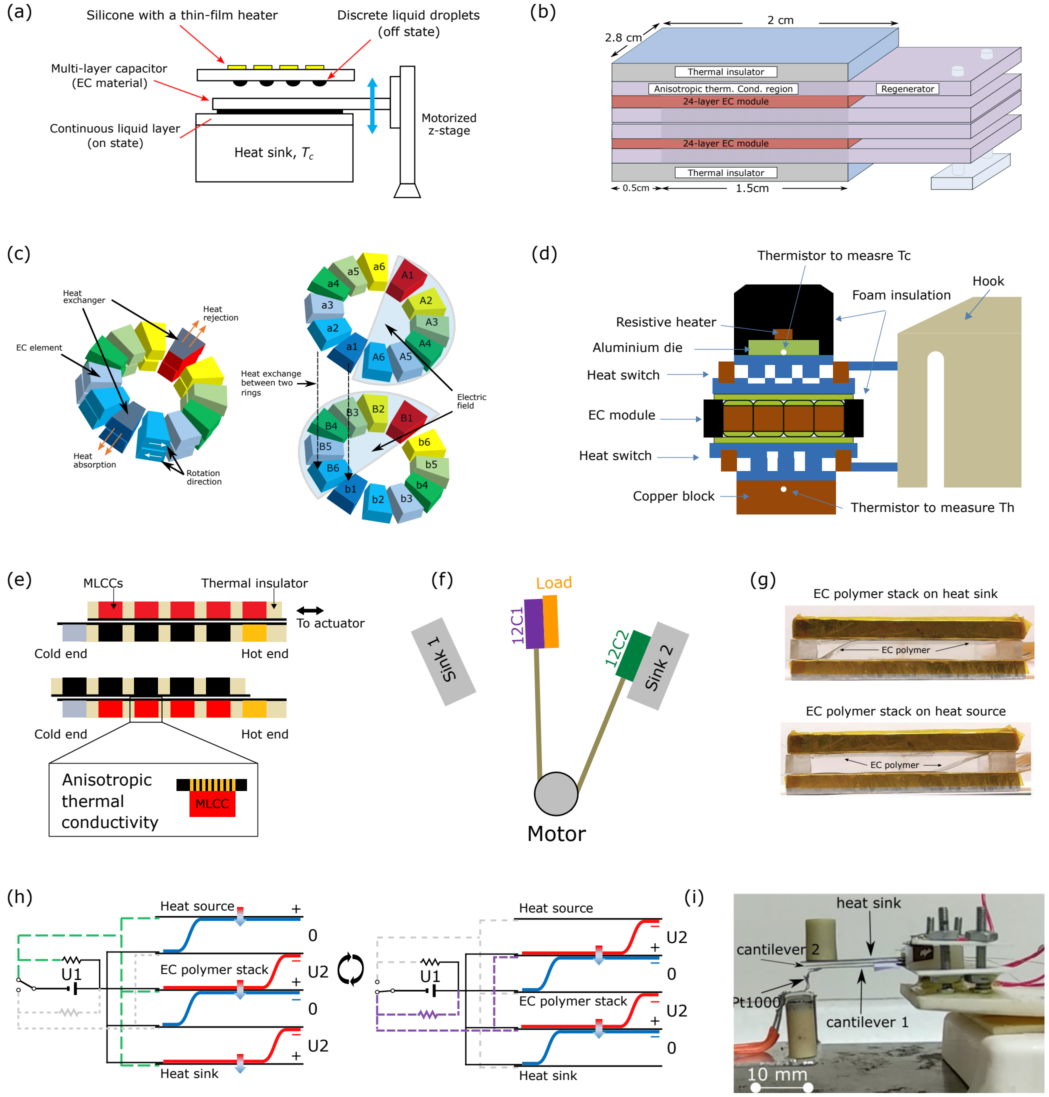

Figure 3.2 **Solid-based EC prototypes |** (a) Jia et al. first EC solid-based prototype, where BTO-MLCs oscillate between a heat source and a heat sink (b) Penn State solid-solid heat regenerator. PVDF plates moved in an oscillatory manner through stainless steel plates. (c) Penn State rotatory EC prototype based on commercial trapezoid-like shaped BTO-MLCs with cascading principles. (d) PARC's EC cooler with heat switches, based on commercial BTO-MLCs (e) PARC's second cooler based on PST-MLCs and cascading principles. The device reached a temperature span of 5.5 K with only 9 MLCs. (f) LIST and University of Cambridge's cooler based on commercial BTO-MLC. (g) Pei's first prototype based on PVDF-MLCs and electrostatic actuation. (i) Josef Stefan Institute's cantilever EC prototype made with PMN-PT. More details in Table 3.2.

Table 3.2 **Summary of the features and performances of all experimental EC solid-based coolers proposed to date.**

Inst.	Ref.	EC material	m_{EC} [g]	E [kV cm^{-1}]	ΔT_{ad} [K]	ΔT_{span} [K]	q_c [W kg^{-1}]	q_c [W L^{-1}]
Penn State University	[64]	PVDF-MLCs	-	1000	2.25	6.6	-	-
Penn State University	[94]	BTO-MLCs	9.84	165	0.9	2	-	-
PARC	[66, 104]	BTO-MLCs	$1.88^{a)}$	277	0.5	0.3	$19^{b)}$	$110^{b)}$
PARC	[25]	PST-MLCs	4.73	108	2.5	5.2	$18^{b)}$	$140^{b)}$
LIST and U. of Cambridge	[50]	BTO-MLCs	1.36	77	0.21	0.26	12.7	78
U. of California	[62]	BTO-MLCs	0.094	300	0.5	$0.9^{c)}$	160^{d}	$1048^{d,e)}$
U. of California-Pei's group	[9]	PVDF-MLCs	0.23	667	3.6	1.4 (2.8)	2800	$5000^{f)}$
U. of California-Pei's group	[26]	PVDF-MLCs	$0.92^{g)}$	600	3	8.7	$2140^{b)}$	$3745^{b),f)}$
Jozef Stefan Institute	[111]b)	PMN-PT	-	45	0.5	0.05	-	-

*a) Deduced from multiplying the number of samples by the mass of 1 BTO-MLC. which is 94 mg [63]; b) Cooling power at no-load conditions, i.e., T_{span} = 0; c) Temperature difference that the heater is cooled down; d) Includes cooling by mechanical motion; e) V_{MLC} = 13.4 mm^3 [63]; f) assumed PVDF density of 1.75 g cm^{-1}; g)Refers to the whole EC polymer stack;

walled carbon nanotubes on PVDF surface to keep the fiber flexible. After this process, the resulting EC fibers have a diameter of around 160 μm and are 8 cm long. The interesting feature of this kind of object (for which an ECE of 0.7 K has been reported at 1000 kV cm^{-1}) is its self-actuation effect, allowing it to commute between two different places, i.e., a heat source and a heat sink, without diminishing the EC performance. More interestingly, this avoids the use of any other additional driving mechanisms, such as pumps, motors or moving stages. Although the idea is still embryonic and unripe, these self-actuating EC fibers let envision the first ever active cooler in a thin fiber form factor, as the authors quoted.

3.2.6 Jožef Stefan Institute prototypes

Based on previous theoretical studies utilizing finite-element modelling [113], a cascade of two cantilevers made of bulk PMN/Pt/PMN (Figure 3.2.5i) was presented by Barbara Malic's group in 2021 [111]. Similarly to Pei's work, the system takes advantage of the electromechanical (EM) effect to bend the samples upon application of an electric field and establish this way the required thermal contact to pump heat according to the cascading principle. Although previous simulations predicted a temperature span of 12.6 K in a 15-stage system (the EC effect of their samples was of 1.2 K, entailing a regeneration factor of more than 10) [113], the presented 2-stage experimental cascade exhibited a maximum temperature span of 0.05 K at 45 kV cm^{-1} and frequency of 1 Hz, which was found to be the optimal. At this applied field, the cantilever underwent an ECE of 0.5 K so that a regeneration factor of 0.1 was deduced. The authors explained that the difference between theory and experiment was caused by poor thermal contacts induced by surface roughness and bending radius of the cantilever, and by the limited frequency of 1 Hz, which was found to be optimum above 50 Hz in the modelling studies. Another important consideration that the modelling showed is that, under realistic conditions, a certain critical amount of active EC mass is needed to overcome the losses to the environment, implying that a device made only of 2 stages would never be enough. This issue is recurring in EC prototypes, where the desire to develop low-scale and miniaturized devices pushes them to be as small as possible.

3.3 Numerical models

In this section, some of the numerical modellings on EC coolers are reviewed. They include both fluid and solid-based.

3.3.1 Guo et al.

In 2014, Guo et al.[2] presented a 3D model of a fluid-based micro-scale AER utilising finite elements (COMSOL Multiphysics software) (Figure 3.3). The AER parallel-plate matrix

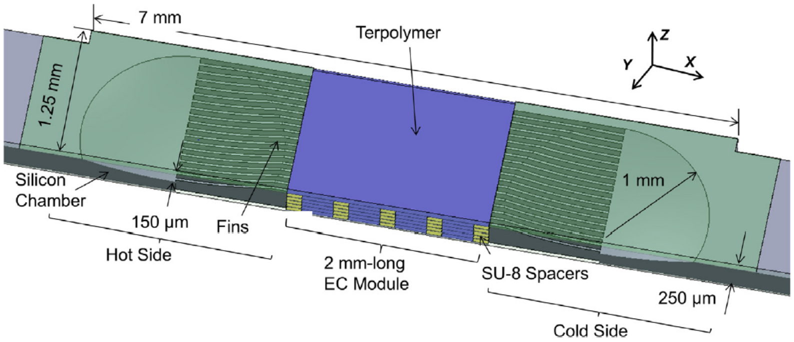

Figure 3.3 **Sketch of a 3D model of an EC cooler |** From Guo et al. [2]. The EC module is 2 mm long and is made of 10 µm-thick terpolymer layers. The fluid flows back and forth through the EC module in the x direction thanks to the actuation of two diaphragms placed at AER end, represented by the 1 mm circles.

was 2 mm long and 1.25 mm wide, containing 5 10 µm-thick plates made of PVDF (spaced 50 µm thanks to SU-8 spacers) and the heat transfer fluid HT-70. The motion of the fluid was carried out thanks to 2 diaphragms placed at the ends of the AER that were actuated electrostatically in an anti-phase fashion. The temperature span of the device was externally imposed by defining the temperature of the cold and hot side so that the corresponding cooling power could be measured. For a given temperature span of 15 K and operating the device at a frequency of 20 Hz, the model reported a cooling power density (space-averaged heat flow on the cold end cross-section of the AER) of 3 W cm^{-2} and a COP / COP_{Carnot} of 31%. The authors mentioned as well that “the time lag between the electric field and the diaphragm motion was found to play an important role”, and that higher applied electric fields should lead the model to higher temperature spans and cooling power densities.

3.3.2 Numerical evaluation of a kilowatt-level rotary electrocaloric refrigeration system

In 2021, a model of a fluid-based rotatory electrocaloric cooler using a finite element software (ANSYS 18) was presented by Shi et al. [3] with the aim to demonstrate a large cooling capacity. The operation of such a system is sketched in Figure 3.4, where rotary in plane movement of a cylinder containing the EC material P(VDF-TrFE-CFE) is coupled with continuous unidirectional out of plane flow of a heat transfer fluid (HT-70) through the EC material and pipes. The simulated cylinder (with an inner diameter of 40 mm, outer diameter of 110 mm, and height of 200 mm) is divided into 12 even parts, and the EC material structured in 0.45 mm plates. The volume of the EC material in each EC unit is 170 cm^3, giving rise to a total EC mass of 3.6 kg. In this model, the EC effect was simulated with positive and negative heat pulses and adiabatic conditions were assumed at the exterior walls to thermally insulate the material from the environment. A cooling power of 290 W was calculated when the device was operated at a temperature span of 10 K and cycle period of 10 s. The COP under these conditions was of 5.5. Moreover, the authors observed that both cooling power and COP increase linearly with the applied electric field if the temperature span is maintained constant. As expected, shorter cycle periods largely increased the total cooling power, and after proper tuning of the operational parameters, a maximum cooling power of 1730 W was reported. This assumes the initial goal of designing EC devices able to operate in the kilo-watt range.

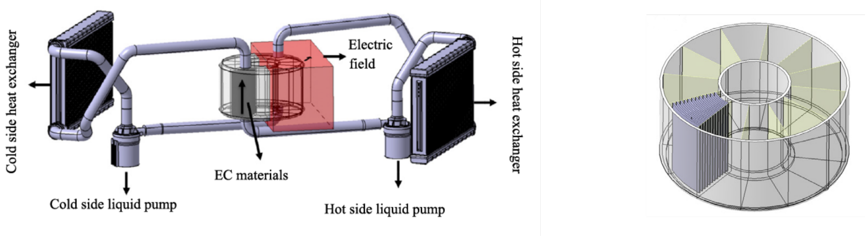

Figure 3.4 **Sketch of the rotatory electrocaloric refrigeration system |** From Shi et al. [3].

3.3.3 Design concept and numerical evaluation of a highly efficient rotary electrocaloric refrigeration device

Shortly after, the same team presented a complementary outcome of their rotatory electrocaloric refrigeration device [114]. This time, the target was compact and efficient devices where size and weight are the main priority. Hence, the rotary EC cylinder had an inner diameter of 4 mm, an outer diameter of 11.1 mm, and a height of 50 mm and was evenly divided into two parts. Each of these parts contained 36 EC sheets (0.1 mm-thick) and the fluid slits were set to 0.1 mm. In this work, the operation of different heat transfer fluids (water, HT-70, and silicone oil) was studied as well. Their results showed that when water is utilized, cooling power and COP are maximized, reporting a maximum cooling power of 9.89 W cm^{-3} and a COP of 10.5 for a temperature span of 10 K. Interestingly, the lowest temperature of the cold-side heat exchanger was calculated when using silicone oil as the heat transfer fluid. This work suggests that, depending on the application needs, a different choice should be made to optimize performance, prioritizing water for higher cooling power demands, and silicone oil for colder temperatures at the cold side.

3.3.4 An electrocaloric refrigerator without external regenerator

A numerical modelling of a rotatory EC prototype was presented in 2015 by Qiming Zhang's team based on finite element simulations. The system consisted of two EC rings (outer

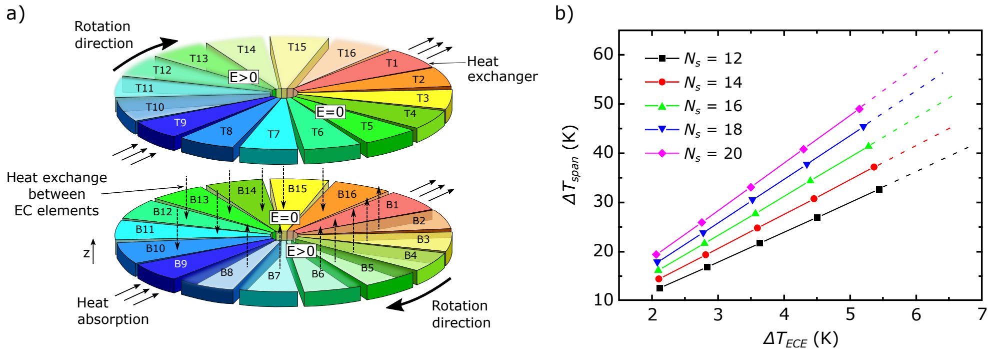

Figure 3.5 **A rotatory EC cooler |** From Gu et al. [4]. a) Sketch of a the modelled rotatory EC cooler. The device consists of 2 rings, each containing 16 EC elements (T1-T16 for ring on the top, and B1-B16 for ring on the bottom) and 4 heat exchangers (at T1 and B1, where heat is rejected, and at T9 B9 here heat is absorbed). The electric field E is applied only to half of each ring in complementary regions, i.e., wherever the field is applied on the top ring, it is not in the bottom ring, and vice versa. b) Temperature span ΔT_{span} predicted by the model as a function of the EC effect ΔT_{EC} for different number of EC elements N_S in each ring.

diameter 20 mm, inner diameter 2 mm) placed one on top of the other with 16 EC elements each as shown in Figure 3.5. The material of the EC elements was poly(vinylidene fluoride-trifluoroethylene-chlorofluoroethylene) (P(VDF-TrFE-CFE)) terpolymer with $k = 0.2$ W m^{-1} K^{-1}, $c_p = 1500$ J Kg^{-1} K^{-1} and $\rho = 1800$ kg m^{-3} that were kept constant with respect to the temperature in the simulations. Note that, contrary to other systems, the device did not utilize any external heat transfer substance to regenerate heat. Instead, 1) the 2 EC rings were rotated coaxially with the same speed but in opposite directions and 2) the electric field was applied only to half of the EC elements in the ring, as shown in the Figure. Note that the regions where the electric field is applied in the top and bottom rings are complementary to each other, so that heat is always transferred between the EC rings. Note that the rotation of the two EC rings is done in a stepwise fashion meaning that the two EC rings rotate by a certain angle (given by the number of EC elements in the ring, N_S) so that EC elements in the top and bottom rings are vertically aligned. After each rotation step, the two rings remain still for some time to allow heat to be transferred. After that, the two rings undergo another rotation step, and so on and so forth. The predicted temperature span is plotted as a function of the EC temperature change in Figure 3.5 showing that a regeneration factor (ΔT_{span} / ΔT_{EC}) of 10 is expected when the EC rings are discretized down to 20 elements. Further simulations reported a cooling power density of 37 W cm^{-3} for a temperature span of 20 K and a COP / COP_{Carnot} of 57%. The authors attempted an experimental version of this device in 2018 utilizing BaTiO$_3$-based multilayer capacitor ceramics as the EC working material [94].Under an electric field of 165 kV cm^{-1} (200 V), these EC samples showed an EC magnitude of 0.9 K, and a maximum T_{span} of 2 K was experimentally measured at a rotation speed of 5 rounds per minute.

3.3.5 Other works

In 2015, Smullin et al. [115] presented a model for a heat-switch-based heat pump utilizing EC multilayer capacitors (MLCs). Given a target temperature span and cooling power as well as the size of the MLCs and heat switches, their model was able to predict the amount of the needed EC mass, heat switch area, and number of samples required to be stacked in series. Aprea and co-authors have carried out several models of EC devices. They are all based on 2D representations of active regenerators. In 2016, a publication was presented studying the impact of utilizing different EC materials on the AER performance [116]. In 2017, a new AER model was presented based on the multicaloric material $PbTiO_3$, which is both electrocaloric (EC) and elastocaloric (eC) [117]. The authors operated the cooler at different fluid-flow rates while keeping the frequency and temperature span constant, showing that the highest COP can be obtained when the $PbTiO_3$ underwent exclusively eC effects. On the other hand, operating the device so that both elastocalorics and electrocaloric effects of PbTiO3 are combined increased the cooling power by around 65% with respect to the single electrocaloric or elastocaloric operation. In 2018, the performances of different caloric materials, including EC materials such as P(VDF-TrFE-CFE)/BST polymer, 0.93PMN-0.07PT thin films, $Pb_{0.97}La_{0.02}(Zr_{0.75}Sn_{0.18}Ti_{0.07})O_3$ or $Pb_{0.8}Ba_{0.2}ZrO_3$, were studied and compared [118, 119]. In 2019, they completed the study by analyzing as well the heat transfer with Al_2O_3-water nanofluids [120]. The authors concluded that with these kinds of fluids the caloric coolers can notably improve their performance. Other analytical and numerical models of EC devices can be consulted elsewhere [121–124].

Chapter 4

Design and characterization of an electrocaloric cooler with $Pb(Sc,Ta)O_3$ multilayer capacitors

This chapter describes the design, construction and characterization of an EC active regenerator based on MLCs of PST. The content of this chapter is based on my first-author publication “Giant temperature span in EC regenerator” [5]. Text in Section 4.3 has been taken from first author contribution to the book chapter “Basics of design and modelling of regenerative electrocaloric coolers” [71]. Among the different tasks conducted in this chapter, the following were not performed by me:

- Preparation and fabrication of PST-MLCs, performed by Sakyo Hirose and Tomoyasu Usui at Murata Manufacturing.
- Synchronization and control of the instrumentation, done by Pierre Lheritier by means of a Python script.
- X-ray diffraction and analysis of the B-site ordering of the PST-MLC samples, carried out by Youri Nouchokgwe.

The structure of this chapter follows that of my publication [5], with supplementary material embedded. Section 4.1 describes and characterizes the EC samples used, which are lead scandium tantalate multilayer capacitors. Section 4.2 details the experimental design and set-up, and reports its preliminary results (REG 1). Section 4.3 explains how numerical modelling based on finite elements can be used as a tool to identify design changes that notably enhance the performance of the regenerator (temperature span). Section 4.4 shows the novel experimental design (REG 2 and REG 3) after following the feedback of the numerical modelling, presenting its main results in terms of temperature span and cooling power. Further modelling predictions are given as well for future works. Section 4.5 summarizes and concludes the chapter.

4.1 $Pb(Sc,Ta)O_3$ multilayer capacitors as active working bodies

The following work was based on lead scandium tantalate $Pb(Sc_{0.5},Ta_{0.5})O_3$ (PST) multilayer capacitors (MLCs), fabricated by Murata Manufacturing. The samples that were initially supplied were 1 mm-thick. After the results obtained with the modelling, we requested thinner samples (0.5 mm-thick) in order to improve the heat exchange of our device. This is explained in more detail in Section 4.3. PST-MLCs are notably interesting for cooling applications because 1) they show large electrocaloric effects (~ 3 K) around room temperature and 2) they do it in a wide temperature range (> 20 K). The first observation is explained thanks to its sharp first order phase transition [75], whereas the second one is related to the high electric field that the multilayer structure allows to be applied [12]. In addition, the MLC structure is convenient and easy to handle, and the amount of active material (~ 50%) is large enough so that one can make use of the heat that is generated (see Section 2.2). Table 4.1 displays some of the properties and dimensions of the two kinds of PST-MLCs that have been used here. MLCs with different initial batch consisted of PST-MLCs that were 1 mm-thick, and were implemented in the first EC device (REG1). After the results obtained with numerical modelling, we ask the supplier to fabricate thinner samples (0.5 mm) to enhance the heat exchange of the device.

Table 4.1 **Properties and dimensions of 1 and 0.5 mm-thick PST-MLCs |** The values for the 1-mm thick PST-MLCs are taken from [12], whereas the 0.5 mm ones were measured at LIST.

Property	0.5 mm thick PST-MLC	1 mm thick PST-MLC
Density ($g\ cm^{-3}$)	8.6	8.8
Active area (mm^2)	48.7	49
Active layer thickness (mm)	0.386	0.379
# active layers	9	19
Active volume (mm^3)	16.9	35.3
Active mass (g)	0.145	0.309
Specific heat ($J\ kg^{-1}\ K^{-1}$)	300	290

4.1.1 PST-MLCs preparation

Solid-state reaction and tape casting methods were used to prepare PST-MLCs. The details of the preparation process can be consulted elsewhere [12]. The MLC thickness and the number of active PST layers were tuned by changing the stacking-sequence of PST-green sheets with and without the printed Pt inner electrodes. MLCs that are 1 mm-thick and 0.5 mm-thick had 19 and 9 active PST layers, respectively. One of the differences in respect to the PST-MLCs in [12] is the B-site ordering, which strongly influences EC performance in PST. The B-site ordering of the PST-MLCs used in this work was approximately 0.7 ~ 0.8, determined with XRD analyses.

4.1.2 PST-MLC characterization

To characterize the EC effect of the PST-MLCs, temperature measurements were performed with a FLIR X6580SC IR camera at different starting temperatures and applied electric fields. Homogeneous emissivity was insured by spraying the PST-MLCs with Black Matt Spray Paint.

Direct observations of ECEs of a single 0.5 mm-thick PST-MLC are displayed in Figure 4.1 as a function of temperature for an electric field $E = 155$ kV cm^{-1} (600 V) in (a), and as a function of the applied voltage and starting temperature $T_s = 30$ °C in (b). The data was gathered at total MLC surface (10.4 mm x 7.2 mm = 75 mm^2), and represents the average value[1]. The maximum ΔT_{EC} in Figure 4.1a is 2.3 K at 38 °C under 600 V. Between 25 and 50 °C, ΔT_{EC} remains stable around 2.25 K. This is optimal for the operation of cooling devices and thus is defined as the electrocaloric temperature window of the cooler. Below 25 °C, the electrocaloric effect starts decreasing, reaching a value of 0.75 K at 10 °C. Around 20 °C and close to the transition temperature at 0 applied field ($T_C = 17$ °C), an asymmetric behaviour in the ΔT_{EC} is found because the magnitude is different when applying the field than when removing it. The reason behind this lies on the influence of the electric field in the entropy-temperature curves, which are shifted towards higher temperatures. More details on this can be consulted elsewhere [75, 125].

Likewise, ΔT_{EC} increases with the applied voltage (Figure 4.1b), reaching a maximum ΔT_{EC} of 2.37 K under 700 V ($E = 184$ kV cm^{-1}). Above 100 V, the trend follows a linear regime because the electric field is high enough to completely bring the sample to its ferroelectric phase. These values agree with what Nair et al. [12] reported in 2019 with better B-site ordered 1 mm-thick PST-MLCs. The authors disclosed EC effects of 2.6 K in

---

[1] The real electrocaloric effect of active PST is ~ 1.5 times the ΔT_{EC} in Figure 4.1 because the active area of the MLC (49 mm^2) is 65% of the total surface.

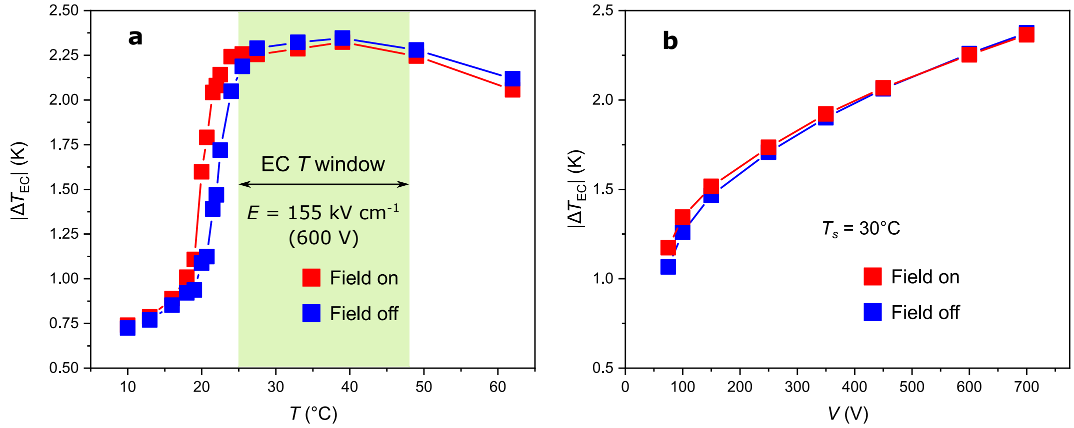

Figure 4.1 **Adiabatic temperature change of 0.5 mm - thick PST-MLCs |** a) as function of the starting temperature for an applied electric field E = 155 kV cm^{-1} and b) as a function of the applied voltage and starting temperature T_s = 30 °C.

the same temperature range and applied electric field E = 155 kV cm^{-1}. Moreover, they showed that these better ordered PST-MLC samples could sustain electric fields as high as 290 kV cm^{-1}, reporting ΔT_{EC} = 5.5 K in the active areas. Unfortunately, the breakdown field in our samples was observed around 700 V (184 kV cm^{-1}). Because of that, the applied voltage was limited to 600 V (155 kV cm^{-1}) in subsequent experiments.

4.2 Design of a fluid-based active electrocaloric regenerator (REG1)

The devices developed in this chapter (REG 1, REG 2 and REG 3) followed the principle of active regeneration (Section 2.4.1). They are all based on PST-MLC samples structured in parallel-plate ensembles. The details of these devices are explained in the following subsections, and in appendix tables A.1, A.3, A.5.

4.2.1 Experimental set-up

The experimental set-up of our first fluid-based active electrocaloric regenerator (REG1) is shown in Figure 4.2. It consisted of: the EC regenerator itself, containing the EC material; a syringe pump (A NE-1010), that displaced the heat transfer fluid with a 10 mL Terumo syringe; a power source (Keithley 2410), that supplied charges (and discharged) the EC material; and type K thermocouples, embedded into the fluid tube to monitor the temperature at both sides of the EC regenerator. Note that thermocouples, syringe pump and power supply were governed by an external computer thanks to a Python script that

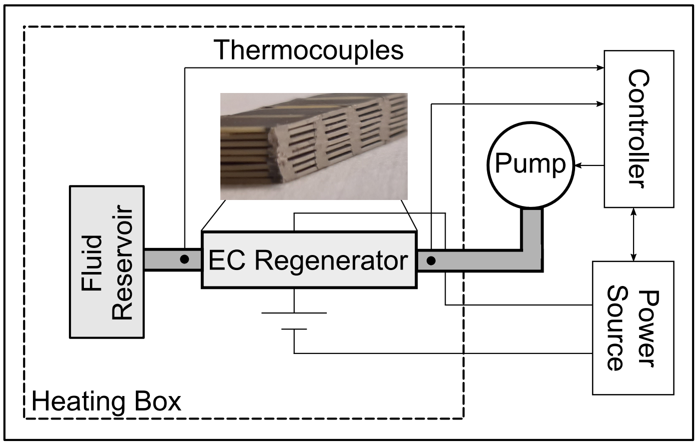

Figure 4.2 **Schematics of the experimental setup of REG1.**

ran the entire operation. Likewise, the fluid system consisted of a non-closed single loop where one end of the regenerator was connected to the syringe pump and the other end was attached to an unsealed fluid reservoir. To reduce friction between fluid and syringe, no fluid was allowed to penetrate inside the syringe. Instead, the compressed and expanded volume inside the syringe was air. Preliminary tests confirmed that there was no difference in the flow rate when loading the syringe with air instead. In addition, the AER was enclosed in a polyurethane box that contained a heater and was used to set the starting temperature of the experiment. The latter was necessary because the optimal working temperature range of the PST-MLCs is right above room temperature (25 °C in our laboratory, Figure 4.1).

The operation of an AER requires thermodynamic cycles such as those described in Figure 2.7. They are typically formed by four steps: A) polarization / charging of the EC capacitors; B) displacement of the heat transfer fluid to one side of the AER; C) discharging of EC samples; and D) displacement of the fluid to the other side of the AER. Due to constraints of the at the time set-up, the fluid was not stopped in steps AB and CD, resembling an Ericsson-Brayton-like cycle like the one described in Section 2.4.3. Approaching a more Brayton-like cycle by stopping the fluid in the polarization and depolarization steps would help improve the temperature span [10]. A summary of the operation of these customized thermodynamic cycles is shown in Figure 4.3. The figure plots the temporal profile of the voltage and current supplied to the PST-MLC stack (red and black curves, respectively), as well as the flowing direction of the heat transfer fluid (green and purple shaded areas). At $t_0 = 0$, the sourcemeter charged the PST-MLCs at the given constant current until the compliance voltage was reached. In the meantime, the fluid was pumped to one side of the regenerator (namely, forward direction). Once the EC material was charged, the current dropped to 0 and the voltage remained constant. At $t = \tau/2$, the flow direction was reversed (backwards) and a negative constant current of the same magnitude as before was set to

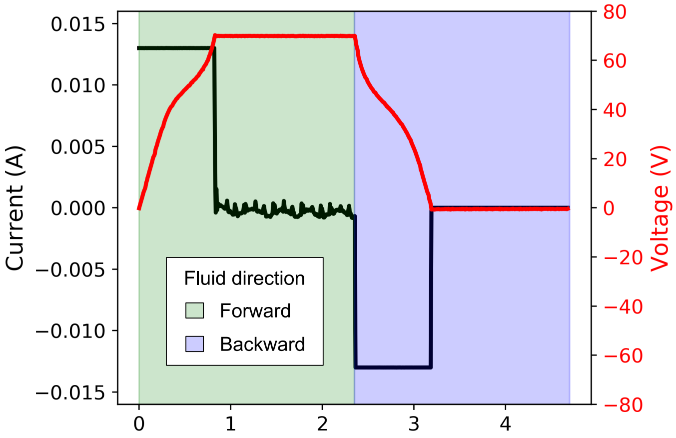

Figure 4.3 **EC regenerator cycle characteristics |** Current (in black) and applied voltage (in red) time evolution of 96 0.5 mm PST-MLCs connected electrically in parallel. The shaded areas represent the fluid flow direction.

discharge the PST-MLCs. Consequently, the voltage decreased until the capacitors were totally discharged. To correct the dielectric loss and communication delays, the time of discharge was self-addressed by our script at each cycle in order to reach 0 V (and not negative values) under a certain tolerance, which was controlled as well. The current was set to 20 mA, the limit of the power supply at high voltages.

4.2.2 REG1 design

The first based active electrocaloric regenerator (REG1) was formed initially by a matrix of 3 columns x 5 rows of 1 mm thick PST-MLCs (Figure 4.4). This design was labelled as REG1. To structure it, nylon frames were 3D printed with 0.5 mm spacers, giving rise to an overall interior regenerator volume (PST-MLCs and fluid) of 1.7 cm^3. Fluid diffusors were added at the EC regenerator ends to ease the fluid pressure drop and gold laminar sheets contacted electrically the samples. Finally, the entire structure was encapsulated in a housing providing sealing from the dielectric fluid (silicone oil of viscosity 5 cSt at 25°C, purchased from Sigma Aldrich), chosen for its electrically insulating nature. While the overall interior volume (PST-MLCs and fluid) was 1.7 cm^3, the resulting total prototype's volume (including frames and EC housing) was 168 cm^3. The fluid used was silicone oil to prevent short-circuits thanks to its dielectric nature. At the applied field of 80 kV cm^{-1}, the temperature span was of 0.6 K, whereas at 155 kV cm^{-1}, 1 K. At this applied electric field, the material showed 2.2 K of adiabatic temperature change (Figure 4.1), which means that the regeneration factor of the REG 1 was 0.45.

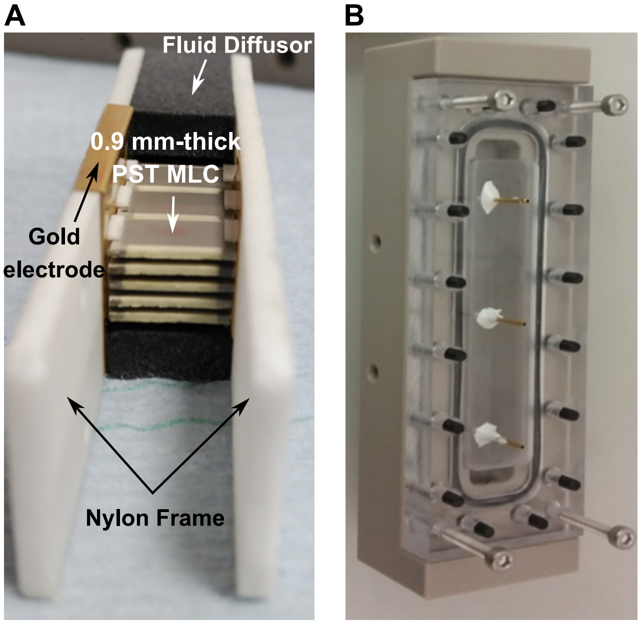

Figure 4.4 **Photos of REG1 in the laboratory |** From Torello et al. [5]. A) Parallel-plate based AER made of PST-MLCs (10.4 x 7.2 x 1 mm^3), structured in a matrix of 3 columns x 5 rows by the white Nylon frame; the fluid slits are 0.5 mm thick. Other structural pieces include fluid diffusors, placed at each AER side to diminish the pressure drop. B) EC housing in which the structure in A) is encapsulated to seal the AER and provide thermal insulation.

4.3 Numerical modelling to enhance the temperature span

To improve the temperature span of REG1, a numerical modelling was explored with two goals: 1) to reproduce the experimental data measured with REG1, and 2) to come up with new prototype configurations with better performances. To see the net effect of these configurations, as many parameters as possible were frozen. Thus, the total amount of cycles (50), the applied voltage (600 V, ΔT_{EC} = 2.2 K) and the fluid flow (25 mL min^{-1}) were maintained constant. The only parameter that was optimized was the frequency. In the experiment, parameters such as the fluid flow and the frequency were adjusted in situ for each new configuration.

4.3.1 Matching the experimental performance

COMSOL Multiphysics 5.2a software was used, coupling the heat transfer and fluid dynamic modules. The geometry simulated (Figure 4.5) consisted of a 2D representation of REG1's cross section, including structural and surrounding elements such as PST-MLCs, fluid diffusors and nylon frames (dimensions in Table A.1 and A.2, material properties in Table 4.2). Adiabatic conditions were imposed at the exterior walls as a first approximation and a no-slip boundary at the fluid-solid wall to ensure laminar flow, according to Reynold's number $Re = 0.87$. The temperature was acquired by averaging at each time step the temperature of the Pt circles, which were placed to simulate the 1.6 mm thick Pt100 RTD sensors used in the experiment.

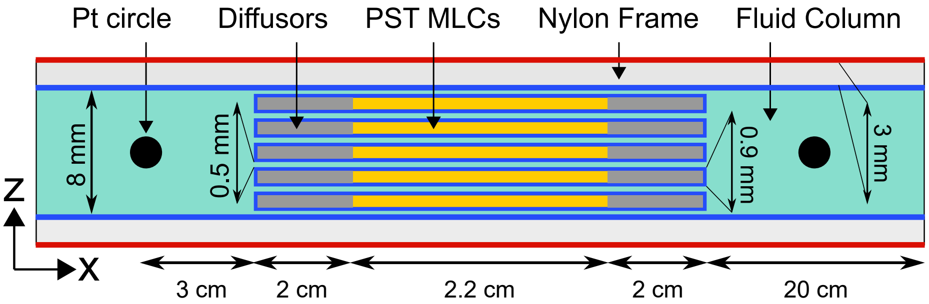

Figure 4.5 **REG1 model |** 2D representation of REG1. It includes the Pt100 temperature sensors (Pt circle), fluid diffusors, PST MLCs, Nylon frames and fluid column.

Table 4.2 **Material thermal properties in REG1 model.**

Material	C_p (J kg^{-1} K^{-1})	k (W m^{-1} K^{-1})	ρ (kg m^{-3}	μ (Pa s)
PST-MLC	300	2.1	8100	-
Silicone Oil	1634	0.16	913	5
Platinum	120	70	19000	-
Nylon	1500	0.26	2000	1
Water	4180	0.6	1000	1

For our model to be predictive, it needs first to show that it can reproduce the available experimental data of REG 1. This is shown in Figure 4.6, where the temperature span of REG 1 is plotted as a function of the electric field, and as a function of time (inset) for an applied electric field of 80 kV cm^{-1}. The squares correspond to experimental data, whereas the crosses correspond to the model. In Figure 4.7, this is shown by the square and cross labelled "Mod-Exp. Match", in which a temperature span of 1 K was measured with a cycle period of 12 s. To fit the experimental data, the power heat density simulating the EC effect (Section 2.5.2) was decreased by 20 % in respect to the real value. Also, the position of the platinum circles emulating Pt100 temperature sensors was adjusted until the time-dependent profile data matched.

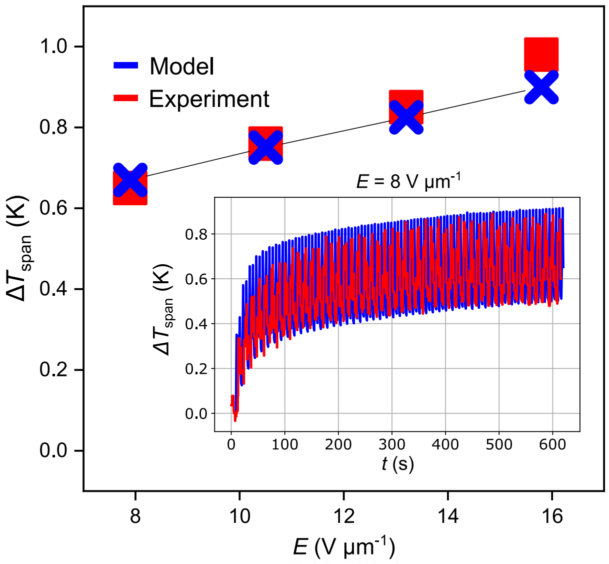

Figure 4.6 **REG1 data |** Comparison between numerical modelling and the corresponding experimental performance of REG 1.

4.3.2 Achieving higher temperature spans

4.3.2.1 Influence of inactive mass on T_{span}

Fluid-based EC devices typically require cases and housings that provide fluid sealing and thermal insulation [5, 7, 8, 65]. These pieces are usually 3D-printed with common thermal insulators, such as nylon or polyether-ether-ketone (PEEK), with thermal conductivities $k \sim 0.2$ W m^{-1} K^{-1}. However, EC materials are poor thermal conductors as well, with thermal conductivities $k \sim 1$ W m^{-1} K^{-1} for ceramics, and $k \sim 0.1$ W m^{-1} K^{-1} for ferroelectric polymers. The dielectric heat transfer fluids have also low thermal conductivities, $k \sim 0.1$ W m^{-1} K^{-1}. With these conditions, it is reasonable to foresee that the surrounding structural elements may not act as thermal insulators in our experiments and might instead be absorbing a non-negligible amount of heat coming from the EC material and the heat transfer fluid. This contribution is shown in Figure 4.7 (where the temperature span of the device is plotted as a function of the cycle period τ) by the square labelled “Less inactive mass”. In the new configuration tested in the model, all the surrounding elements initially considered to model REG 1 (nylon frame and fluid diffusors) were removed so that the fluid column and the EC material were the only geometrical domains considered. The model predicted a temperature span of 2 K, twice as large as before (1 K) for the same cycle duration of 12 s.

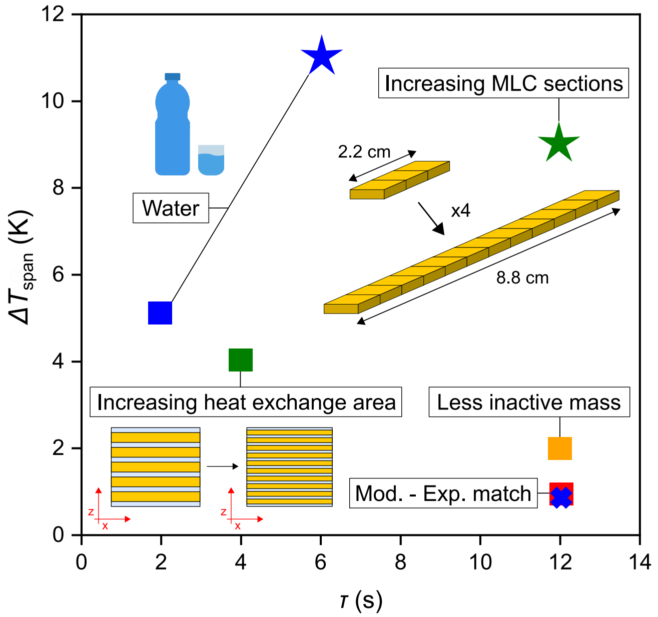

Figure 4.7 **Temperature span prediction from the model of new prototype's configurations |** These include modifications in REG1 design, such as enlarging the length, removing the inactive mass, or using a different heat transfer fluid.

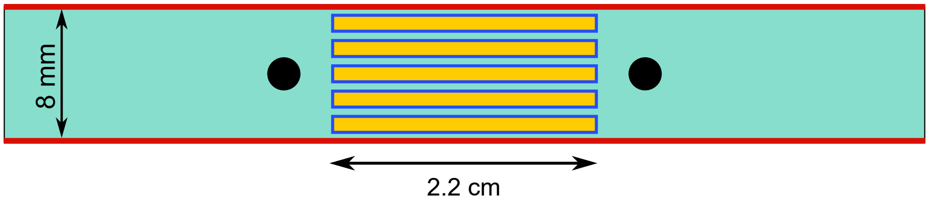

Figure 4.8 **"Less inactive mass" model |** 2D representation of the "less inactive mass" configuration in Figure 4.7.

4.3.2.2 Influence of EC material thickness on T_{span}

Another important parameter to play with is the thickness of the EC plates in AER. Thinning the plates increases the heat exchange interface between the EC material and the fluid, and hence, heat is transferred from the EC material to the fluid (and vice versa) at a higher heat transfer rate. Enhancing the heat transfer between the active element (EC material) and the regenerating substance (heat transfer fluid) in an AER permits increasing the cycle frequency, and, hence, reducing the contribution of parasitic losses, enhancing the overall device performance. In Figure 4.7, this is shown by the square labelled "increasing heat exchange area". To do that, the thickness of the EC plates (PST-MLCs) was reduced from 1 mm to 0.5 mm, and as a result, the temperature span increased from 2 K to 4 K. In addition, the cycle period was reduced from 12 s to 4 s. It is important to note that the fluid channel slit had to be reduced accordingly (from 0.5 mm to 0.25 mm) to keep the volume ratio of fluid and EC material constant. Not doing so would have meant reducing the active mass of our device, and hence, reducing the effective adiabatic temperature change. Also, note that from the results obtained, one could conclude that the smaller the plate thickness, the better the performance. However, frictional heating effects induced by the fluid viscosity were not accounted for in the model, and hence, having a too small plate thickness (and thus, too small fluid channels) could become an issue. Another important feature is the feasibility of experimentally implementing EC plates that are thinner than 0.5 mm, which is not trivial considering the limited material mechanical strength and fluid slit homogeneity. Thus, a compromise will need to be made when reducing the sample thickness for a better heat exchange.

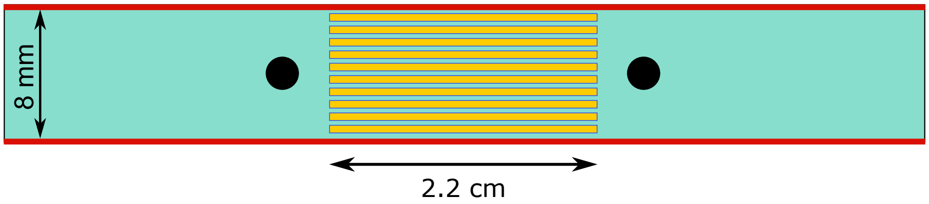

Figure 4.9 **"Increasing heat exchange area" model |** 2D representation of the "increasing heat exchange area" configuration in Figure 4.7.

4.3.2.3 Influence of prototype length on T_{span}

The length of an AER is another interesting parameter to be considered. In an AER, a temperature gradient is built in the EC material along the fluid displacement direction. For a given temperature span, the amplitude of this temperature gradient is more pronounced with a shorter AER length. Hence, a larger amount of heat needs to be pumped from the cold side to the hot side by the device in order to sustain it. It is clear then that larger temperature spans are a priori expected by AERs with longer lengths. This is shown by the star in Figure 4.7 labelled "increasing MLC sections" . By increasing the AER length fourfold, the temperature span increased from 4 K to 9 K. Because of the longer AER length (same cross-section but more EC mass), more heat is generated and more fluid needs to be displaced. Thus, since the fluid volume flow rate was kept constant, the optimum cycle period was found to be at 12 s, three times larger than the previous step. Note that, when increasing the length of the AER, it increases as well the area of the external walls and, hence, it also increases the contribution of the heat losses to the surroundings. A balance needs to be found.

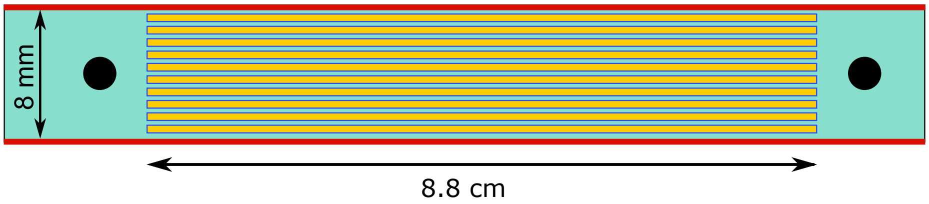

Figure 4.10 **"Increasing MLC sections" model |** 2D representation of the "increasing MLC sections" configuration in Figure 4.7.

4.3.2.4 Influence of fluid choice on T_{span}

Finally, the performance of a different heat transfer fluid was studied. Note that all data points gathered up to now were calculated employing silicone oil because of its dielectric nature. However, from a thermal point of view, silicone oil is not a very good heat transfer fluid (see Table 4.2). This is not the case with water, which is often considered to be one of the best heat transfer fluids thanks to its large specific heat and thermal conductivity (but also because of its non-toxicity and abundance). Thus, in Figure 4.7, the configurations "increasing heat transfer area" and "increasing MLC section" were calculated again replacing silicone oil by water (square and star labelled "water"). The results showed that the use of water increases the temperature span by about 25 % (from 4 K to 5 K and from 9 to 11 K) while having the cycle period τ halved (from 4 s to 2 s and from 12 s to 6 s). These results are compatible with other works on MC and EC where the influence of the heat transfer fluid was studied as well [7, 126].

4.4 EC regenerator improved versions: REG2 and REG3

From the modelling described in Section 4.3, a second AER was built (REG 2), with thinner PST-MLC samples (0.5 mm-thick). Attempting to reduce the inactive mass of the system, all structural pieces, such as nylon frames, fluid diffusors and EC housing, were removed. The gold sheet electrode, too. Instead, mechanical assembly of the parallel plate matrix was achieved by placing double-sided tape stripes at the MLC sides, as Figure 4.11 displays, giving rise to a total porosity of 36%.

The width of these stripes was minimized to increase the amount of MLC surface that was in contact with the fluid, which was calculated to be around 60-70% of the MLC width. On the top plates, a conductive wire of diameter 0.12 mm and longer than the MLC regenerator length was placed on the double-sided tape strip to drive electricity from the power supply. The thickness of the double-sided tape strip in contact with the wire was 0.125 mm to ensure that all slits had the same height so that the fluid flow was homogeneously distributed. The MLC electrode terminals of each side were connected in parallel by silver paste bridges

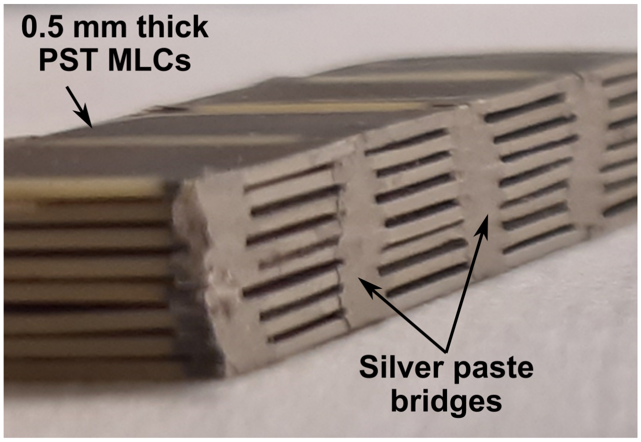

Figure 4.11 **REG2's PST-MLC stack |** Optical photograph of the 0.5 mm-thick PST-MLC stack, structured with double-sided tape spacers and connected electrically with silver paste bridges.

that were drawn in between. More silver paste bridges were built in between the electrodes terminal of the top plate and the conductive wire. Capacitance measurements of the entire system by a voltmeter were done to confirm that all MLCs were connected in parallel - and to the wires - at the end of the process before the experiment started. The AER length was increased as well by building a parallel-plate (PP) matrix of 8 rows x 16 columns (total number of PST-MLCs hence was 128). The dimensions of the regenerator were 115 mm (L) by 10.4 mm (W) by 6.25 mm (T). The total PST mass was 38.4 g, of which only 60% was active due to the overlap of the inner MLC electrode sheets (as with the 1 mm thick PST-MLCs). The heat transfer fluid remained the same (silicone oil). The overall interior volume of REG2 was 7.5 cm^3.

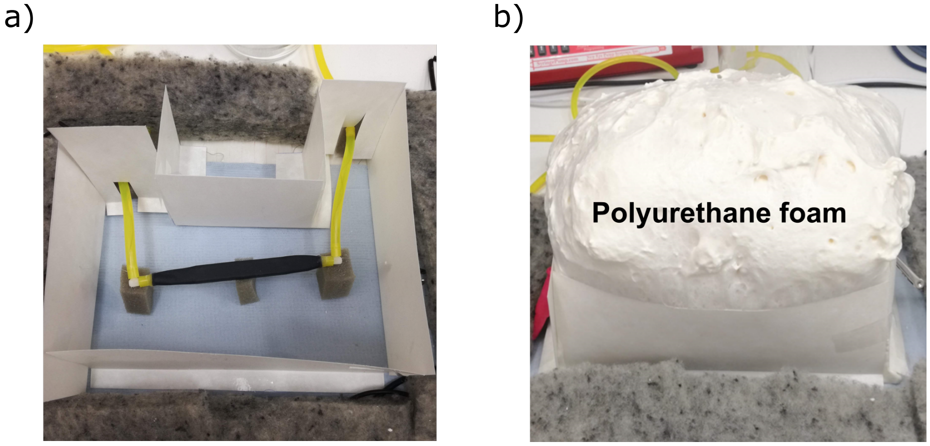

Figure 4.12 **REG2's experimental design |** a) with the polyolefin hose (black), connected to the fluid tubes (yellow) before insulation, b) after applying the polyurethane foam.

To seal the resulting prototype, a black polyolefin hose was used (Figure 4.12a). This is a very interesting solution because 1) it adapts its shape to the PST-MLC stack matrix so that dead volume is minimized, and 2) it has a negligible thermal mass. To improve the thermal insulation, polyurethane foam was applied on top of the polyolefin hose (Figure 4.12b). After curing, the polyurethane foam had a wall of 15 cm. The MLC stack (overall interior volume) was 7.5 cm^3. Another remarkable feature of this new design is the possibility to use an IR-camera to visualize (if thermal insulation is not provided) the entire temperature profile of the prototype under operation. This is shown by Figure 4.13, with the infrared imaging of REG2 (top) and the corresponding reading of temperature (bottom) along the depicted black horizontal line. This kind of characterization is useful because it allows one to spot where the temperature gradient peaks are, and, thus, deduce the maximum temperature difference in the regenerator. Nevertheless, thermal insulation needs to be provided when aiming at the maximum temperature span, and consequently, IR-imaging is no longer possible in these conditions.

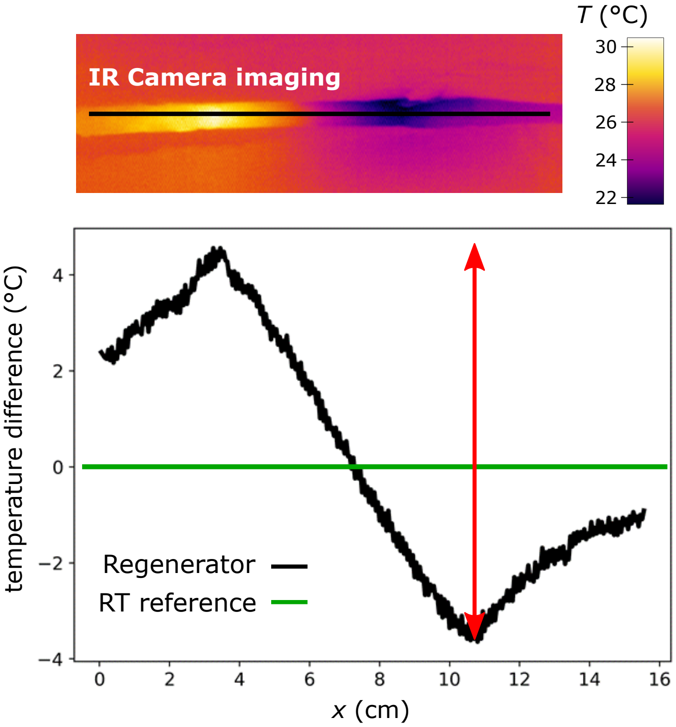

Figure 4.13 **Steady state IR camera imaging of REG2 |** Prior to the appliance of the polyurethane foam. The experimental parameters for this particular case were V = 150 V, flow rate of 25 mL min^{-1} and cycle period τ = 8 s.

4.4.1 Temperature span

The performance of the regenerator was optimized first by playing with the flow rate and cycle period. Within these experiments, the applied voltage was kept to 50 V (E = 13 kV cm^{-1}) to avoid any kind of fatigue and sample breakdown. Although drastic changes were not observed, the parameters that showed the highest temperature span corresponded to a fluid flow rate of 25 mL min^{-1} and a cycle frequency of 0.125 Hz, which is in agreement with similar works [7, 8]. This corresponds to a ratio of fluid displaced with respect to the total volume of the fluid in the regenerator v^* of 0.62. The same set of parameters was used later to operate the EC device close to their breakdown field (600 V, E = 155 kV cm^{-1}) to maximize its performance. The starting temperature was set to 30 °C to take full advantage of the PST-MLC temperature window, as shown in Figure 4.1. Figure 4.14 shows the resulting temperatures of hot (red) and cold (blue) ends of REG2. Data was gathered with type-K thermocouples, embedded in the fluid tubing as Figure 4.12 depicts. The corresponding temperature span (difference between cold and hot sides) is displayed in the inset of the figure as a function of time (in black).

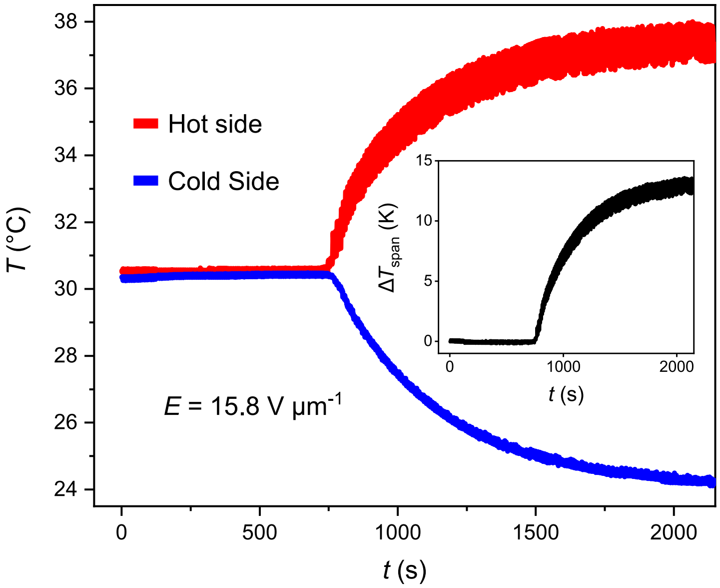

Figure 4.14 **Performance of REG2 |** Time evolution temperature and temperature difference (inset) of the REG2's hot and cold side for an E = 155 kV cm^{-1} and T_s = 30 °C.

The system was let to reach thermal equilibrium for several minutes before launching the field to get rid of any other kind of thermal contributions, as confirmed for the first 750 s (Figure 4.14). After 1500 s of operation, a maximum temperature span of 13.0 K was measured. This is 13 times larger than REG 1 and means a regeneration factor of 5.9 (ΔT_{EC} is 2.2 K under this applied field). The temperature span achieved is also higher than similar EC devices, including a temperature span of 6.6 K by Gu et al. [4] (Figure 4.15). Note as well that the result obtained agrees well with the modelling in Section 4.3, where a temperature span ~ 10 K was predicted after reducing the amount of inactive

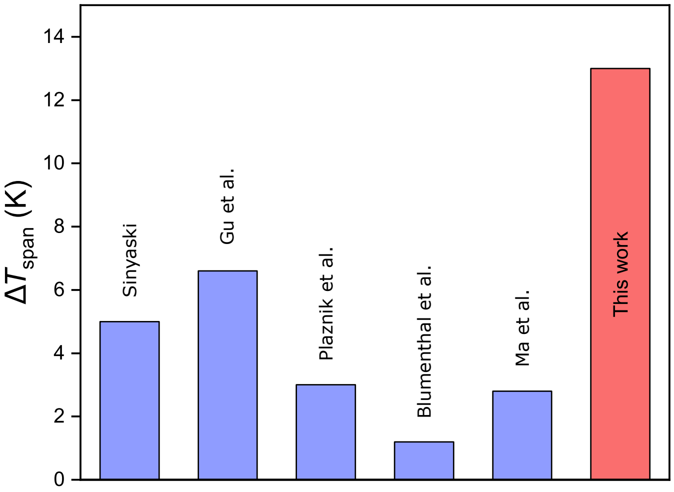

Figure 4.15 **Temperature span achieved by recent EC devices |** This includes prototypes from [4, 6–9], all of them previous to the work reported here.

mass, decreasing the thickness of the PST-MLCs to 0.5 mm and enlarging the length of the regenerator by at least a factor of four.

4.4.2 Cooling power

To report cooling power values, a third regenerator (REG 3) was built. This device followed the same design as REG2, but the parallel plate matrix was formed by 32 1 mm-thick PST-MLCs, with 8 columns x 4 rows and fluid spacers of 0.5 mm. After connecting all the PST-MLCs and sealing the structure as in REG2, a 20 cm - long coiled nichrome wire 0.25 mm thick was placed at the cold side to act as a heat source. The wire endings were left outside the sealing tube and were connected to a second power supply through copper wires. The measured resistance of the nichrome wire was 8.9 Ohms, whereas of the copper wires 0.1 Ohms. The cooling power was directly deduced from the electric power circulating through the nichrome wire [37]. The experimental results obtained for REG3 are displayed by the red squares in Figure 4.16a, reporting a maximum temperature span (no-load conditions) of 3 K and a maximum cooling power (i,e, $\Delta T_{span} = 0$) of 12 W kg^{-1} of active electrocaloric material.

To fit the experimental data, a numerical modelling was built with COMSOL Multiphysics with a 2D representation of the regenerator's cross section, similarly than the previous model. To fit the experimental data, the power heat density that simulates the EC effect was decreased by 40% with respect to the real value and the effective nichrome wire length was increased to 36 cm. The corresponding modelling results are shown by the pink triangles in the Figure 4.16a, which are in agreement with REG1 data. The model agreed well

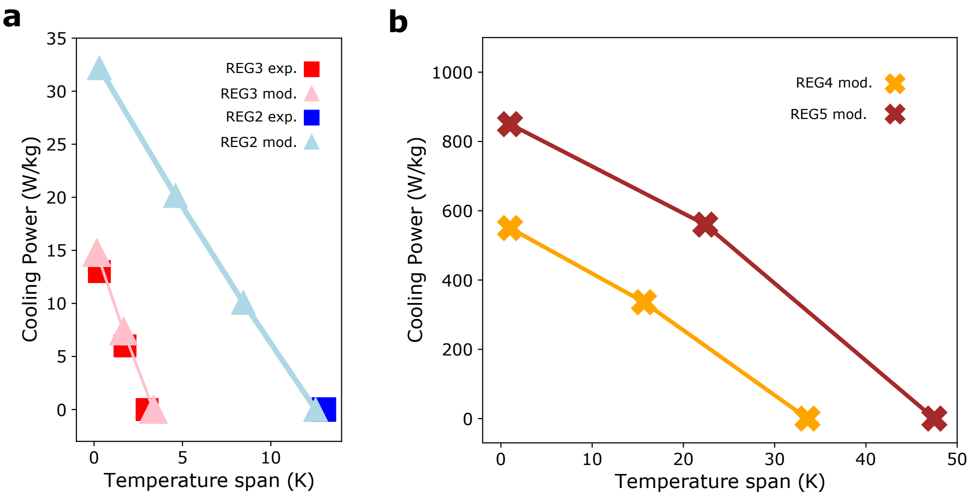

Figure 4.16 **Cooling power vs temperature span curves |** a) Experimental and simulated data of REG2 (red squares and pink triangles) and REG 3 (blue square and light blue triangles); b) simulated data for REG4 (orange crosses) and REG5 (brown crosses). The cooling power axis is normalized per kilograms of active material.

with REG2 performance too, displaying a no-load temperature span of 12.8 K (light blue triangles), very close to the 13 K in the experiment (blue square). The maximum cooling power that the model predicted for REG2 was 32 W kg^{-1} (of active EC material).

Additional configurations were tested with this same model, where heat exchangers were added in the hot side to stabilize its temperature. These configurations consisted of PST-MLCs that were 100% electrocaloric active and displayed adiabatic temperature changes of 5.5 K, which has been shown possible when applying a supercritical field of $E = 290$ kV cm^{-1} in better ordered samples [12]. In addition, the heat transfer fluid was assumed to be water thanks to its greater thermal properties. Regarding the PST-MLC thickness, two values were tested for better heat exchange: 0.3 and 0.2 mm. Hence, labelled these hypothetical prototypes were labelled as REG4 and REG5, respectively. Their experimental parameters can be consulted in Tables A.7 and A.8. The results obtained are gathered in Figure 4.16b. It shows that for REG5, the model predicted a maximum temperature span as large as 50 K and a maximum cooling power of almost 1000 W kg^{-1} (of active material). These results are comparable to the best elastocaloric prototypes, displaying temperature spans of 28 K [44] and cooling powers of 800 W kg^{-1} [22], and magnetocaloric prototypes, displaying temperature spans 40 – 60 K [127–129] and cooling powers of 2000 W kg^{-1} [37].

4.5 Summary and conclusions

This chapter describes the design, development and characterization of three fluid-based electrocaloric active regenerators (REG1, REG2 and REG3) based on multilayer capacitors made of $Pb(Sc_{0.5},Ta_{0.5})O_3$ (PST-MLCs). Numerical models based on finite-element software are described and presented as well. These models were built with two purposes: 1) to reproduce the existing experimental data and 2) to predict further performances with improved designs. This is for instance the case in the evolution from REG1 to REG2. REG1, built prior to any numerical modelling, displayed a maximum temperature span of 1 K. REG2, built after the outcome of our numerical model, reported 13 K of temperature span. This is a 13-fold increase. The changes the model suggested for the design of REG2 were: 1) thinner PST-MLC samples, 2) longer regenerator's length and 3) suppression of any kind of inactive mass other than the dielectric fluid. REG3, built to disclose cooling power values, reported 12 W kg^{-1} (of electrocaloric active material) at 0-K temperature span. An upgraded numerical model based on this experimental data predicted temperature spans of 50 K and cooling powers in the order of 1000 W kg^{-1} when using even thinner (0.2 mm) PST-MLCs, water as a heat transfer fluid and applying supercritical electric fields of 290 kV cm^{-1}, which is possible in better B-site ordered samples [12].

The presented work signifies an important achievement not only in the scientific community but also in the industrial sector. It shows that, similarly as magnetocaloric and elastocaloric coolers did before, cooling devices based on the EC effects can display temperature spans larger than 10 K. In addition, the prediction of large cooling powers and the enhancement of its intrinsic efficiency by energy recovery means [50] should reinforce and promote the development of even more competitive coolers in the years to come. Experimental validation of such actuators would position electrocaloric cooling as a reasonable and real alternative to the currently dominating vapour-compression systems, with the added value of being more efficient and free of green-house emissions.

Chapter 5

Heat transfer law in caloric regenerators

This chapter focuses on the heat transfer coefficient of caloric regenerative heat pumps and its influence on the performance of these coolers. This study started aiming to answer the questions: 1) what is the heat transfer coefficient of our EC device (described in Chapter 4)?; and 2) what information does this coefficient give us in relation to the device's performance? The first question is actually already answered in the literature, with expressions for the Nusselt number Nu for porous-like assemblies like parallel-plates [130] and spherical particles [131], typical structures of caloric regenerators. In addition, an effective heat transfer coefficient for such kind of devices has been defined as well [132, 133] to account for the solid thermal resistance of the caloric material, which is non-negligible in such devices. Hence, by merging these expressions, one comes up with an effective heat transfer coefficient for parallel-plate and spherical-based caloric regenerators that depends exclusively on the thermal properties of the fluid and caloric material, and on geometrical properties of the porous-like assembly. To answer the second question, all caloric regenerators in the literature that could fit into these expressions were analysed, and their corresponding effective heat transfer coefficient was computed. In this work, this parameter is compared thus with the performance of these coolers to find out whether a correlation or trend can be extracted.

The text of this chapter is the same as my first-author publication "Heat exchange law in caloric regenerators" [69]. Section 5.1 corresponds to the introduction, and has been shortened to avoid unnecessary repetition. Section 5.2 describes the theoretical expressions from literature that have been used in this work to come up with an effective heat transfer coefficient for parallel-plate and spheres fluid-based caloric regenerators. Section 5.3 explains the methodology, including what kinds of caloric prototypes have been included in this study, how the data of these prototypes has been collected and clarifications on the estimation of the adiabatic temperature change and fluid velocities. In Section 5.4, the regeneration factor of the caloric prototypes considered is plotted as a function of the effective heat transfer coefficient (deduced from the expressions in Section 5.2), and the results are discussed. Finally, the chapter ends with Section 5.5 with a summary and conclusions.

5.1 Background

The heat transfer coefficient in caloric prototypes has been reported before. Sinyavsky [61] claimed that a value between 5.000 – 10.000 W m^{-2} K^{-1} was required (although information on the calculation was not disclosed) to further increase the temperature span of their previous EC prototype, which was of 5 K from an adiabatic temperature change of the EC material of 1.5 K. Šarlah et al. [134] used single blow methods to experimentally deduce the heat transfer coefficient of magnetic passive regenerators. Lei et al. [135] compared the performance of four different geometries in a MC gadolinium-based prototype by means of a 1-D model. To do so, the heat transfer coefficient was determined from theoretical expressions involving the Nusselt number Nu and other dimensionless numbers. Faye et al. [93] studied the heat transfer of EC multi-layer capacitors to the surroundings. In the study, different configurations were tested, displaying experimentally measured heat transfer coefficients of 3.400 W m^{-2} K^{-1} in the case of large area thermal pad contacts. Despite these few studies, the direct influence of the heat transfer coefficient on the performance of caloric prototypes has not been explicitly addressed and quantified to date.

5.2 Theoretical expressions

The heat transfer coefficient is commonly expressed as a function of the Nusselt number Nu, the thermal conductivity of the fluid k_f and the characteristic length of the thermal system D_L:

$$h = \frac{Nu k_f}{D_L} \tag{5.1}$$

5.2.1 Parallel-Plates

For the parallel-plate (PP) regenerator configuration, Nickolay and Martin [130] proposed the following expression for Nu:

$$Nu = \left(7.541^n + \left(1.84Gz^{1/3}\right)^n\right)^{1/n} \tag{5.2}$$

where $n = 3.592$ and $Gz < 105$. Gz is the Graetz number, expressed as:

$$Gz = \frac{2v_s A_c \rho_f c_f D_L}{k_f W_p L} \tag{5.3}$$

where v_s is the superficial velocity of the fluid (which is the fluid volumetric flow rate divided by the fluid cross-section area), A_c the cross-section area of the regenerator, ρ_f, c_f, k_f respectively the density, specific heat and thermal conductivity of the fluid, W_p and L the width and length of the plates and D$_L$ the characteristic length, which is $D_L = 2H_s$, H_s being the fluid slit.

5.2.2 Spherical particles

In the case of spherical particles, Engelbrecht [131] suggested the following expression for Nu, valid for laminar flow regimes ($Re < 2100$):

$$Nu = 2 + 1.1 Pr^{1/3} Re_p^{0.6} \tag{5.4}$$

where Pr and Re_p are the Prandtl and Reynolds numbers based on particle diameter, defined respectively as

$$Re_p = \frac{\rho_f v_s D_L}{\mu_f} \tag{5.5}$$

$$Pr = \frac{c_{p,f} \mu_f}{k_f} \tag{5.6}$$

where the characteristic length is $D_L = D_{sp}$, the diameter of the sphere, and f the dynamic viscosity of the fluid (equations (5.1−5.6)) can be consulted as well in Lei et al. [135]). On the other hand, when the solid's thermal resistance is in the same range as that of the fluid, an effective heat transfer coefficient h_{eff} can be defined. This concept was proposed first by Jeffreson [132] and applied modified later by Engelbrecht et al. [133] to the case of caloric regenerators as:

$$h_{eff} = \frac{h}{1 + \frac{Bi}{a_0}} \tag{5.7}$$

where Bi is the Biot number and a_0 a geometrical factor that yields 3 for spheres, 4 for cylinders and 5 for parallel plates. The characteristic length used to calculate the Biot number has been the plate thickness for the parallel-plate and the sphere diameter for the sphere-based prototypes. By plugging Eq. (5.1) respectively for the parallel-plates and spherical beds in Eq. (5.7), an expression for h_{eff} that contains information on the caloric material, heat transfer fluid, porous assembly and geometrical dimensions of the regenerator is obtained.

5.3 Methods

5.3.1 Works included in this study

A statistical study is performed after analyzing all the caloric prototypes that could fit in this study (Table 1), including MC parallel-plate and spherical particles based prototypes, EC parallel-plate fluid-based, one EC parallel-plate solid-based prototype and one eC prototype. The parameter chosen to characterize the performance of these devices was the regeneration factor (RF), i.e. the ratio between the temperature span and the adiabatic temperature change, because it shows how much the device can amplify the latter, regardless of how large this is. Hence, only prototypes with regenerative cycles were considered.

5.3.2 Data points considerations

The data points were taken at no-load conditions, i.e., cooling power = 0, because it is when the temperature span is maximum. The adiabatic temperature change taken to calculate the regeneration factor consisted of an average over the temperatures contained in the regenerator gradient. Only in works [6, 64, 99] the adiabatic temperature change was assumed to be the maximum (at the Curie temperature) because no information about its temperature dependence was given nor could be estimated. Likewise, only the data points that optimized the temperature span (and hence the regeneration factor) in terms of fluid flow and cycle frequency were considered for each work.

5.3.3 MC prototypes considerations

Both reciprocating and rotary prototypes were included. Prototypes with non-spherical particles were not considered, even though an effective spherical diameter is given in most of the cases. The reason for that is that non-spherical particles account always for larger surface areas, so that their heat transfer coefficient is hence underestimated when using expression 5.4.

5.3.4 Estimation of adiabatic temperature change

Almost all MC works are based on Gd. In most of them, the adiabatic temperature change of Gd is not given, but the applied magnetic field is. When that is the case, the adiabatic temperature change was extrapolated from the data in [136, 137], where it is given for pure Gd as a function of temperature for different applied magnetic fields. In the cases for which the adiabatic temperature change of Gd was given, the data was consistent with our extrapolation. In [138, 139], where La(Fe,Co,Si)13, and (La,Ca,Sr)MnO_3 were also used as MC materials, the adiabatic temperature change as a function of temperature was given for the corresponding field applied, so that no extrapolation had to be done.

Layered prototypes were treated the same than non-layered. The only difference has been on the adiabatic temperature change. We took the maximum because the temperature difference between the Curie temperature of the first and last layers exceeded the temperature span of the regenerator.

5.3.5 Fluid velocity considerations

Similarly, the fluid velocity is not directly given in all cases. In those works, the fluid velocity was calculated using other parameters, such as the flow rate, utilization factor, frequency, porosity and volume of fluid in the regenerator. In the cases where this calculation was not possible, it was estimated to be of the same order as similar cases for the parallel-plate geometry, in which the h_{eff} does not vary significantly for fluid velocities in the range of $0.001 - 0.1$ m s^{-1}. For the spherical particle geometry, only the works where the fluid velocity could be calculated were included in the study.

5.4 Results and discussion

The values of h_{eff} and the corresponding RF for the MC, EC and eC prototypes studied are plotted in Figure 5.1. Regression statistical analysis suggests a linear trend that follows the equation $Y = 6 \times 10^{-4} X$. Despite the linear trend obtained, there are factors that can induce dispersion into the data set and hence need to be considered. The first one refers to the heat losses, which are very specific to each design and difficult to quantify. Yet, the impact into the overall regenerative performance is not negligible, because poor insulation can be very detrimental when achieving competitive temperature spans, as shown recently by Torello et al. [5]. The second one refers to the temperature window of the caloric effect, i.e. the temperature range where the caloric effect is strongest seen.

An example of that is found in [139], where a layered $\mathrm{LaFe}_{13-x-y}\mathrm{Co}_x\mathrm{Si}_y$ based regenerator with a temperature window of 35 K (#26 in Figure 5.1) is compared to a non-layered gadolinium one (80% of the maximum adiabatic temperature change is enclosed in a temperature window of 10 K, #25 in Figure 5.1). The heat transfer coefficient of the former is 9000, whereas 17000 for the latter. Yet, the RF is almost 10 for both. Finally, the porosity of the regenerator, defined as the volume fraction of the fluid that lies inside, can have an important impact as well. Very low values of porosity report high heat transfer coefficients because of the thin fluid channels. However, the heat regeneration process requires not

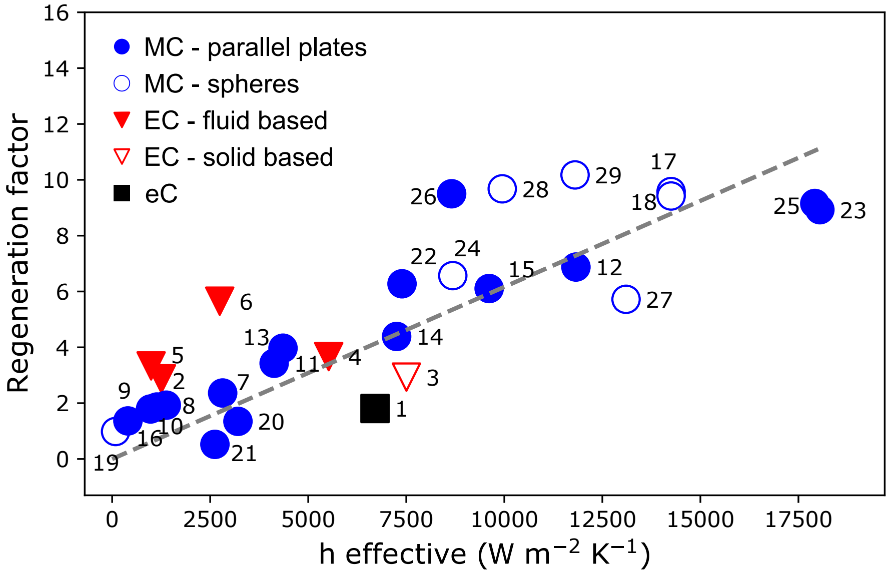

Figure 5.1 **Experimental regeneration factor (RF) of caloric regenerative prototypes as a function of heat exchange coefficient h_{eff} |** The latter is calculated using the expressions described in the methods, and the corresponding linear trend ($Y = 6 \times 10^{-4} X$) from statistical regression analysis. Each point corresponds to the optimum of each prototype.

only a fast heat exchange between the solid and the heat transfer fluid, but also to store a significant quantity of heat in the fluid, which is not the case when the porosity is too low. This has been confirmed in our study, where works in [140, 141], with porosities of 13% and 9% respectively, were found out of the trend because their RF (4 and 1) were achieved with h_{eff} of 14.400 and 22.000. Hence, they were not included in Figure 5.1.

Within this context, Figure 5.2 displays the porosities of the works in Figure 5.1 as a function of V^*, defined as the ratio between the amount of fluid moved per cycle and the total amount of fluid the regenerator can store [7]. All the porosities in Figure 5.2 are framed between 18 and 66 % and V^* between 0.1 and 1.1. Moreover, a trend is visible in these ranges, suggesting an inversely proportional relationship: the larger the porosity, the lower V^*, and vice versa. This should be used as a guide to estimating V^* before running experiments.

For completeness, Table 5.2 shows the expected RF for a given heat transfer coefficient according to the fit in Figure 5.1. It reveals that h_{eff} around 10.000 W m^{-2} K^{-1} are needed to obtain RF of 6. This agrees with [61], where h_{eff} of 5.000 – 10.000 were predicted for such prototype's performances. This law can therefore be used as a help to design more efficiently caloric regenerators by envisioning the performance of new coolers before their experimental development is done. This can be very useful especially when the deduced

Table 5.1 **Details and features of the prototypes in Figure 5.1.**

Work	# Fig. 5.1	Family-Type	Caloric Material	Heat transfer fluid	Geometry
[99]	1	eC-reciprocating	Ni-Ti	Water	PP
[8]	2	EC-reciprocating	PMN-MLC*	Silicone Oil	PP
[64]	3	EC-reciprocating	PVDF*	Steel bars*	PP
[7]	4	EC-reciprocating	PMN-PT*	Silicone Oil	PP
[6]	5	EC-reciprocating	Hexane	Silicone Oil	PP
[5]	6	EC-reciprocating	PST-MLC	Silicone Oil	PP
[126]	7	MC-reciprocating	Gd	Water	PP
[126]	8	MC-reciprocating	Gd	EG	PP
[126]	9	MC-reciprocating	Gd	PG	PP
[126]	10	MC-reciprocating	Gd	OO	PP
[142]	11	MC-reciprocating	Gd	Silicone Oil	PP
[142]	12	MC-reciprocating	Gd	Water	PP
[138]	13	MC-reciprocating	Gd	Water	PP
[138]	14	MC-reciprocating	La(Fe,Co,Si)13	Water	PP
[138]	15	MC-reciprocating	$(La,Ca,Sr)MnO_3$	Water	PP
[143]	16	MC-reciprocating	Gd	Helium	PP
[144]	17	MC-reciprocating	Gd	Water	Spheres
[144]	18	MC-reciprocating	Gd	Water	Spheres
[145]	19	MC-reciprocating	Gd	Air	Spheres
[146]	20	MC-reciprocating	Gd	Water	PP
[141]	21	MC-reciprocating	Gd	Water	PP
[147]	22	MC-reciprocating	Gd	Water	PP
[147]	23	MC-reciprocating	Gd	Water	PP
[147]	24	MC-reciprocating	Gd	Water	Spheres
[147]	24	MC-reciprocating	Gd	Water	Spheres
[139]	25	MC-reciprocating	Gd	Water	Spheres
[139]	26	MC-reciprocating	$LaFe_{13xy}Co_xSi_y$	Water	Spheres
[148]	27	MC-rotatory	Gd	Water	Spheres
[149]	28	MC-rotatory	Gd	Water	Spheres
[150]	29	MC-rotatory	Gd	Water	Spheres

*PVDF: poly(vinylidene fluoridetrifluoroethylene) 68/32mol%; PST: $Pb(Sc,Ta)O_3$; PST-MLC: $Pb(Sc,Ta)O_3$ multilayer capacitors; PMN-PT: $Pb(Mg,Nb)O_3$-$PbTiO_3$; PMN-PT-MLC: $Pb(Mg,Nb)O_3$-$PbTiO_3$ multilayer capacitors.

performances do not match the aimed requirements, saving time and resources. To obtain large regeneration factors, our study suggests increasing the heat exchange coefficient by

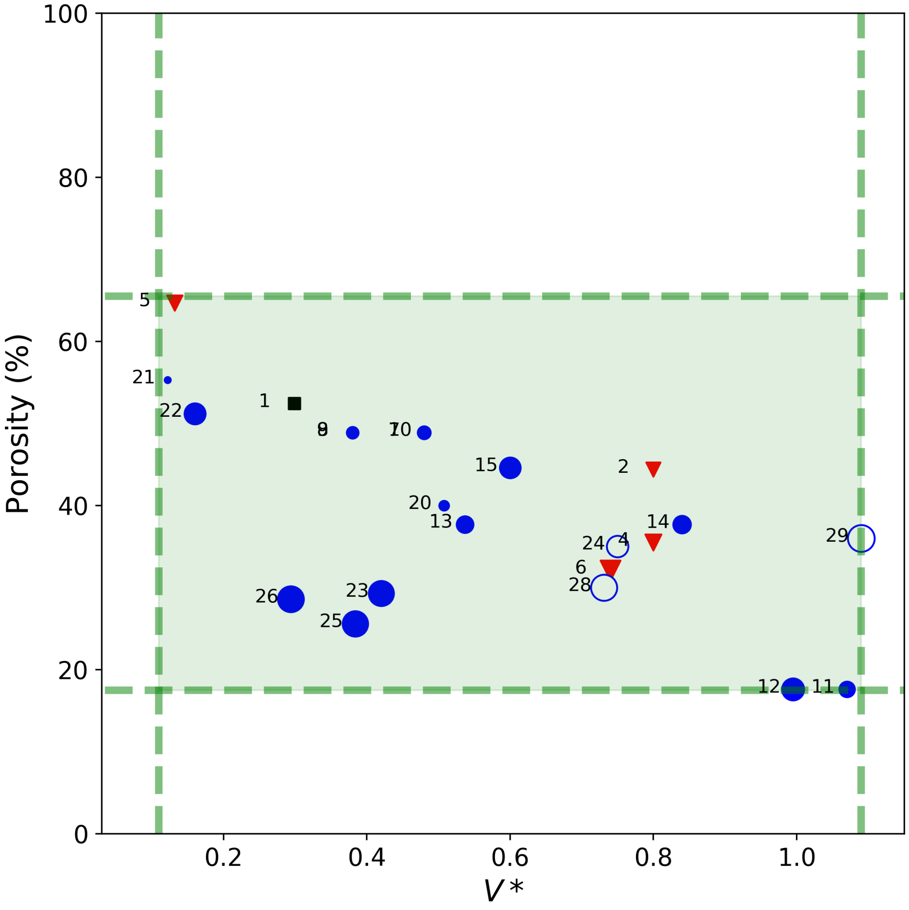

Figure 5.2 **Porosity of the caloric regenerative prototypes versus** V^* **|** The area of the markers is proportional to the regeneration factor of each point.

Table 5.2 **Regeneration factor vs the effective heat transfer coefficient.**

h_{eff} (W m^{-2} K^{-1})	$R.F.$
1500	1
3000	6
10000	6
20000	12

playing with the parameters that define it. This for instance can be done by reducing the thermal resistance of the caloric material and fluid, either by reducing their plate or slit thickness (or sphere's diameter) or by increasing their thermal conductivity. Regarding fluid velocity and cycle frequency, V^* should remain between 0.1 and 1.1, as seen in Figure 5.2.

5.5 Summary and conclusions

This work consisted of a statistical study of the performances of caloric prototypes that have been published to date. Through theoretical expressions already given in the literature, an effective heat transfer coefficient was defined for the parallel-plate and spherical particle-based regenerators. After computing this parameter for all the possible prototypes and comparing it to their regeneration factor, a linear trend with slope 6×10^{-4} was observed. The equation deduced does not depend on the caloric family, material, fluid or other involved experimental parameters, and thus is viewed as an empirical law for caloric regenerators. This highlights the importance of having an efficient heat exchange to obtain competitive regeneration factors. With the remarks mentioned in the discussion on the heat losses, caloric effect temperature window and framed porosities and V^* of the regenerator, the law presented serves as a guide to foresee the heat exchange we need for reaching a certain performance and what are the elements one must change to achieve it.

Chapter 6

Pyroelectric harvester with $Pb(Sc_{0.5},Ta_{0.5})O_3$ multilayer capacitors

This chapter investigates so-called DC bias pyroelectric energy harvesting of bespoke 1 and 0.5 mm-thick PST-MLCs samples, presented in Section 4.1. The content is based on my contribution to the publication “A 10 Joule-pyroelectric harvester”, currently under review process. The background of the topic is set in Section 6.1. Section 6.2 details the different steps of the cycles used (Olsen and Stirling cycles), emphasizing their pros and cons. In Section 6.3, the PST-MLCs are characterized in terms of the energy they can harvest depending on the temperature span they undergo and the voltage applied. Section 6.4 focuses on the description and characterization of different pyroelectric devices based on PST-MLCs. These devices are labelled as HARV1, HARV2 and HARV3. They make use of the circulation of a dielectric fluid from hot and cold reservoirs to vary the temperature. A numerical modelling on the thermalization time between the dielectric fluid and the PST-MLCs is investigated to provide guidelines on how to improve the electric power. Section 6.5 presents the methods as written in the publication. Section 6.6 summarizes and concludes the chapter.

6.1 Background

Global warming and its alarming consequences constitute one of the biggest challenges of our society. A major measure to diminish these effects consists of electrifying massive greenhouse-emitter energy consumption processes, such as vehicles and thermal management of households. These actions will have little impact in the fight against climate change though if the electricity produced does not come from sustainable and emissions-free sources.

From this motivation stems energy harvesting principles and the development of systems able to reuse natural, wasted energy sources to produce electricity. These energy harvesting processes include mainly wind mills, taking advantage of the wind's mechanical energy to activate turbines and generate electricity; thermoelectrics [151], where electricity is generated from a spatial temperature gradient within a material exhibiting the Seebeck effect; photovoltaics [152], where photons from the sun are absorbed in semiconductor materials, freeing electrons and holes; and thermophotovoltaics [153], utilizing the same principle of photovoltaic systems but absorbing instead the infrared radiation of an emitter that is purposely being heated.

Another interesting group of materials in this area are those displaying pyroelectric effects, i.e, changes in the polarization from temperature changes in the sample. Hence, differently than thermoelectrics, these materials can produce electricity from periodic oscillations of temperature in time and are thus treated as thermal engines [154, 155]. Pyroelectric harvesting was initially called "thermodielectric" effect in 1954 [156] and baptized in 1983 by Randall Olsen as "dc-bias assisted pyroelectric energy harvesting" [157]. Even though pyroelectric harvesting has shown promising prospects, the lack of macroscopic devices able to harvest energy in the joule range has limited their industrial development to sensors and low-powered appliances [158–160].

The purpose of this work is to revisit Olsen's pioneering work from the 1980s and design a pyroelectric harvester based on PST-MLCs able to generate more than 1 J of electrical energy per cycle. The motivation of utilizing PST-MLC lies on the fact that materials exhibiting large electrocaloric effects should also perform well at converting heat into electrical energy. This has been pointed out by several works, such as Sebald et al. [155], Alpay et al. [154], or, more recently, Moya and Mathur [27]. The chapter explores as well the corresponding electric power and heat exchange numerical modellings predicting higher cycle frequencies.

6.2 Thermodynamic cycles of pyroelectric harvesting

Pyroelectric energy harvesting consists of periodic temperature oscillations within a material in which an electric field is applied at the heating step (further described in more detail). Differently than thermoelectris, in which electricity is generated from a spatial temperature gradient, pyroelectric harvesting requires thermodynamic cycles such as Olsen and Stirling cycles. These are described hereunder.

6.2.1 Olsen cycles

Olsen-like pyroelectric harvesting cycles are constituted by four steps:

- Isothermal polarization of the sample (leg AB)
- Isofield heating (leg BC)
- Isothermal depolarization of the sample (leg CD)
- Isofield cooling (leg DA)

These cycle steps are displayed in Figure 6.1, which plots the electric displacement D - electric field E loops[1] of a single 1 mm-thick PST-MLC at the temperatures of 20 and 90 °C.

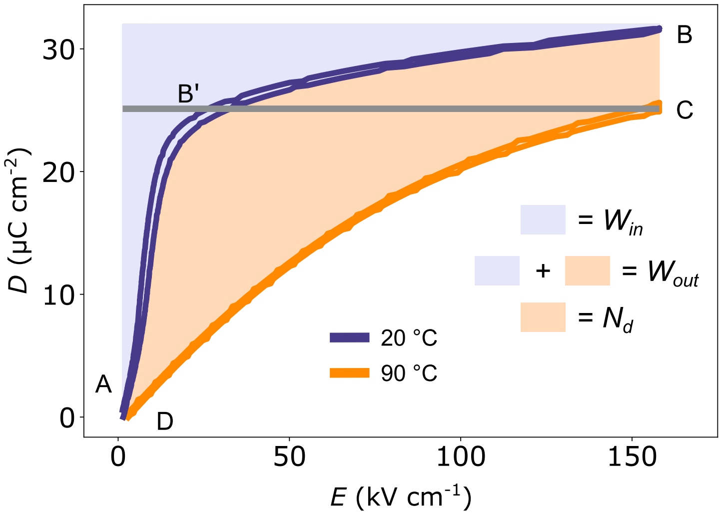

Figure 6.1 **Electric displacement - Electric field (*DE*) loops of a single 1 mm-thick PST-MLC at 20 and** 90 °C. The cycle ABCD corresponds to an Olsen cycle, whereas the cycle AB'CD to an Stirling one. The purple shaded area is the energy cost of applying an electric field (150 kV cm^{-1}), whereas the orange shaded area is the energy harvested by the sample at the completion of the cycle.

In the first step (isothermal polarization, leg AB), an electric field of 150 kV cm^{-1} is applied to a 1 mm-thick PST-MLC that is initially at 20 °C. In the second step (isofield heating, leg BC), the sample is heated up to the hot temperature (90 °C) while the electric field remains constant (150 kV cm^{-1}). In the third step (isothermal depolarization, leg CD) the electric field is removed from the sample while the latter remains hot (90 °C). Finally, the discharged sample is cooled down (isofield cooling, leg DA) to its initial temperature (20 °C). The energy density cost of applying a given electric field to a polarizable sample is given by:

$$W_e = \int \boldsymbol{D} d\boldsymbol{E} \tag{6.1}$$

---

[1] Electric displacement $\boldsymbol{D}$ and polarization $\boldsymbol{P}$ in a dielectric are related as $\boldsymbol{D} = \epsilon_0 \boldsymbol{E} + \boldsymbol{P}$, with polarization being $\boldsymbol{P} = \epsilon_0 \chi \boldsymbol{E}$. Since in ceramic ferroelectrics $\chi >> 1$ [161], $\boldsymbol{D} \cong \boldsymbol{P}$. Throughout this chapter, the electric displacement field magnitude will be used in the equations and graphs, though sometimes it will be referred to as the electric polarization for convenience.

where $\boldsymbol{D}$ is the electric displacement and $\boldsymbol{E}$ is the electric field vector. In Figure 6.1, the energy density cost of applying the electric field corresponds to the shaded purple area in the figure. On the other hand, the orange shaded area tells us the energy density N_d generated / harvested by the cycle. It can be expressed as the integral of the polarization curves over the field in the closed path ABCD

$$N_d = \oint_{ABCD} \boldsymbol{D} d\boldsymbol{E} \tag{6.2}$$

Therefore, DE-loops constitute a convenient and straightforward way of indirectly measuring the energy harvested by the sample. On the other hand, direct measurements can be provided by measuring the voltage and current of a sample that undergoes actual cycles, and integrating the product of these two magnitudes over time $E = \int_0^\tau I_{meas}(t)V_{meas}(t)dt$. This is shown in Figure 6.2, where the voltage (in black) and current (in red) as a function of time of a 1 mm-thick PST-MLC sample are displayed in the top-panel. Note that the sample undergoes the same Olsen cycle described in Figure 6.1. The calculated energy at each time step is represented in the bottom panel (in green) together with the temperature of the sample (in yellow, recorded with an IR-camera). In these energy curves, positive values of energy meant energy supplied to the PST-MLCs, and negative values meant energy provided by them, and hence, energy harvested. In the leg AB, a voltage of 600 V was applied to the sample, which was at 20 °C. The compliance current was set at 200 μA. After $\sim$ 2 s, the sample reached 600 V and the current dropped to 0 (bottom inset in top panel). This step had an energetic cost of 30 mJ. In the leg BC, the temperature of the sample was ramped up to 90 °C while the applied voltage was maintained constant (600 V). As a consequence of the pyroelectric effect, a negative pyroelectric current was generated in this step (top-right inset in top panel). Hence, the electric power became negative, decreasing the overall energy of the sample (within this context, a negative energy contribution meant that energy was being harvested). After reaching the hot temperature of 90 °C, charges from the sample were not freed anymore and the electrical energy was observed to reach a plateau. In total, 35 mJ were harvested in this step. In the CD leg, the voltage was removed from the sample at the compliance current of 200 μA, providing 60 mJ more and making a total of 95 mJ. In the last step (leg DA), the temperature was decreased to 20 °C at 0 V applied, with no contribution to the energy. Considering that 30 mJ were needed to charge the sample at the beginning, this means that at the end of the cycle 65 mJ of electrical energy were generated. The active volume of PST in the sample was 0.035 cm^3 (see Table 4.1), and hence, the volumetric energy density was 1.84 J cm^{-1}. This agrees well with the value deduced from the DE-loops in Figure 6.1, which yielded 1.78 J cm^{-1}.

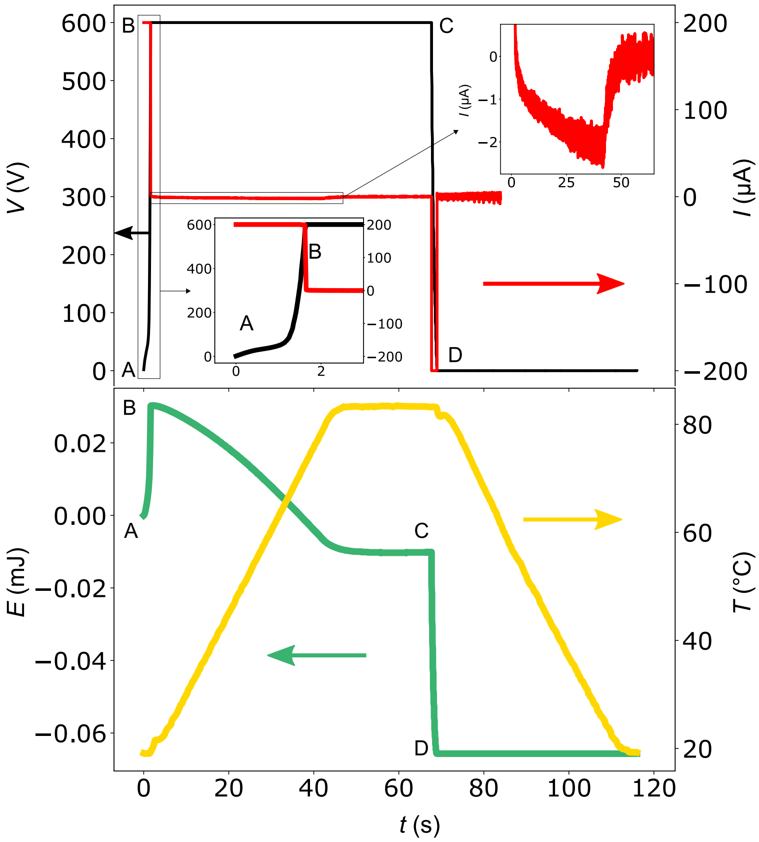

Figure 6.2 **Real Olsen cycle |** Voltage (black) and current (red) temporal profiles (top panel) of a 1 mm-thick PST-MLC undergoing actual Olsen cycles as the one displayed in Figure 6.1. The temperature of the sample (recorded with an IR-camera) and corresponding energy (deduced from the voltage and current data) are respectively displayed in the bottom panel by the yellow and green curves. The capital letters in the graphs correspond to the steps of the Olsen cycle.

6.2.2 Stirling cycles

Stirling cycles differ from Olsen cycles in BC and DA legs. They are constituted by the following steps (AB'CD in Figure 6.1):

- Isothermal polarization of the sample (AB')
- Isocharge heating (B'C)
- Isothermal depolarization of the sample (CD)
- Isocharge cooling (DA)

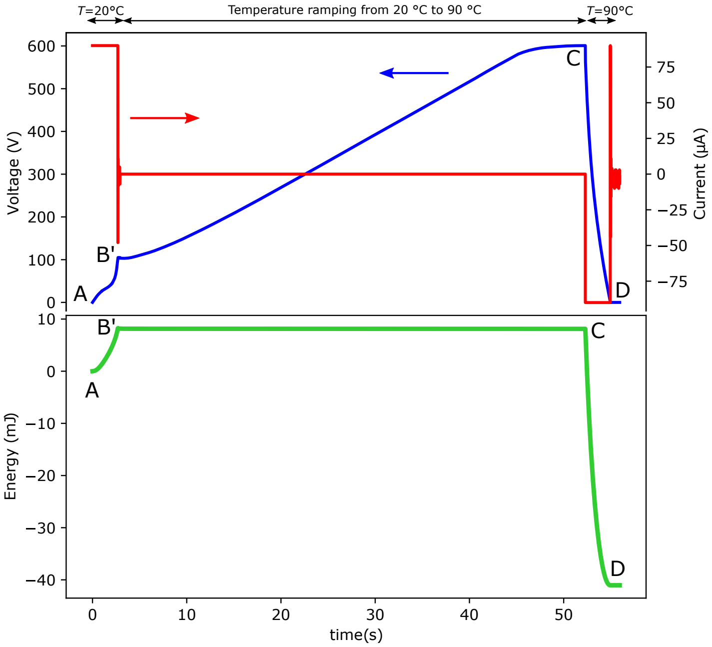

Figure 6.3 **Real Stirling cycle for a 1 mm-thick PST-MLC |** Starting temperature was T_i = 20 °C, input voltage V_i = 105 V and compliance current I = 90 μA (AB'). In leg B'C, the temperature was ramped to 90 °C. Because of the pyroelectric effect and open circuit conditions, the voltage increased to 600 V. In CD, the sample was discharged ($V = 0$). In D, the sample was cooled down to 20 °C so a new cycle could start again. In total, 41 mJ of energy were harvested at the end of the cycle.

Similarly as before, these steps can be visualized by the *DE*-loops in Figure 6.1. First, an electric field (27.6 kV cm^{-1}, 105 V) is applied to the sample at the cold temperature of 20 °C (leg AB'). This induces an electric displacement D of 25 μC cm^{-2}. At B', the electric circuit is opened, and the temperature of the sample is ramped up to the hot temperature of 90 °C. Because charges cannot leave the sample (open circuit conditions), the electric displacement remains constant. However, since the capacitance of PST decreases above its transition temperature (17 °C), the voltage of the sample increases as temperature raises up. This is shown in step C in Figure 6.1, with the voltage reaching 600 V (155 kV cm^{-1}). At C, the sample is discharged at 90 °C, reaching point D in the figure ($E = 0$, $D = 0$). In leg DA, the sample is cooled down to the initial temperature (20 °C) so that a new cycle can start again.

The corresponding actual Stirling cycle is displayed in Figure 6.3, which shows in the top panel the current (in red) and the voltage (in blue) temporal evolution measured in a 1 mm-thick PST-MLC that undergoes the cycle AB'CD described in Figure 6.1. The corresponding calculated energy is shown in the bottom panel. The energetic cost of charging the sample at 105 V and 20 °C (isothermal polarization, leg AB) was 8.13 mJ. At B', the circuit was opened (I = 0 A) and the temperature was ramped to 90 °C. As a result, the voltage in the sample increased to 600 V (C). Because of the open circuit conditions, this step did not contribute to the energy. Afterwards, the sample was discharged (V = 0) at the same compliance current (I = 90 μA), giving back 49.16 mJ (D). After substracting the initial 8.13 mJ required to charge the PST-MLC, 41.03 mJ of energy were generated. Finally, the sample was cooled down to its initial temperature (20 °C). The corresponding energy density harvested was 1.17 J cm^{-3}, not far from the 1.35 J cm^{-3} deduced from the *DE*-loops.

Note that the energy harvested in this particular Stirling cycle was 63% of the analog Olsen's cycle, with the same cold and hot temperatures. This can be noticed in the *DE* loops from Figure 6.1 as well. However, Olsen cycles require higher electric fields (and voltages) to be applied from the beginning of the cycle, which can be a challenge for certain applications. On the other hand, Stirling cycles harvest less energy in general, but smaller starting voltages are enough to harvest a decent amount of energy. This subtlety could make a difference and be key in the development of practical applications.

6.3 Harvested energy characterization of PST-MLCs

This section presents the characterization of the energy harvested by 0.5 mm-thick PST-MLCs deploying real Olsen and Stirling cycles. Data were gathered with a sourcemeter power supply (Keitlhey 2410) and a Linkcam temperature stage. A Python script automatized and synchronized the operation of both instruments. For more details, see methods in Section 6.5.

6.3.1 Olsen cycles

Figure 6.4 displays the energy harvested by Olsen cycles in a 0.5 mm-thick PST-MLC for different temperature spans and applied voltages. The starting temperature T_i was always 5 °C and the final temperature was found between 95 and 180 °C.

The maximum energy harvested was 74.9 mJ at the applied voltage of 750 V and temperature spanning from 5 to 180 °C. Considering that the active volume of the PST-MLC was 16.9 mm^3 (active area = 48.7 mm^2 * number of layers = 9 * layer thicknes = 38.6 μm), it yielded an energy density of 4.4 J cm^{-3}. This is four times larger than the highest value reported in the literature [89], where 1.06 J cm^{-3} were reported in PMN-PT films in a temperature span of 90 °C and applied field of 400 kV cm^{-1}. Other representative works from the literature were gathered in Table 6.1.

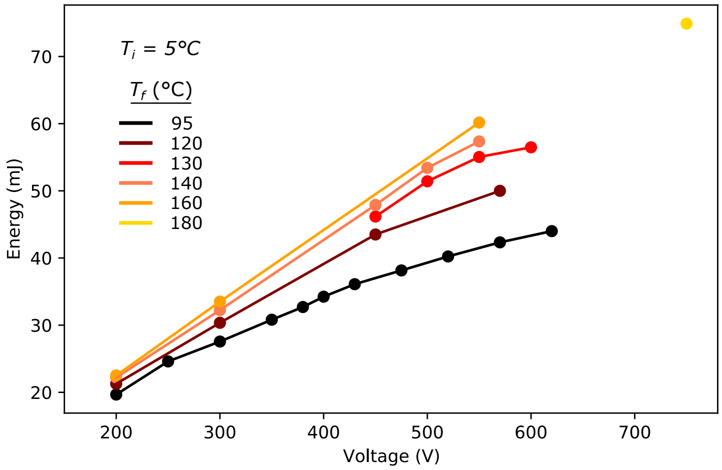

Figure 6.4 **Energy harvested with Olsen cycles for a 0.5 mm-thick PST-MLC as a function applied voltage |** The initial temperature of the cycle was 5 °C for all points. The final temperatures, represented by the legend in the figure, varied from 95 to 180 °C.

6.3.2 Stirling cycles

Figure 6.5 shows characterization of the energy harvested by 0.5 mm-thick PST-MLCs undergoing Stirling cycles. The harvested energy is displayed as a function of the output voltage measured. The data points correspond to different input voltages (15 to 50 V) and final temperatures reached (55 to 125 °C). This is represented respectively by different symbol signs and colours. The initial temperature for all points was 5 °C. The maximum energy harvested was 24.33 mJ with an input voltage of 50 V and a final temperature of 95 °C. Note that one remarkable fact of Stirling cycles is their capability to amplify the input voltage by several factors. An example of this is shown by the red square in the figure, where the initial voltage was amplified by a factor of 39 (from V_i = 15 V to V_{out} = 590 V) when undergoing temperature oscillations between 5 and 125 °C.

6.4 Design and characterization of pyroelectric harvesters

Section 6.3 showed that PST-MLCs could produce ~ 50 mJ of electrical energy from temperature oscillations between 20 and 100 °C . This envisions prototypes based on several PST-MLCs able to produce electrical energy in the Joule range. The design and characterization of three harvesting devices (HARV1, HARV2 and HARV3) is presented hereunder. Differently than previous sections, temperature oscillations were provided thanks to the circulation of a fluid from hot and cold reservoirs through the PST-MLCs, assembled previously in a porous-like stack like the designs showed in Chapter 4.

Table 6.1 **Energy harvested density of some representative works |** The data shows the energy density N_d in J cm^{-3} of representative examples from the literature performed on actual Olsen cycles at a given electric field E, initial temperature T_i and temperature span ΔT_{span}.

Material	Type - thickness (μm)	ΔT_{span} (K)	T_i (°C)	N_d (J cm $^{-3}$	E (kV cm^{-1}	Ref.
PZST	Ceramic - 250	20	145	0.12	32	[157]
0.85PMN-015PT	Ceramic - 1000	50	35	0.186	30	[155]
PZNT	Single crystal - 1000	60	100	0.24	20	[162]
60PVDF-40TrFE	Film - 50	75	25	0.52	400	[163]
PNZST	Ceramic - 500	70	150	0.8	13	[164]
8/65/35 PLZT	Ceramic - 290	135	25	0.9	75	[165]
0.68PMN-0.32PT	Thin film - 0.15	90	25	1.06	400	[89]
PST-MLC	MLC - 9 layers of 38 μm each	175	5	4.43	195	This work

*PZST = Pb0.99Nb0.02(Zr0.68,Sn0.25Ti0.07)0.98O3, PZNT = Pb(Zn1/3Nb2/3)0.955Ti0.045O3, PVDF = poly(vinylidene fluoride), TrFE = trifluoroethylene, PLZT = (Pb,La)(Ti,Zr)O3, (1-x)PMN-yPT = (1-x)Pb(Mg1/3Nb2/3)O3 – x PbTiO3, PNZST = Pb0.99Nb0.02(Zr0.637Sn0.273Ti0.09)0.98O3.

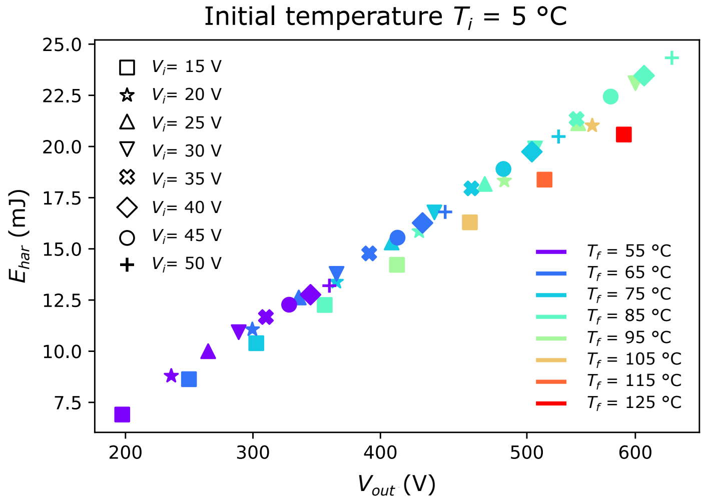

Figure 6.5 **Energy harvested with Stirling cycles for a 0.5 mm-thick PST-MLC as a function of the output voltage |** The initial temperature of the cycle is 5 °C for all points, and the input voltage takes values from 15 to 50 V, as the symbols in the legend show. The colour legend indicates the final temperature of each cycle/point.

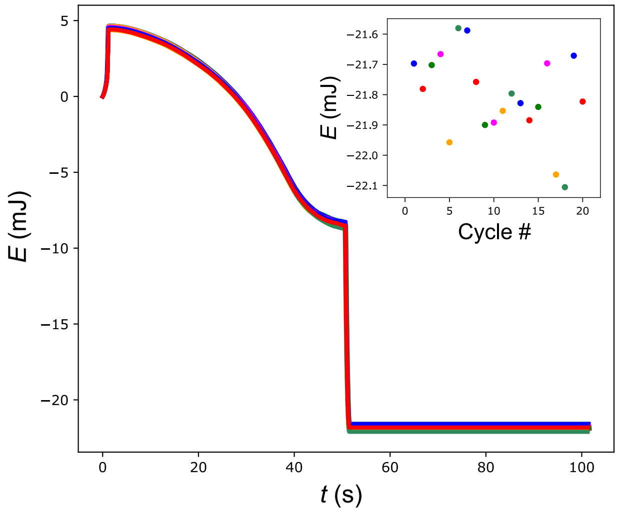

Figure 6.6 **Reproducibility of real Olsen cycles |** Temporal profile of the energy of a 1 mm-thick PST-MLC sample that undergoes 20 consecutive Olsen cycles with isofield legs at 0 and 80 kV cm^{-1} (300 V) and isothermal legs at 5°C and 70°C (time resets after each cycle for clarity). The inset shows the energy harvested at the end of each cycle.

6.4.1 Reproducibility of Olsen harvesting cycles

Before going any further, reproducibility of Olsen cycles must be first verified. To do so, 20 Olsen cycles were run consecutively in a 0.5 mm-thick PST-MLC. This is displayed in Figure 6.6, where the corresponding energy harvested throughout the cycle is plotted as a function of time. Note that the absolute time value is reset between cycles, so that each cycle is purposely plotted as if started at $t = 0$. The inset of the figure shows the final energy (total energy harvested) for each single cycle. These values were found to be between 21.58 and 22.11 mJ, yielding an average value of 21.80 ± 0.03 mJ [2]. The overlap of the different energy time evolution curves in the figure proved the reproducibility of our Olsen cycles as well.

6.4.2 Harvester 1 (HARV1)

A macro-harvester prototype (HARV1) was built with 28 1 mm-thick PST-MLCs, assembled in a parallel-plate matrix of 7-columns x 4-rows, following the design described in Chapter 4, with a fluid slit of 1 mm. The goal with this device was to harvest energy in the Joule-range.

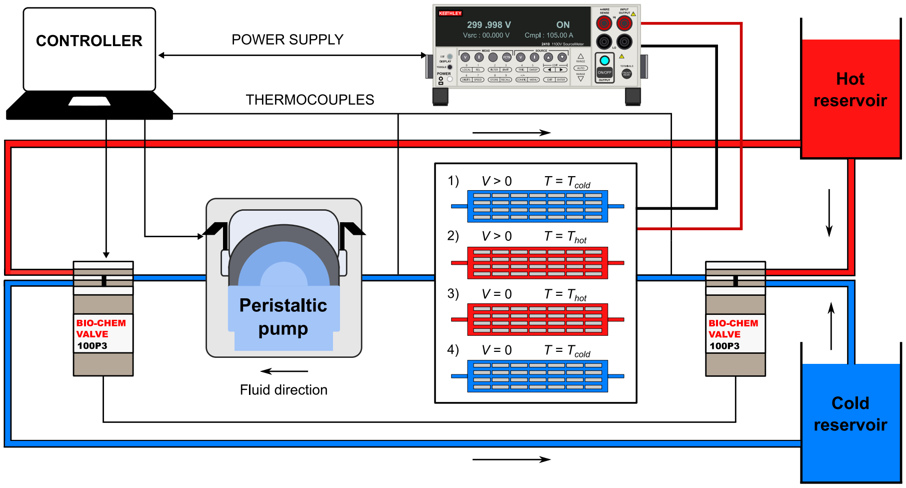

Figure 6.7 **Expermental set-up of HARV1 |** It contains the harvester, made of 28 1 mm PST-MLCs, a peristaltic pump, two valves, hot reservoir, cold reservoir, power supply and controller.

The experimental set-up of HARV1 is depicted in Figure 6.7. It consisted of two fluid closed loops (hot and cold) in which a dielectric fluid (silicone Oil, viscosity 5 cSt) was pumped in an unidirectional manner thanks to a peristaltic pump, placed right at the outlet of the PST-MLC stack. Two pinched valves chose accordingly which fluid loop Was to circulate through

---

[2] Statistical error calculated from $\sigma_{\bar{x}} = \frac{\sigma}{\sqrt{N}}$, being $\sigma = 0.14$ the standard deviation and $N = 20$.

the stack. Hot and cold reservoirs close to the prototype inlet maintained the temperature of the fluid at the desired temperature. For the hot reservoir, a vessel containing dielectric fluid silicone oil 5 cSt was placed on top of a hot plate. For the cold reservoir, copper tubes containing the dielectric fluid were submerged in a water tank with ice. A Keithley 2410 power supply charged and discharged the PST-MLCs (which were electrically connected in parallel) at the desired voltage and compliance current. Thermocouples embedded in the fluid tubing measured the temperature of the fluid at the entry and exit of the PST-MLC stack. Pump, power supply, valves and thermocouples were governed and synchronized with a controller thanks to a Python script so that Olsen cycles were deployed.

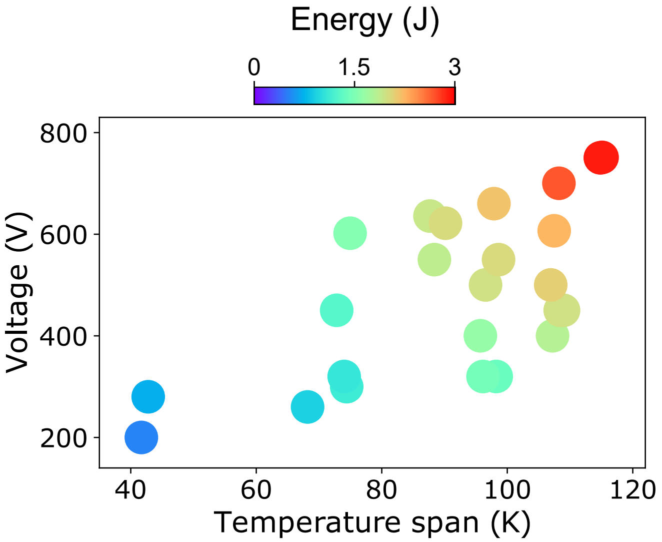

Figure 6.8 **Energy harvested by HARV1 |** Energy generated (colour legend) by the 28 PST-MLCs harvester (HARV1) as a function of the temperature span and applied voltage. A maximum energy of 3.1 J was harvested at 750 V and 115 K.

Figure 6.8 displays the energy harvested by HARV1 from all experiments run. The energy is shown by the colour legend as a function of the temperature span (x-axis) and the applied voltage (y-axis). The colour legend of the data points shows a linear-like behaviour of energy in respect to temperature span and voltage. A maximum energy harvested of 3.1 J was measured at 750 V (195 kV cm^{-1}) and temperature span 115 K, with isothermal legs at 10 °C and 125 °C. The period of this cycle was $\tau = 57$ s, mostly because of the long thermalization time τ_{therm} between PST-MLCs and fluid (26 s heating and 26 s cooling). With this period, the electric power was found to be 54 mW.

Exploration of better power results was carried out with finite elements software by coupling heat transfer and fluid dynamics phenomena with the non-isothermal laminar flow module. Simulations consisted of a time dependent 2D representation of the macroscopic harvester

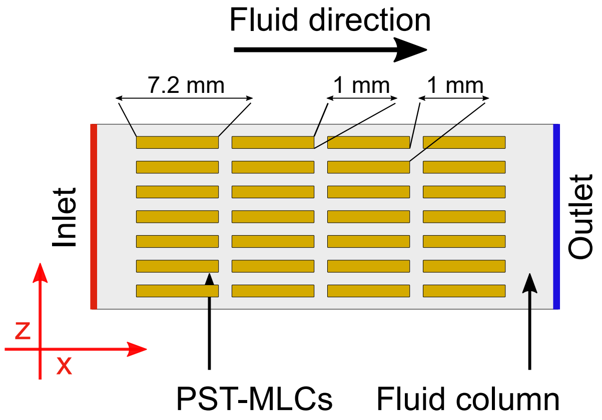

Figure 6.9 **2D Comsol simulations schematics of HARV1 |** 28 1 mm-thick PST-MLCs (yellow rectangles) were structured in a parallel-plate matrix of 4-columns and 7-rows within a fluid column (gray rectangle). An inlet and outlet boundary conditions allowed the fluid to be moved in an unidirectional manner through the PST-MLCs.

prototype. The geometry simulated included only the fluid column and the 28 1 mm-thick PST-MLC matrix (Figure 6.9). In the simulations, the fluid from the hot reservoir (set at 115 °C) was sent through the PST-MLC matrix (initially set at 10 °C) at the desired flow rate. To help the numerical integration, a 2 s linear ramp of the velocity was set first. At $t = 2$ then, the fluid inlet became 115 °C, simulating the time it took the fluid to travel from the reservoir to the harvester, which was approximately 2 s. This time was identified as waiting time τ_w. Correspondence with the experimental value (54.4 mW) was verified by computation of the time that the average temperature of the PST-MLCs thermalized with the temperature of the incoming fluid (thermalization time τ_t) plus the already defined waiting time. The first fluid simulated was silicone oil (same as in the experiment) and the PST-MLC matrix consisted of 7-columns x 4- rows. In the simulations, the thermalization time observed was $\tau_{therm} = 25.2$ s. Adding the 2 s of τ_w, this yielded a total cycle period $(2\tau_w + 2\tau_{therm})$ of 54.4 s, very close to the 57 s of the experiment. Additional simulations were run for different PST-MLC thicknesses and various configurations. They are shown in Figure 6.10. In the first one, water was used as a fluid while keeping the same parallel-plate (PP) matrix (7-columns x 4-rows, green squares in the figure). In the second one, water was kept as a fluid but the PP-matrix was reversed to 4-columns x 7-rows (dark green triangles). Finally, the latter was repeated but imposing $\tau_w = 0$ (dark green plus sign). Experimentally, this means bringing hot and cold fluid reservoirs to the PST-MLCs stack inlet. As a matter of fact, the porosity of the harvester was kept constant in all the points (50%), meaning that the fluid slit was changed accordingly to the PST-MLC' thickness change. The fluid flow in the simulation was set initially equal to the experimental one (112 mL min^{-1}). In the reversed PST-MLC matrix configuration (4-columns x 7-rows), the fluid flow was increased accordingly so that the fluid velocity through the PST-MLC channels was always the same

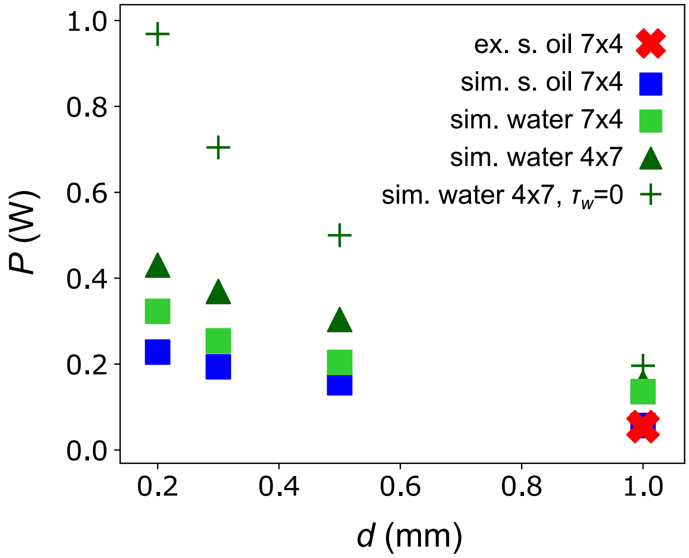

Figure 6.10 **Harvester power in several configurations as a function of the PST-MLC thickness** | These include: experimental value (red cross), corresponding simulation match (blue square), utilizing water instead of silicone oil (light green square), reversing the PST-MLC parallel plate matrix to 4 columns x 7 rows (dark green triangle) and making waiting time $\tau_w = 0$ (dark green plus sign).

(112 x (7/4) = 196 mL min^{-1}). The properties of the materials as well as the complete geometry dimensions can be consulted in Tables A.9 and A.10. 3.1 J were assumed to be harvested in all cases because: 1) 750 V were assumed to be applied, 2) the temperature span was 115 K, and 3) the total PST-MLC mass remained the same. To calculate the simulated power, the energy value of 3.1 J was divided by the cycle period simulated ($2\tau_w + 2_{therm}$).

6.4.3 Harvester 2 (HARV2)

A second macro-prototype was built with eight single units made of PST-MLCs (Figure 6.11) following the experimental set-up of HARV1. Four of these units (left-hand side in the figure) were structured in a parallel-plate matrix of 8 rows x 5 columns of 0.5 mm-thick PST-MLCs, and the other four (right-hand side) were in a parallel-plate matrix of 5 rows x 3 columns of 1 mm-thick PST-MLCs. The fluid circuit was divided into two circuits (yellow tube and white plug-in connectors), each with their own cold bath and fluid reservoir. The hot reservoir was shared by the two fluid circuits, with no fluid returning so that its temperature was not altered. Two pinched valves selected accordingly whether to pump from the cold bath (to cool down the PST-MLCs units) or the hot reservoir (to

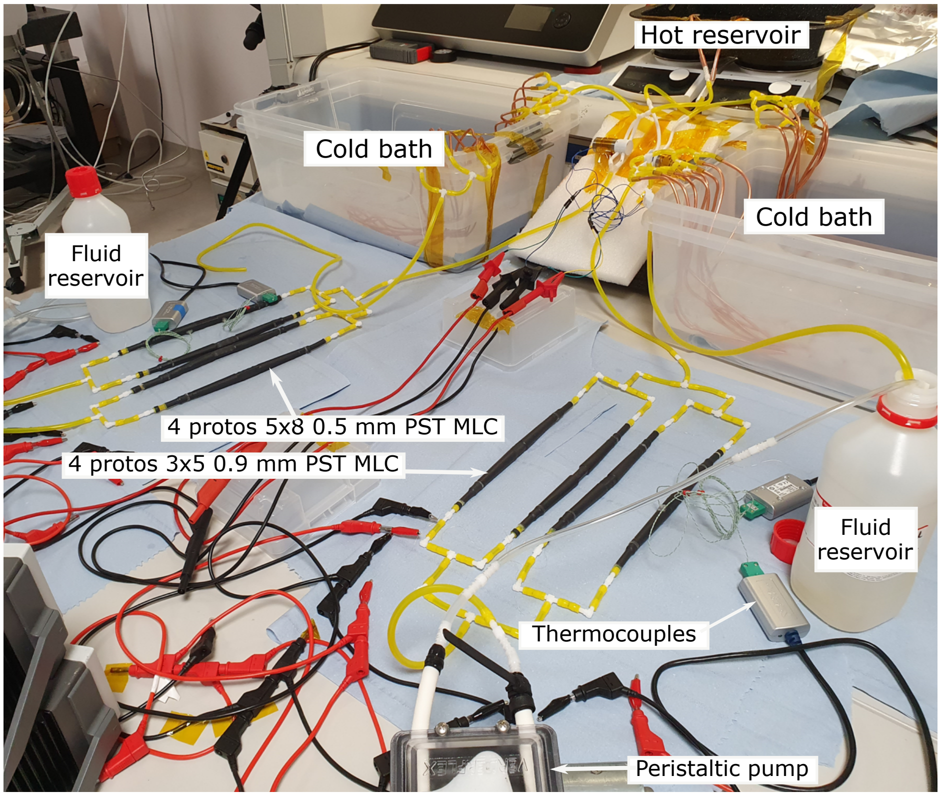

Figure 6.11 **Experimental set-up and design of HARV2 |** It contains the hot and cold fluid reservoirs, the peristaltic pumps, the fluid tubing and the eight single units, four of them made of 0.5 mm-thick PST-MLCs and the remaining four of 1 mm-thick PST-MLCs. Thermocouples are embedded into the prototypes to measure the inlet and outlet fluid temperature. Electrical connectors connect all eight units electrically in parallel.

heat them up). The eight units were connected electrically in parallel and were charged and discharged from a sourcemeter. Thermocouples were added at the inlet and outlet of two PST-MLC units to monitor temperature. Sourcemeter, valves, thermocouples and pump were governed and synchronized with a Python script similar to HARV1.

The results gathered by HARV2 are displayed in Figure 6.12, where the energy of HARV2 is plotted as a function of time. An Olsen cycle was run under 500 V (131 kV cm^{-1}) and a temperature span of 87 °C. The isothermal legs were at 11 °C and 98 °C. Note that 2 J were required to charge all PST-MLCs (AB leg). In the heating leg BC, 7.5 J were harvested, yielding a total energy of -5.5 J. When discharging the PST-MLCs (CD), an extra 5.7 J were gained, making the total energy generated in the cycle 11.2 J. This is twice the value that Olsen obtained in 1984, which is the only comparable value of energy in the Joule range [166]. He obtained 6.23 J with 317 g of active material (tin doped PZT) around 150°C. The cycle period of HARV2's performance was 240 s (120 s the semi-cycle). This

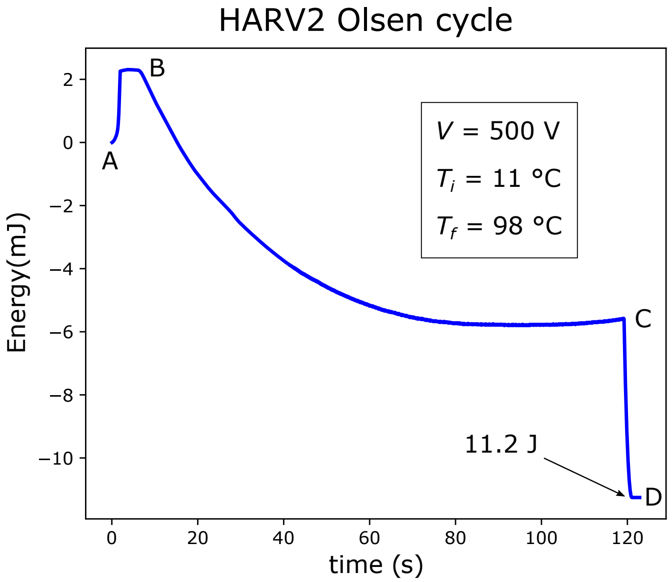

Figure 6.12 **Energy of the Olsen cycle run in HARV2 vs time |** In cycle's step A, the PST-MLCs in HARV2 were charged to 500 V (E = 131 kV cm^{-1}) at a current of 15 mA and temperature Ti = 11 °C. The energetic cost for that was 2.3 J. At B, the hot fluid started circulating and heated up the PST-MLCs. As a result, HARV2 started harvesting energy, reaching -6 J at C, once the PST-MLCs reached thermal equilibrium with the hot fluid at a temperature of 98 °C. Right after that, PST-MLCs were discharged, and the energy harvested reached 11.2 J (D). At this point, the cold fluid started circulating, cooling down the temperature of the PST-MLCs so that another cycle could be started again.

yielded a power of 47 mW, slightly lower than the power generated by HARV1, though with almost four times less energy. The reason for such a long thermalization time (120 s) is the peristaltic pump used in the HARV2-120 sub-unit (4 prototypes of 40 0.5 mm-thick PST-MLCs each), which had a limited flow rate of 112 mL min^{-1}. Additional experiments utilizing a bigger peristaltic pump (maximum flow rate was 1 L min^{-1}) in one single unit alone revealed that thermalization time could be reduced to 52 s.

6.4.4 Harvester 3 (HARV3)

A third harvester (HARV3) was built to boost the electrical power. HARV3 consisted of one single 0.5 mm-thick PST-MLC, following the same design and experimental set-up than HARV1 and HARV2 (this includes tubes, pump, hot and cold reservoirs, thermocouples and valves). 0.5 mm-thick fluid slits were set at the top and bottom of the MLC for the fluid to flow through. The results obtained when operating an Olsen cycle under 195 kV cm^{-1} from 10 to 130 °C are shown in Figure 2.7. The thermalization time τ_{therm} between the

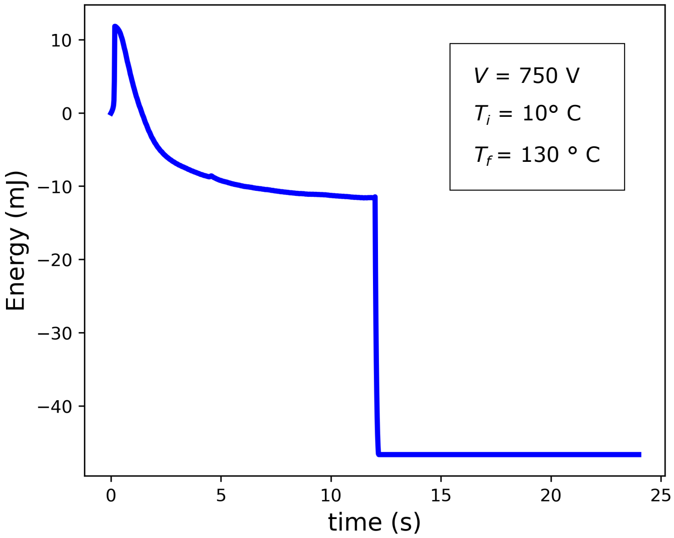

Figure 6.13 **Energy time evolution of HARV3 running under Olsen cycles |** The applied voltage was $V = 750$ V ($E = 195$ kV cm^{-1}) and the temperature span ~ 120 °C (10 °C to 130 °C). The harvested energy was 47 mJ and the period cycle of 24 s. This indicates a cycling power of 1.95 mW (per each 0.5 mm-thick PST-MLC)

fluid and the PST-MLC was 12 s, yielding a total period τ of 24 s. The amount of energy harvested was 47 mJ, giving rise to an electric power of 1.95 mW (per MLC). This result envisions a potential electrical power of ~ 0.5 W for HARV2 (ten times higher than the current value (45 mW)), if all 180 samples were to be connected in parallel in respect to the fluid, that is, a parallel plate matrix of 1 column x 180 rows.

6.5 Methods

6.5.1 Experimental set-up of the Olsen cycles

The heart of this chapter is based on Olsen cycles. For such cycles, we need a cold and a hot heat reservoir and a power supply able to control and monitor the voltage and current in the different MLC modules. Two different configurations have been used for these direct cycles, namely 1) a Linkam module heating and cooling one single MLC associated with a Keithley 2410 energy supply and 2) a prototype based on 28 MLCs connected in parallel with the same energy supply. In the latter case, a dielectric fluid (silicone oil of viscosity 5 cSt at 25 °C, purchased from Sigma Aldrich) has been used to exchange heat between the two reservoirs (hot and cold) and the MLCs. The hot reservoir consisted of a glass vessel that contained the dielectric fluid and was placed on top of a hot plate. The cold reservoir consisted of a thermal bath of the fluid tube containing the dielectric fluid in a large plastic vessel filled with water and ice. Two 3-way pinch valves (Bio-Chem Fluidics) were placed at each end of the harvester to properly switch the fluid flow from one reservoir to the other (Figure 6.7). Alternatively, we confirmed these direct measurements of harvested energy with an indirect method. These indirect methods were based on polarization P – electric field E loops collected at different temperatures and enabling an accurate estimation of how much energy can be harvested by calculating the area in between two *DE* loops, as depicted in Figure 6.1. These *DE* loops were collected with the Keithley sourcemeter as well.

6.5.2 Harvester prototypes description

HARV1 28 1 mm-thick PST-MLCs were assembled in a 7-column x 4-row parallel plate structure following the design described in [12]. The fluid slit in between the PST-MLC rows was 0.75 mm. This was achieved by adding double sided tape stripes acting as fluid spacers at the edges of the PST-MLCs. The PST-MLCs were electrically connected in parallel with silver epoxy bridges that contacted the electrode terminals. After that, a wire was glued with silver epoxy to each electrode terminal side so that it could be connected to the power supply. Finally, the entire structure was inserted into a polyolefin hose and the polyolefin hose was glued to the fluid tubes to ensure proper sealing. At the end, type K thermocouples 0.25 mm-thick were embedded at each end of the PST-MLC structure to monitor the temperature of the fluid's inlet and outlet. To do so, the hose had to be first perforated. Once the thermocouple was embedded, the same glue as before was applied in between the hose and the thermocouple wire to ensure back the sealing.

HARV2 Eight individual prototypes were built, four of them with 40 0.5 mm-thick PST-MLCs each, distributed in 5-column x 8-row parallel plate structures, and the other four with 15 1 mm-thick PST-MLCs each, distributed in 3-column x 5-row parallel plate structures. The total number of PST-MLCs used was 220 (160 0.5 mm-thick and 60 1 mm-thick PST-MLCs). We refer to the two sub-units as HARV2_160 and HARV2_60. The fluid slit in HARV2_160 prototypes consisted of two stripes of double sided-tape 0.25 mm-thick and a 0.25 mm-thick wire in between them. For HARV2_60 prototypes, we repeated the same procedure but with 0.38 mm wires instead. For the sake of symmetry, HARV2_160 and HARV2_60 had their own fluid circuit, pump, valve, and cold side. The hot reservoir, a 3 L (30 cm x 20 cm x 5 cm) recipient on top of two hot plates with rotating magnets, was shared by the two HARV2 subunits. All eight individual prototypes were connected electrically in parallel. In the Olsen cycle that led to 11.2 J of energy harvested, subunits HARV2_160 and HARV2_60 were operated simultaneously.

HARV3 One single 0.5 mm-thick PST-MLC was placed in the polyolefin hose, with double-sided tape stripes and wires at the sides to create spacers for the fluid to flow through. Because of its smaller size, the prototype was placed next to the valve that supplied fluid from either the hot or cold reservoir.

6.5.3 Olsen Cycles

A constant electric field was imposed in the PST-MLCs by applying a constant voltage throughout the heating leg. As a result, a negative pyroelectric current was generated, harvesting energy. After the PST-MLCs were heated up, the field was removed ($V = 0$), and the energy stored in them was brought back to the sourcemeter, adding another contribution to the energy harvested. Finally, at the applied voltage $V = 0$, the PST-MLCs were cooled down to its initial temperature so that a cycle could start again. In this step, no energy was harvested. These Olsen cycles were run with a Keithley 2410 sourcemeter by charging the PST-MLCs at voltage source and setting the current compliance to the appropriate value so that enough points in the charging step were gathered to calculate reliably the energy.

6.5.4 Stirling Cycles

In Stirling cycles, PST-MLCs were charged in voltage source mode at an initial electric field value (input voltage $V_i > 0$), desired compliance current (so that the charging step lasted $\sim$ 1 s), and cold temperature. Before the PST-MLC was heated up, the electric circuit was opened by imposing current compliance $I = 0$ mA (the lowest value of current compliance that our sourcemeter can take is 10 nA). As a result, charges were kept in the PST-MLCs and voltage increased while the sample was heated up. In the BC leg, no energy was harvested because $I = 0$ mA. After the hot temperature was reached, the PST-MLCs were discharged ($V = 0$), and the electrical energy stored in them was brought back to the sourcemeter at the same current compliance that they were charged initially. Because of the voltage amplification, the energy stored at the hot temperature was higher than the energy supplied at the beginning of the cycle. Thus, energy was harvested from converting heat into electrical energy.

6.6 Summary and conclusions

This chapter explored the capability of bespoke PST-MLCs in converting heat into electrical energy by revisiting Olsen's pioneering work from the 1980's. This sort of energy conversion, known today as "dc-bias assisted pyroelectric energy" harvesting, consists of cyclical thermal oscillations within a pyroelectric material under the application of an electric field in the heating step. The main achievements presented in this chapter are:

- The development of a numerical modelling based on HARV1's data predicting cycle frequencies of 0.33 Hz when: 1) the PST-MLCs were thinned to 0.2 mm; water as used as a heat transfer fluid; 3) the PP-matrix was reversed to 4 columns x 7 rows; and 4) the hot and cold fluid reservoirs were placed at the PST-MLC stack entry. The corresponding electrical power of HARV1 with a cycle frequency of 0.33 Hz was 1 W.

- The design and characterization of a harvesting prototype (HARV2) able to generate 11.2 J when undergoing an Olsen cycle at 750 V (195 kV cm^{-1}) and temperature span from 10 to 98 °C. This is twice the best value reported in the literature (6.23 J [166]), with eight times less pyroelectric material (42 g vs 317 g).

- The design and characterization of a harvesting prototype (HARV3) able to generate 1.95 mW per MLC when undergoing Olsen cycles at 750 V (195 kV cm^{-1}) and temperature spans from 10 to 130 °C. This envisions an overall experimental power of 0.5 W for HARV2's design.

- A maximum energy density of 4.4 J cm^{-3} in a 0.5 mm-thick PST-MLC undergoing an Olsen cycle at 750 V (195 kV cm^{-1}) and 5 to 180 °C. This is four times larger than the best value reported in the literature, 1.06 J cm^{-3} [89].

The results obtained are beyond the state of the art and are explained thanks to the excellent properties of PST-MLCs, namely 1) a sharp first-order phase transition close to room temperature (T_C = 17 °C), 2) extremely low leakage current preventing electrical losses and 3) possibility to apply very large electric fields thanks to the multilayer assembly. The high performance reported highlights the need of reconsidering this sort of energy conversion for future applications producing carbon-free electricity.

Chapter 7

Conclusions and perspectives

This dissertation focuses on the development of energy-conversion applications, such as heat pumps and energy harvesters, that exploited electrocaloric and pyroelectric effects of multilayer capacitors (MLCs) of $Pb(Sc_{0.5},Ta_{0.5})O_3$, fabricated at Murata Manufacturing (Japan). The previous six chapters are summarized hereunder, and future perspectives are provided alongside.

Chapter 1 provided a general introduction to the entire manuscript, contextualizing the topic of electrocaloric cooling and heat energy harvesting, as well as presenting the research questions, objectives and overall structure of the thesis.

Climate change and its dramatic effects is mostly a consequence of the greenhouse (GH) emissions. Among the different kinds, hydrofluorocarbon (HFC) refrigerants are especially harmful because they possess global warming potential thousands of times larger than that of carbon dioxide CO_2. In addition, the demand for cooling and refrigeration units is expected to rise as the consequences of climate change become more stringent, worsening the whole scene. Electrocaloric (EC) materials have been identified as a promising GH-free alternative to current refrigerants. However, EC demonstrators have failed at displaying competitive temperature variations and their industrial development has been discouraged for years. The content of this dissertation attempted to demonstrate that EC coolers can indeed display temperature variations larger than 10 K, and provided hints and guidelines on how to increase them even further. For completeness, pyroelectric effects on the same samples were investigated in order to produce low-carbon electricity from wasted heat. The aim was to develop convincing demonstrators able to generate electrical energy in the joule range.

Chapter 2 recapped the basic principles of EC and EC heat pumps, starting with an explanation of the phenomenology of EC effects and a review of the main EC materials.

The latter were classified according to their geometrical configuration as bulk, thin-films and multilayer capacitors (MLCs). The multi-layer structure was identified to be the most suitable for EC applications because it congregates the advantages of bulk and thin-films. On one hand, MLCs are macroscopic objects with a similar amount of thermal mass than bulk materials. Thus, as opposed to thin-films, it is possible to make use of the heat that they generate. On the other hand, their thin active layers (typically tenths of micrometers thick) notably decrease the applied voltage, allowing higher electric fields to be induced and, hence, displaying larger temperature changes.

Schematics of heat pumps and their thermodynamic cycles were also provided. The focus was put onto heat regenerative cycles able to display temperature differences (between hot and cold sides) larger than the adiabatic temperature change ΔT_{EC} of the materials. These kinds of cycles are crucial to be operated in EC-based heat pumps because most EC materials display temperature variations (< 5 K) much lower than the values that commercial applications demand (> 20 K). The chapter ended with the basics of numerical models of fluid-based EC regenerators, providing a detailed example of one that utilizes finite elements methods.

Chapter 3 consisted of an exhaustive review of the literature on EC devices. Each of these works was carefully scrutinized, providing graphs and tables that summarized the most relevant data. A general classification was made between EC coolers based on the circulation of a heat transfer fluid (fluid-based) and those that employed exclusively solid elements (solid-based). The idea behind this cataloging was to compare their working principles and performances, highlighting their pros and cons.

Fluid-based EC prototypes represent the most common kind of EC heat pumps. While they have shown larger temperature spans and regeneration factors, they have barely reported cooling power and efficiencies. The main advantages of fluid-based devices were identified to be 1) the optimum thermal contact that solid-fluid interfaces entail, and 2) their handy and robust structures, such as the widely studied parallel-plate assembly in active regenerators, favouring their industrial development. On the other hand, the disadvantages of fluid-based devices were identified to be 1) the non-negligible inactive thermal mass of the fluid itself, diminishing the overall performance, and 2) the difficulty to deploy high cycle frequencies in fluid media. The latter would also involve the operation of large flow rates, promoting turbulence that degrades the temperature gradient. In addition, fluid-based prototypes require the operation of fluid pumps which may have a non-negligible power consumption, and hence, should not be overlooked.

Solid-based prototypes are in comparison less numerous than fluid-based. While they have shown more accurate and optimistic studies in cooling power and efficiencies (up to 2800 W

kg^{-1} of active EC material and $COP_{Carnot} \sim 10\%$), they have shown also more limitations on displaying competitive temperature spans (> 10 K). The highest temperature span reported so far was 8.7 K [26], which is remarkable considering the low amount of EC material that was used (96 mg). Thus, the successful construction of more massive prototypes should enable solid-based coolers to easily increase their temperature spans, though this needs to be experimentally validated. Among the different working principles of solid-solid devices, those following cascading cycles were identified to be especially interesting because 1) they do not require inactive material to exchange heat ("the refrigerant is also the pump" [167]), and 2) the mechanical actuators used showed negligible power consumption [9, 25, 26, 66]. While these approaches are unique and very promising, these devices entail some disadvantages such as 1) their designs are more complex and delicate than fluid-based prototypes, involving a higher degree of engineering, and 2) solid-solid interfaces are typically junctions of high thermal resistance because of their weak physical contact, which hinders heat transfer. This could be improved though by using flexible surfaces that are bound together thanks to their electrostatic interaction [95], like PVDF, as has been already shown in a couple of devices [9, 26].

Ultimately, the performance of both fluid- and solid-based EC heat pumps could be utterly improved if 1) the amount of active EC mass is increased, 2) higher EC effects are triggered, and 3) heat losses are minimized. The second point could be attained by developing materials that have (i) larger pyroelectric effects (as is the case of sharper first-order phase transitions), and (ii) higher breakdown fields (so that higher electric fields could be applied). The latter point, on reducing the heat losses, could be achieved by (i) deploying higher cycle frequencies (though this would require firstly an enhancement of the heat transfer, as Chapter 5 suggests), and (ii) improving the thermal insulation (as could be done with vacuum surroundings, for instance).

Aside from implementing these modifications, future works should report durability and reliability studies showing whether EC heat pumps can indeed sustain the amount of cycles that real-life applications demand ($\sim 10^6$ cycles). In regards to this, some preliminary work has been already performed at the material's level, focusing on the fatigue-life of EC effects. Examples of these are:

- Fulanovic et al. [168] and Del Duca et al. [169], both showing almost no degradation of the EC effect magnitude (less than 5%) after 10^6 unipolar cycles in MLCs of $Pb(Mg_{1/3}Nb_{2/3})O_3$ under 110 kV cm^{-1} and bulk relaxor ferroelectric $0.9Pb(Mg_{1/3}Nb_{2/3})O_3$–$0.1PbTiO_3$ (PMN-10PT) under 90 kV cm^{-1}, respectively.
- Qian et al. [59], observing no changes in the EC properties of poly(vinylidene fluoride-trifluoroethylene-chlorofluoroethylene) terpolymer after 62×10^3 cycles at low fields (500 kV cm^{-1}, 20% of its breakdown field).

Chapter 4 explored the design, construction and characterization of customized fluid-based EC regenerators made of PST-MLCs. The motivation behind this work was to exploit the excellent qualities of PST-MLCs (large EC effects near room temperature, displayed in a wide temperature range [12], but also their handiness and easy manipulation), in the operation of subsequent coolers able to display temperature spans larger than 10 K. The design of this novel heat pump was based on the outcome of a numerical model that stressed the need for 1) reducing the inactive mass of the overall design and 2) improving the thermal insulation of preliminary designs. The main set of experimental modifications that were implemented in this novel design were:

1) removal of all inactive structural elements, including frames, fluid diffusors and EC housing, simplifying the overall design;

2) replacement of 1 mm-thick PST-MLCs by thinner ones (0.5 mm) to increase the heat exchange surface and thus, improve heat exchange. Accordingly, the fluid slit was reduced from 0.5 mm to 0.25 mm so that the porosity of the device was kept the same;

3) enlargement of the length of the regenerator (by implementing more PST-MLCs) to promote the creation of a temperature gradient;

4) sealing off the PST-MLC stack with a polyolefin hose, which minimized the fluid dead volume and has a negligible thermal mass;

5) application of a 15 cm-wide polyurethane foam wall around the prototype in order to improve thermal insulation.

The resulting device (labelled as REG2) consisted of 128 0.5 mm-thick PST-MLCs, distributed in a parallel-plate (PP) matrix of 16 columns x 8 rows. This device was able to display temperature spans as large as 13 K near room temperature under 155 kV cm^{-1}, and a maximum predicted cooling power of 32 W kg^{-1} under the same conditions. The latter was deduced from a model based on the experimental data from a similar device (labelled as REG3), that consisted of 32 1 mm-thick PST-MLCs distributed in a PP-matrix of 8 columns x 4 rows. REG3 reported a maximum experimental cooling power of 12 W kg^{-1} of active material under an electric field of 40 kV cm^{-1}. It is important to underline that the parallel-plate matrices of REG2 and REG3 did not have regular and homogeneous fluid channels (in some cases these were even closed) due to the uneven shape of bespoke PST-MLCs. This, which was caused by the long and high-temperature annealing process ($\sim$ 1000 h at $\sim$ 1000 °C), hindered heat transfer, diminishing the overall performance. Therefore, it would be of great interest that future works could find a solution to this problem, and experimentally test what the added value of flat and even MLCs would be.

Further numerical analyses in modified regenerators were able to predict temperature spans as large as 50 K and cooling powers in the order of 1000 W kg^{-1} of active EC material. These modifications consisted of:

1) reduction of the PST-MLC thickness to 0.25 mm for even better heat exchange. Accordingly, the fluid slit was reduced from 0.5 mm to 0.125 mm so that the porosity was the same;
2) deploying a higher EC effect of 5.5 K, which was measured recently in better ordered PST-MLCs [12];
3) utilizing water as a heat transfer fluid for better heat exchange.

The first of the previous points (reducing PST-MLC thickness) is in accordance with the findings reported in Chapter 5 and highlights the need to improve heat transfer in order to reach better performances. In the case of active regenerators, this relates more specifically to an enhancement of heat transfer in the perpendicular flow direction. In the parallel flow direction (where the temperature gradient is built along) heat transfer should be minimized. This ideal anisotropic-like heat transfer is typically achieved thanks to geometrical deformations by 1) decreasing the plate's thickness (in this case PST-MLC thickness, around 0.2 mm), and 2) enlarging the length of the plate (number of columns in the PP-matrix). More sophisticated ways could be developed with engineered structures that entail an anisotropic thermal conductivity. An example of this could be the MLCs themselves, though their inner electrode sheets should be oriented perpendicular to the fluid flow [90, 93] instead. To prevent electrical shorts, the distance between electrode sheets (active layer) should be considerably decreased if the overall MLC thickness is not increased. The latter is not advisable because it would hinder heat transfer. Another example of these of heterogeneous structures is given in [170], where a p(VDF-TrF-CFE) solution was dripped in the nanochannels of an aluminum oxide membrane. The resulting object displayed optimal EC properties at the same time than a notably enhancement of the heat transfer thanks to the thermally conductive channels. Capillary tubes made of P(VDF-TrFE-CFE [171], with a tube wall of 80 μm and internal and external electrodes composed of Ag and carbon nanowires network respectively, constitute another promising approach to enhance heat transfer. The authors reported temperature changes of 3.53 K and a maximum cooling power density of 7021.1 mW cm^{-3} when silicone oil was continuously flowing through the tube.

The second point relates to the obvious fact that higher EC effects lead to better cooling performances, as already commented in paragraphs above. In 2019, a temperature span of 5.5 K was directly measured with IR-imaging in the active area of similar PST-MLCs (though better B-site ordered $S = 0.9$) under a supercritical field of 290 kV cm^{-1}. Despite the large adiabatic temperature change reported, these high electric fields are not viable to be applied in actuators today since a lot of samples would undergo electrical breakdown. Therefore, it would be interesting to see that future works find solutions to increase the breakdown field of these samples so that this supercritical regime could be safely applied in the operation of EC heat pumps. Recently, the creation of covalent double bonds in poly(vinylidene fluoride-trifluoroethylene-chlorofluoroethylene) terpolymer has shown very promising prospects, exhibiting temperature changes of 7.5 K under 500 kV cm^{-1} [59], which represents only 20% of its breakdown field. In addition, the authors did not observe degradation of the EC properties after 62×10^3 cycles.

The last point referred to the utilization of water as a heat transfer fluid, which has been identified as one of the main reasons behind the superior performances of magnetocaloric and elastocaloric heat pumps in comparison to electrocaloric ones. Unfortunately, water cannot be directly used in EC devices unless electric insulation of the electrode terminals is provided. The main challenge this entails is finding an electrical insulator that 1) screens the applied voltage, 2) can be properly applied on the entire electrode terminals, and 3) does not compromise heat transfer. The latter requires that this electrical insulator should (i) have a negligible thermal mass, and (ii) be preferably a good thermal conductor. Examples of this could be for instance coating the electrode terminals with a flexible insulator that is a few microns thick. Another possibility would be “hiding” one of the electrode terminals inside the EC material itself, similarly to what has been done in [112], where the EC material was grown on a wire rod and the second electrode was deposited at the final outer surface.

Chapter 5 investigated the heat transfer coefficient of caloric heat pumps, particularly of those that operated heat regenerative cycles thanks to the oscillatory circulation of a heat transfer fluid. The heat transfer coefficient was defined first by merging existing expressions in the literature, and computed secondly after a deep and thorough analysis of more than 50 caloric prototypes. By inserting their experimental data (such as operational parameters, but also physical properties and geometrical dimensions) into the described equations, the resulting heat transfer coefficient was compared to their experimental performance. Despite the evident dispersion, a linear correlation was drawn between their regeneration factor, i.e., how much larger the temperature span is in respect to the adiabatic temperature change of the material, and the calculated heat transfer coefficient. A linear regression fit was applied to quantify this correlation, reporting a slope of 6×10^{-4} m^2 K W^{-1}.

The trend observed confirmed the expected assumption that, the larger the heat transfer, the better the performance of a heat pump. This holds true for active regenerators as well, in which heat transfer should display an anisotropic profile, as already commented above. The results obtained underline the need for future caloric heat pumps to pay more attention to the heat transfer coefficient of their designs. In addition, they suggest that magnetocaloric and electrocaloric heat pumps (with typical adiabatic temperature changes of $2 - 3$ K) should have heat transfer coefficients $h_{eff} \geq 10000$ W m^{-2} K^{-1} in order to reach the performances that actual cooling applications require ($\Delta T_{span} \geq 20$ K [95]). Moreover, these results permit to assess more efficiently what the design of a certain heat pump should be in order to reach a targeted performance. This could be done by previous calculation of the heat transfer coefficient (and thus its expected regenerator factor), before carrying on the construction and experimental characterization of the heat pump.

Chapter 6 studied the capabilities of bespoke PST-MLCs in converting heat into electrical energy by means of their pyroelectric effect. The work performed was inspired by Olsen's original studies from 1980 and the well-known reasoning that materials displaying large EC effects must display large pyroelectric coefficients as well. The harvested energy density of PST-MLCs was first characterized as a function of the temperature span and electric field applied. Secondly, three harvesters were built and characterized following the same design as described in Chapter 4. The main results obtained were:

- a maximum energy density of 4.4 J cm^{-3} when undergoing Olsen cycles between 5 and 180 °C under the applied field of 195 kV cm^{-1} (750 V);
- 11.2 J of harvested electrical energy per cycle in a harvester made of 180 PST-MLCs that underwent Olsen cycles between 10 and 100 °C under the applied field of 132 kV cm^{-1} (500 V);
- a maximum electrical power of 1.95 mW per MLC when undergoing Olsen cycles between 10 and 130 °C and applied field of 195 kV cm^{-1} (750 V).

Furthermore, numerical analyses were carried out by means of finite element simulations on the heat transfer and fluid dynamics of these devices. The models were used to envision new design configurations for higher cycle frequencies, and hence, higher electrical power. These analyses stressed the need 1) to decrease the PST-MLC thickness for better heat exchange, 2) to utilize water as a heat transfer fluid and 3) to promote the parallel connection between MLCs and fluid (for instance, by increasing the number of rows of the PP-matrix while reducing the number of columns) to reduce the thermalization time.

In summary, the work presented in this dissertation represents an important step towards the industrial development of EC applications because it has been shown that coolers based on EC effects can indeed reach temperature spans larger than 10 K. More specifically, this dissertation provided new insights on the design and modelling of future EC coolers and highlighted the need to pay more attention to their heat transfer coefficient. It also revisited

Olsen's prior work on operating the reverse effect (pyroelectric effect) to produce electricity from oscillating temperature variations in time. The results reported are well beyond the state-of-the-art in both fields and should encourage the development of actual applications in the years to come.

Appendix A

Supplementary

Table A.1 **Parameters of the experimental design REG1.**

Element	Thickness (mm)	Length (mm)	Witdth (mm)
PST-MLC	0.9	7.2	10.4
Fluid slit	0.5	21.6	10.4
Regenerator	7.5	21.6	10.4

# PST-MLC columns	3
# PST-MLC rows	5
# fluid slits	6
Volume PST (mm^3)	1011
Volume fluid (mm^3)	674
Fluid cross-section (mm^2)	31.2
ΔT_{EC}	2.2
$t_{charging}$	0.4
Period τ (s)	12
Fluid flow (mL min^{-1})	25
Voltage (V)	600
Current (mA)	20
v^*	3.7

Table A.2 **Parameters of the modelling of REG1 that matched the experimental data.**

Element	Thickness (mm)	Length (mm)
PST-MLC	0.9	7.2
Fluid slit	0.5	21.6
Nylon frame	6	500
Regenerator	6.1	21.6
PT circle diameter (mm)	1.6	
# PST-MLC columns	3	
# PST-MLC rows	5	
# fluid slits	6	
$\Delta T_{EC,sim}$	$0.8\Delta T_{EC,exp}$	
$t_{charging}$	0.4	
Period τ (s)	12	
Fluid flow (mm^{2}s^{-1}	40	
v^*	3.7	

Table A.3 **Parameters of the experimental design REG2.**

Element	Thickness (mm)	Length (mm)	Width (mm)
PST-MLC	0.5	7.2	10.4
Fluid slit	0.25	115.2	10.4
Regenerator	6.25	115.2	10.4
# PST-MLC columns	16		
# PST-MLC rows	8		
# fluid slits	9		
Volume PST (mm^3)	4792.32		
Volume fluid (mm^3)	2695.68		
Fluid cross-section (mm^2)	23.4		
ΔT_{EC}	2.2		
Period τ (s)	8		
Fluid flow (mLmin^{-1})	25		
Voltage (V)	600		
Current (mA)	20		
v^*	0.62		

Table A.4 **Parameters of the modelling of REG2 that matched the experimental data.**

Element	Thickness (mm)	Length (mm)
PST-MLC	0.5	7.2
Fluid slit	0.25	115.2 Regenerator
6.25	115.2	
# PST-MLC columns	16	
# PST-MLC rows	8	
# fluid slits	9	
$\Delta T_{EC,sim}$	$0.6\Delta T_{EC,exp}$	
$t_{charging}$	1.1	
Period τ (s)	8	
Fluid flow (mm^{2}s^{-1})	40	
v^*	0.62	

Table A.5 **Parameters of the experimental design REG3.**

Element	Thickness (mm)	Length (mm)	Width (mm)
PST-MLC	0.9	7.2	10.4
Fluid slit	0.5	57.6	10.4
Regenerator	6.1	57.6	10.4
# PST-MLC columns	8		
# PST-MLC rows	4		
# fluid slits	5		
Volume PST (mm^3)	2156.54		
Volume fluid (mm^3)	1495.68		
Fluid cross-section (mm^2)	26		
ΔT_{EC}	1.3		
Period τ (s)	12		
Fluid flow (mLmin^{-1})	10.5		
Voltage (V)	150		
Current (mA)	10		
v^*	0.7		

Table A.6 **Parameters of the modelling of REG3 that matched the experimental data.**

Element	Thickness (mm)	Length (mm)
PST-MLC	0.9	7.2
Fluid slit	0.16	57.6
Regenerator	6.1	57.6
# PST-MLC columns	8	
# PST-MLC rows	4	
# fluid slits	5	
$\Delta T_{EC,sim}$	0.6 $\Delta T_{EC,exp}$	
$t_{charging}$	0.8	
Period τ (s)	12	
Fluid flow (mm^{2}s^{-1})	17	
v^*	0.7	

Table A.7 **Parameters of the modelling with 0.3 mm thick PST-MLCs exhibiting 5.5 K adiabatic temperature change and with water as heat exchange fluid.**

Element	Thickness (mm)	Length (mm)
PST-MLC	0.3	7.2
Fluid slit	0.5	57.6
Regenerator	5.76	57.6
# PST-MLC columns	8	
# PST-MLC rows	12	
# fluid slits	13	
$\Delta T_{EC,sim}$	$0.6\Delta T_{EC,exp}$	
$t_{charging}$	0.2	
Period τ (s)	1.5	
Fluid flow ($\mathrm{mm^2s^{-1}}$)	96	
v^*	0.58	

Table A.8 **Parameters of the modelling with 0.2 mm thick PST-MLCs exhibiting 5.5 K adiabatic temperature change and with water as heat exchange fluid.**

Element	Thickness (mm)	Length (mm)
PST-MLC	0.2	7.2
Fluid slit	0.5	57.6
Regenerator	5.5	57.6
# PST-MLC columns	8	
# PST-MLC rows	18	
# fluid slits	19	
$\Delta T_{EC,sim}$	$0.6\Delta T_{EC,exp}$	
$t_{charging}$	0.12	
Period τ (s)	1	
Fluid flow (mm^{2}s^{-1})	144	
v^*	0.66	

Table A.9 **Parameters of the experimental design HARV1.**

Element	Thickness (mm)	Length (mm)	Witdth (mm)
PST-MLC	0.9	7.2	10.4
Fluid slit	1	50.4	10.4
Harvester	9	50.4	10.4
# PST-MLC columns	7		
# PST-MLC rows	4		
# fluid slits	5		
Period τ (s)	52		
Thermalisation time (s) τ (s)	26.5		
Waiting time (s) τ (s)	2		
Fluid flow (mLmin^{-1})	112		
Voltage (V)	300-750		
Current (mA)	0-20		
Power (mW)	54		

Table A.10 **Parameters of the model that match HARV1 experimental performance.**

Element	Thickness (mm)	Length (mm)
PST-MLC	0.9	7.2
Fluid slit	1	50.4
Harvester	9	50.4
# PST-MLC columns	7	
# PST-MLC rows	4	
# fluid slits	5	
Period τ (s)	54.4	
Thermalisation time (s)	25.2	
Waiting time (s)	2	
Fluid flow (mm^{2}s^{-1}	112	
Power (mW)	57	

Appendix B

Publication list

Papers

(First-author contributions)

- **A. Torello**, P. Lheritier, T. Usui, Y. Nouchokgwe, M. Gerard, O. Bouton, S. Hirose, E. Defay, "*Giant temperature span in an electrocaloric regenerator*", Science, Vol 370, Issue 6512, 2020. [5]
- **A. Torello**, E. Defay, "*Heat transfer law in caloric regenerators*", International Journal of Refrigeration, Vol. 127, 2021.
- **A. Torello**, E. Defay, "*Electrocaloric coolers: a review*", Advanced Electronic Materials, 2022, 2101031.
- P. Lheritier*, **A. Torello***, T. Usui, Y. Nouchokgwe, A. Aravindhan, J. Li, U. Prah, V. Kovacova, O. Bouton, S. Hirose, E. Defay, "*A 10-Joule pyroelectric harvester*", Under Review. * These authors contributed equally.

(Co-author contributions)

- R. Faye, T. Usui, **A. Torello**, B. Dkhil, X. Moya, N. D. Mathur, S. Hirose and E. Defay, "*Heat flow in electrocaloric multilayer capacitors*", Journal of Alloys and Compounds, vol. 834, pp. 155042, 2020.
- Y. Nouchokgwe, P. Lheritier, C. Hong, **A. Torello**, R. Faye, W. Jo, C.R.H. Bahl and E. Defay, "*Giant electrocaloric materials energy efficiency in highly ordered lead scandium tantalate*", Nature Communications, vol. 12 (1), pp. 1-7, 2021.
- P. Lheritier, Y. Nouchokgwe, V. Kovacova, C. Hong, **A. Torello**, W. Jo and E. Defay, "*Measuring lead scandium tantalate phase transition entropy by infrared camera*", Journal of the European Ceramic Society, vol. 41, pp. 7000-7004, 2021.
- Y. Nouchokgwe, P. Lheritier, C. Hong, **A. Torello**, S. Hirose and E. Defay, "*Materials efficiency of PST-MLCs*", Under review
- A. Aravindhan, P. Lheritier, F. D. Dos Santos, X. Chevalier, Y. Nouchokgwe, **A. Torello**, U. Prah, A. El Moul, E. Defay, V. Kovacova, "*Direct measurement of electrocaloric effect in P(VDF-TrFE-CFE) film using infrared imaging*", Submitted

Patents

- E. Defay, M. Gerard, **A. Torello**, "*Electro-caloric and/or pyroelectric heat exchanger with an improved housing*", LU Patent WO/2021/123460, filed February 19, 2021, and issued June 24, 2021.

Book chapters

- **A. Torello**, E. Defay, “*Basics of design and modelling of regenerative electrocaloric coolers*”, The electrocaloric effect, edited by Andrei L. Kholkin, Elsevier, 2022.

Conferences

- *"Predictive modelling of electrocaloric heat exchangers"* (**Oral presentation**) at the Material Research Society (MRS) fall exhibition, Boston, USA (2019).
- *"Experimental improvement of Electrocaloric heat exchangers by guidance of numerical modelling"* (**Oral presentation**) at the International Symposium of Applications of Ferroelectrics (ISAF), Lausanne, Switzerland (2019).
- "*Development of an electrocaloric cooling device*" (**Poster presentation**) at the International School of Oxide Electronics (ISOE), Cargese, France (2019).
- *"Experimental improvement of Electrocaloric heat exchangers by guidance of numerical modelling"*" (**Oral presentation**) at the European Material Research Society (E-MRS), Warsow, Poland (2019).
- "*Giant temperature span in EC regenerator*" (**Oral presentation**) at the Material Research Society (E-MRS) spring exhibition. Virtual (2020).
- "*Giant temperature span in EC regenerator*" (**Poster**) at MASSENA Young Scientist Conference, Bourscheid, Luxembourg (2021).
- *"Electrocaloric cooling, a plausible alternative to vapour compression systems?"* (**Poster presentation**), in the International Symposium of Applications of Ferroelectrics (ISAF), Tours, France (2022).

Awards

- **Student Pitch Industry’s Choice Award Winner** at the International Symposium of Applications of Ferroelectrics (ISAF), Lausanne, Switzerland (2019).
- **Graduate Student Award** at the European Material Research Society (E-MRS), Warsow, Poland (2019).
- **Outstanding Scientific Achievement** at the Luxembourg National Research Fund (FNR) awards ceremony, Belval, Luxembourg (2021).

References

[1] B. Nair, Electrocaloric applications based on multilayer capacitors of $PbSc_{0.5}Ta_{0.5}O_3$, Phd thesis, University of Cambridge, 2020.

[2] D. Guo, J. Gao, Y. J. Yu, S. Santhanam, A. Slippey, G. K. Fedder, A. J. McGaughey, S. C. Yao, Design and modeling of a fluid-based micro-scale electrocaloric refrigeration system, International Journal of Heat and Mass Transfer 72 (2014) 559–564. URL: http://dx.doi.org/10.1016/j.ijheatmasstransfer.2014.01.043. doi:10.1016/j.ijheatmasstransfer.2014.01.043.

[3] J. Shi, Q. Li, T. Gao, D. Han, Y. Li, J. Chen, X. Qian, Numerical evaluation of a kilowatt-level rotary electrocaloric refrigeration system, International Journal of Refrigeration 121 (2021) 279–288. URL: https://www.sciencedirect.com/science/article/pii/S0140700720303832. doi:https://doi.org/10.1016/j.ijrefrig.2020.09.011.

[4] H. Gu, X. Qian, H. Ye, Q. M. Zhang, An electrocaloric refrigerator without external regenerator, Applied Physics Letters 105 (2014) 162905. URL: https://doi.org/10.1063/1.4898812. doi:10.1063/1.4898812.

[5] A. Torelló, P. Lheritier, T. Usui, Y. Nouchokgwe, M. Gérard, O. Bouton, S. Hirose, E. Defay, Giant temperature span in electrocaloric regenerator, Science 370 (2020) 125–129. URL: http://science.sciencemag.org/.

[6] Y. V. Sinyavsky, G. E. Lugansky, N. D. Pashkov, Electrocaloric refrigeration: Investigation of a model and prognosis of mass and efficiency indexes, Cryogenics 32 (1992) 28–31. doi:10.1016/0011-2275(92)90102-G.

[7] U. Plaznik, A. Kitanovski, B. Rǒič, B. Malič, H. Uršič, S. Drnovšek, J. Cilenšek, M. Vrabelj, A. Poredoš, Z. Kutnjak, Bulk relaxor ferroelectric ceramics as a working body for an electrocaloric cooling device, Applied Physics Letters 106 (2015). doi:10.1063/1.4907258.

[8] P. Blumenthal, A. Raatz, Design Methodology for Electrocaloric Cooling Systems, Energy Technology 6 (2018) 1560–1566. doi:10.1002/ente.201800139.

[9] R. Ma, Z. Zhang, K. Tong, D. Huber, R. Kornbluh, Y. S. Ju, Q. Pei, Highly efficient electrocaloric cooling with electrostatic actuation, Science 357 (2017) 1130–1134. doi:10.1126/science.aan5980.

[10] A. Kitanovski, J. Tušek, U. Tomc, U. Plaznik, M. Ožbolt, A. Poredoš, Magnetocaloric energy conversion - From theory to applications, 2015.

[11] P. Kosky, R. Balmer, W. Keat, G. Wise, Chapter 14 - Mechanical Engineering, in: Exploring Engineering (Fifth Edition), Academic Press, 2021, pp. 317–340. URL: https://www.

sciencedirect.com/science/article/pii/B9780128150733000144. doi:https://doi.org/10.1016/B978-0-12-815073-3.00014-4.

[12] B. Nair, T. Usui, S. Crossley, S. Kurdi, G. G. Guzmán-Verri, X. Moya, S. Hirose, N. D. Mathur, Large electrocaloric effects in oxide multilayer capacitors over a wide temperature range, Nature 575 (2019) 468–472. URL: http://dx.doi.org/10.1038/s41586-019-1634-0. doi:10.1038/s41586-019-1634-0.

[13] OECD, Ghg emissions from fuel combustion (summary) (2021). URL: https://www.oecd-ilibrary.org/content/data/445ec5dd-en. doi:https://doi.org/https://doi.org/10.1787/445ec5dd-en.

[14] NASA, What is the greenhouse effect?, 2022. URL: https://climate.nasa.gov/faq/19/what-is-the-greenhouse-effect/.

[15] EPA, Overview of greenhouse gases, 2022. URL: https://www.epa.gov/ghgemissions/overview-greenhouse-gases.

[16] U. E. P. Agency, Understanding global warming potentials, 2022. URL: https://www.epa.gov/ghgemissions/understanding-global-warming-potentials.

[17] N. Earth Observatory, World of change: Global temperatures, 2021. URL: https://earthobservatory.nasa.gov/world-of-change/global-temperatures.

[18] Selectra, Global warming in 2022: causes and consequences, 2022. URL: https://climate.selectra.com/en/environment/global-warming.

[19] U. Nations, Paris agreement, 2015. URL: https://unfccc.int/sites/default/files/english_paris_agreement.pdf.

[20] U. N. E. Programme, I. E. Agency, Cooling emissions and policy synthesis report, 2020. URL: https://iea.blob.core.windows.net/assets/71c8db7e-1137-41ef-99c3-8f2c8d3a5d86/Cooling_Emissions_and_Policy_Synthesis_Report.pdf.

[21] UNIDO, Mapping the HFC phase-down, 2017. URL: https://www.unido.org/sites/default/files/files/2020-04/UNIDO-brochure_HFC-Phase_Down-Complete.pdf.

[22] J. Tušek, K. Engelbrecht, D. Eriksen, S. Dall'Olio, J. Tušek, N. Pryds, A regenerative elastocaloric heat pump, Nature Energy 1 (2016) 1–6. doi:10.1038/nenergy.2016.134.

[23] P. Lloveras, A. Aznar, M. Barrio, P. Negrier, C. Popescu, A. Planes, L. Mañosa, E. Stern-Taulats, A. Avramenko, N. D. Mathur, X. Moya, J. L. Tamarit, Colossal barocaloric effects near room temperature in plastic crystals of neopentylglycol, Nature Communications 10 (2019) 1–7. URL: http://dx.doi.org/10.1038/s41467-019-09730-9. doi:10.1038/s41467-019-09730-9. arXiv:1903.12010.

[24] B. Li, Y. Kawakita, S. Ohira-Kawamura, T. Sugahara, H. Wang, J. Wang, Y. Chen, S. I. Kawaguchi, S. Kawaguchi, K. Ohara, K. Li, D. Yu, R. Mole, T. Hattori, T. Kikuchi, S. ichiro Yano, Z. Zhang, Z. Zhang, W. Ren, S. Lin, O. Sakata, K. Nakajima, Z. Zhang, Colossal barocaloric effects in plastic crystals, Nature 567 (2019) 506–510. URL: http://dx.doi.org/10.1038/s41586-019-1042-5. doi:10.1038/s41586-019-1042-5.

[25] Y. Wang, Z. Zhang, T. Usui, M. Benedict, S. Hirose, J. Lee, J. Kalb, D. Schwartz, A high-performance solid-state electrocaloric cooling system, Science 370 (2020) 129–133.

[26] Y. Meng, Z. Zhang, H. Wu, R. Wu, J. Wu, H. Wang, Q. Pei, A cascade electrocaloric cooling device for large temperature lift, Nature Energy 5 (2020) 996–1002. URL: http://dx.doi.org/10.1038/s41560-020-00715-3. doi:10.1038/s41560-020-00715-3.

[27] X. Moya, N. D. Mathur, Caloric materials for cooling and heating, Science 370 (2020) 797–803.

[28] S. Fähler, U. K. Rößler, O. Kastner, J. Eckert, G. Eggeler, H. Emmerich, P. Entel, S. Müller, E. Quandt, K. Albe, Caloric effects in ferroic materials: New concepts for cooling, Advanced Engineering Materials 14 (2012) 10–19. doi:10.1002/adem.201100178.

[29] L. Mañosa, A. Planes, M. Acet, Advanced materials for solid-state refrigeration, Journal of Materials Chemistry A 1 (2013) 4925–4936. doi:10.1039/c3ta01289a.

[30] X. Moya, S. Kar-Narayan, N. D. Mathur, Caloric materials near ferroic phase transitions, Nature Materials 13 (2014) 439–450. URL: http://dx.doi.org/10.1038/nmat3951. doi:10.1038/nmat3951.

[31] M. Ožbolt, A. Kitanovski, J. Tušek, A. Poredoš, Electrocaloric refrigeration: Thermodynamics, state of the art and future perspectives, International Journal of Refrigeration 40 (2014) 174–188. URL: https://www.sciencedirect.com/science/article/pii/S0140700713002995. doi:https://doi.org/10.1016/j.ijrefrig.2013.11.007.

[32] J. Shi, D. Han, Z. Li, L. Yang, S. G. Lu, Z. Zhong, J. Chen, Q. M. Zhang, X. Qian, Electrocaloric Cooling Materials and Devices for Zero-Global-Warming-Potential, High-Efficiency Refrigeration, Joule 3 (2019) 1200–1225. URL: https://doi.org/10.1016/j.joule.2019.03.021. doi:10.1016/j.joule.2019.03.021.

[33] X. Moya, E. Defay, V. Heine, N. D. Mathur, Too cool to work, Nature Physics 11 (2015) 202–205. URL: http://dx.doi.org/10.1038/nphys3271. doi:10.1038/nphys3271.

[34] B. Yu, M. Liu, P. W. Egolf, A. Kitanovski, A review of magnetic refrigerator and heat pump prototypes built before the year 2010, International Journal of Refrigeration 33 (2010) 1029–1060. URL: http://dx.doi.org/10.1016/j.ijrefrig.2010.04.002. doi:10.1016/j.ijrefrig.2010.04.002.

[35] G. V. Brown, Magnetic heat pumping near room temperature, Journal of Applied Physics 47 (1976) 3673–3680. doi:10.1063/1.323176.

[36] C. R. Bahl, K. Engelbrecht, D. Eriksen, J. A. Lozano, R. Bjørk, J. Geyti, K. K. Nielsen, A. Smith, N. Pryds, Development and experimental results from a 1 kW prototype AMR, International Journal of Refrigeration 37 (2014) 78–83. URL: http://dx.doi.org/10.1016/j.ijrefrig.2013.09.001. doi:10.1016/j.ijrefrig.2013.09.001.

[37] S. Jacobs, J. Auringer, A. Boeder, J. Chell, L. Komorowski, J. Leonard, S. Russek, C. Zimm, The performance of a large-scale rotary magnetic refrigerator, International Journal of Refrigeration 37 (2014) 84–91. URL: http://dx.doi.org/10.1016/j.ijrefrig.2013.09.025. doi:10.1016/j.ijrefrig.2013.09.025.

[38] E. Pieczyska, S. Gadaj, W. Nowacki, H. Tobushi, Phase-transformation fronts evolution for stress- and strain-controlled tension tests in tini shape memory alloy, Exp. Mech. 46 (2006) 531–542.

[39] J. Tušek, K. Engelbrecht, L. P. Mikkelsen, N. Pryds, Elastocaloric effect of ni-ti wire for application in a cooling device, Journal of Applied Physics

117 (2015) 124901. URL: https://doi.org/10.1063/1.4913878. doi:10.1063/1.4913878. arXiv:https://doi.org/10.1063/1.4913878.

[40] D. Cong, W. Xiong, A. Planes, Y. Ren, L. Mañosa, P. Cao, Z. Nie, X. Sun, Z. Yang, X. Hong, Y. Wang, Colossal elastocaloric effect in ferroelastic ni-mn-ti alloys, Phys. Rev. Lett. 122 (2019) 255703. URL: https://link.aps.org/doi/10.1103/PhysRevLett.122.255703. doi:10.1103/PhysRevLett.122.255703.

[41] L. Mañosa, A. Planes, J. Ortín, B. Martínez, Entropy change of martensitic transformations in cu-based shape-memory alloys, Phys. Rev. B 48 (1993) 3611–3619. URL: https://link.aps.org/doi/10.1103/PhysRevB.48.3611. doi:10.1103/PhysRevB.48.3611.

[42] E. Bonnot, R. Romero, L. Mañosa, E. Vives, A. Planes, Elastocaloric effect associated with the martensitic transition in shape-memory alloys, Phys. Rev. Lett. 100 (2008) 125901. URL: https://link.aps.org/doi/10.1103/PhysRevLett.100.125901. doi:10.1103/PhysRevLett.100.125901.

[43] S. Qian, Y. Geng, Y. Wang, J. Ling, Y. Hwang, R. Radermacher, I. Takeuchi, J. Cui, A review of elastocaloric cooling: Materials, cycles and system integrations, International Journal of Refrigeration 64 (2016) 1–19. URL: https://www.sciencedirect.com/science/article/pii/S0140700715003783. doi:https://doi.org/10.1016/j.ijrefrig.2015.12.001.

[44] R. Snodgrass, D. Erickson, A multistage elastocaloric refrigerator and heat pump with 28 K temperature span, Scientific Reports 9 (2019) 1–10. doi:10.1038/s41598-019-54411-8.

[45] M. O. McLinden, Thermophysical properties of refrigerants, Handbook: Fundamentals, ASHRAE, Atlanta, 2009.

[46] M. Romanini, Y. Wang, K. Gürpinar, G. Ornelas, P. Lloveras, Y. Zhang, W. Zheng, M. Barrio, A. Aznar, A. Gràcia-Condal, B. Emre, O. Atakol, C. Popescu, H. Zhang, Y. Long, L. Balicas, J. Lluís Tamarit, A. Planes, M. Shatruk, L. Mañosa, Giant and reversible barocaloric effect in trinuclear spin-crossover complex $Fe_3(bntrz)_6(tcnset)_6$, Advanced Materials 33 (2021) 2008076. URL: https://onlinelibrary.wiley.com/doi/abs/10.1002/adma.202008076. doi:https://doi.org/10.1002/adma.202008076. arXiv:https://onlinelibrary.wiley.com/doi/pdf/10.1002/adma.202008076.

[47] P. Vales-Castro, R. Faye, M. Vellvehi, Y. Nouchokgwe, X. Perpiñà, J. M. Caicedo, X. Jordà, K. Roleder, D. Kajewski, A. Perez-Tomas, E. Defay, G. Catalan, Origin of large negative electrocaloric effect in antiferroelectric $PbZrO_3$, Phys. Rev. B 103 (2021) 54112. URL: https://link.aps.org/doi/10.1103/PhysRevB.103.054112. doi:10.1103/PhysRevB.103.054112.

[48] R. Pirc, B. Rožič, J. Koruza, B. Malič, Z. Kutnjak, Negative electrocaloric effect in antiferroelectric $PbZrO_3$, EPL (Europhysics Letters) 107 (2014) 17002. URL: https://doi.org/10.1209/0295-5075/107/17002. doi:10.1209/0295-5075/107/17002.

[49] N. Novak, F. Weyland, S. Patel, H. Guo, X. Tan, J. Rödel, J. Koruza, Interplay of conventional with inverse electrocaloric response in $(Pb, Nb)(Zr, Sn, Ti)O_3$ antiferroelectric materials, Phys. Rev. B 97 (2018) 94113. URL: https://link.aps.org/doi/10.1103/PhysRevB.97.094113. doi:10.1103/PhysRevB.97.094113.

[50] E. Defay, R. Faye, G. Despesse, H. Strozyk, D. Sette, S. Crossley, X. Moya, N. D. Mathur,

Enhanced electrocaloric efficiency via energy recovery, Nature Communications 9 (2018). doi:10.1038/s41467-018-04027-9.

[51] P. Kobeko, J. Kurtschatov, Dielektrische Eigenschaften der Seignettesalzkristalle, Z. Phys. 66 (1930) 192–205.

[52] H. Baumgartner, Elektrische Sättigungserscheinungen und elektrokalorischer Effekt von Kaliumphosphat KH_2PO_4, Helv. Phys. Acta 23 (1950) 651–696.

[53] G. Lombardo, R. O. Pohl, Electrocaloric effect and a new type of impurity mode, Phys. Rev. Lett. 15 (1965) 291–293.

[54] A. I. Karchevskii, Electrocaloric effect in polycrystalline barium titanate, Phys. Solid State 3 (1962) 2249–2254.

[55] P. D. Thacher, Electrocaloric effects in some ferroelectric and antiferroelectric $Pb(Zr,Ti)O_3$ compounds., J. Appl. Phys. 39 (1968) 1996–2002.

[56] B. A. Tuttle, D. A. Payne, The effects of microstructure on the electrocaloric properties of $Pb(Zr,Sn,Ti)O_3$ ceramics, Ferroelectrics 37 (1981) 603–606.

[57] A. S. Mischenko, Q. Zhang, J. F. Scott, R. W. Whatmore, N. D. Mathur, Giant electrocaloric effect in thin-film $PbZr_{0.95}Ti_{0.05}O_3$, Science 311 (2006) 1270–1271. doi:10.1126/science.1123811. arXiv:0511487.

[58] B. Neese, B. Chu, S. G. Lu, Y. Wang, E. Furman, Q. M. Zhang, Large electrocaloric effect in ferroelectric polymers near room temperature, Science 321 (2008) 821–823. doi:10.1126/science.1159655.

[59] X. Qian, D. Han, L. Zheng, J. Chen, M. Tyagi, Q. Li, F. Du, S. Zheng, X. Huang, S. Zhang, J. Shi, H. Huang, X. Shi, J. Chen, H. Qin, J. Bernholc, X. Chen, L.-Q. Chen, L. Hong, Q. M. Zhang, High-entropy polymer produces a giant electrocaloric effect at low fields, Nature 600 (2021) 664–669. URL: https://doi.org/10.1038/s41586-021-04189-5. doi:10.1038/s41586-021-04189-5.

[60] Y. V. Sinyavsky, N. D. Pashkov, Y. M. Gorovoy, G. E. Lugansky, L. Shebanov, The Optical Ferroelectric Ceramic As Working Body For Electrocaloric Refrigeration, Ferroelectrics 90 (1989) 213–217. doi:10.1080/00150198908211296.

[61] Y. V. Sinyavskii, Electrocaloric refrigerators: A promising alternative to current low-temperature apparatus, Chemical and Petroleum Engineering 31 (1995) 295–306. doi:10.1007/BF01148217.

[62] Y. Jia, Y. Sungtaek Ju, A solid-state refrigerator based on the electrocaloric effect, Applied Physics Letters 100 (2012). doi:10.1063/1.4729038.

[63] S. Kar-Narayan, N. D. Mathur, Direct and indirect electrocaloric measurements using multilayer capacitors, Journal of Physics D: Applied Physics 43 (2010) 3–7. doi:10.1088/0022-3727/43/3/032002.

[64] H. Gu, X. Qian, X. Li, B. Craven, W. Zhu, A. Cheng, S. C. Yao, Q. M. Zhang, A chip scale electrocaloric effect based cooling device, Applied Physics Letters 102 (2013) 3–6. doi:10.1063/1.4799283.

[65] U. Plaznik, M. Vrabelj, Z. Kutnjak, B. Malič, B. Rožič, A. Poredoš, A. Kitanovski, Numerical modelling and experimental validation of a regenerative electrocaloric cooler, International Journal of Refrigeration 98 (2019) 139–149. doi:10.1016/j.ijrefrig.2018.10.029.

[66] Y. D. Wang, S. J. Smullin, M. J. Sheridan, Q. Wang, C. Eldershaw, D. E. Schwartz, A heat-switch-based electrocaloric cooler, Applied Physics Letters 107 (2015). URL: http://dx.doi.org/10.1063/1.4932164. doi:10.1063/1.4932164.

[67] D. Sette, A. Asseman, M. Gérard, H. Strozyk, R. Faye, E. Defay, Electrocaloric cooler combining ceramic multi-layer capacitors and fluid, APL Materials 4 (2016). URL: http://dx.doi.org/10.1063/1.4961954. doi:10.1063/1.4961954.

[68] K. K. Nielsen, C. R. H. Bahl, A. Smith, R. Bjørk, N. Pryds, J. Hattel, Detailed numerical modeling of a linear parallel-plate Active Magnetic Regenerator, International Journal of Refrigeration 32 (2009) 1478–1486. URL: https://www.sciencedirect.com/science/article/pii/S0140700709000796. doi:https://doi.org/10.1016/j.ijrefrig.2009.03.003.

[69] A. Torello, E. Defay, Heat exchange law in caloric regenerators, International Journal of Refrigeration 127 (2021) 174–179. URL: https://www.sciencedirect.com/science/article/pii/S0140700721000888. doi:https://doi.org/10.1016/j.ijrefrig.2021.02.024.

[70] A. Torello, E. Defay, Electrocaloric coolers: A review, Advanced Electronic Materials (2021) 2101031.

[71] A. Torello, E. Defay, Chapter 21 - Basics of design and modelling of regenerative electrocaloric coolers, in: The electrocaloric effect (First Edition), Elsevier, 2022. URL: https://www.sciencedirect.com/science/article/pii/B9780128150733000144.

[72] G. Sebald, L. Seveyrat, J. F. Capsal, P. J. Cottinet, D. Guyomar, Differential scanning calorimeter and infrared imaging for electrocaloric characterization of poly(vinylidene fluoride-trifluoroethylene- chlorofluoroethylene) terpolymer, Applied Physics Letters 101 (2012). doi:10.1063/1.4734924.

[73] V. Basso, F. Russo, J. F. Gerard, S. Pruvost, Direct measurement of the electrocaloric effect in poly(vinylidene fluoride-trifluoroethylene-chlorotrifluoroethylene) terpolymer films, Applied Physics Letters 103 (2013). doi:10.1063/1.4830369.

[74] P. Lhéritier, Y. Nouchokgwe, V. Kovacova, C.-H. Hong, À. Torelló, W. Jo, E. Defay, Measuring lead scandium tantalate phase transition entropy by infrared camera, Journal of the European Ceramic Society (2021). URL: https://www.sciencedirect.com/science/article/pii/S0955221921004726. doi:https://doi.org/10.1016/j.jeurceramsoc.2021.07.002.

[75] Y. Nouchokgwe, P. Lheritier, C.-H. Hong, A. Torelló, R. Faye, W. Jo, C. R. H. Bahl, E. Defay, Giant electrocaloric materials energy efficiency in highly ordered lead scandium tantalate, Nature Communications 12 (2021) 1–7. URL: http://dx.doi.org/10.1038/s41467-021-23354-y. doi:10.1038/s41467-021-23354-y.

[76] G. Sebald, L. Seveyrat, D. Guyomar, L. Lebrun, B. Guiffard, G. Sebald, L. Seveyrat, D. Guyomar, L. Lebrun, B. Guiffard, S. Pruvost, Electrocaloric and pyroelectric properties of $0.75Pb(Mg_{1/3}Nb_{2/3})O_3$–$0.25PbTiO_3$ single crystals 124112 (2006) 0–6. doi:10.1063/1.2407271.

[77] X. Moya, E. Stern-Taulats, S. Crossley, D. González-Alonso, S. Kar-Narayan, A. Planes,

L. Mañosa, N. D. Mathur, Giant electrocaloric strength in single-crystal BaTiO3, Advanced Materials 25 (2013) 1360–1365. doi:10.1002/adma.201203823.

[78] X. Qian, H.-j. Ye, Y.-t. Zhang, H. Gu, X. Li, C. A. Randall, Q. M. Zhang, Giant Electrocaloric Response Over A Broad Temperature Range in Modified BaTiO3 Ceramics, Advanced Functional Materials 24 (2014) 1300–1305. doi:10.1002/adfm.201302386.

[79] M. Vrabelj, H. Uršič, Z. Kutnjak, B. Rožič, S. Drnovšek, A. Bencan, V. Bobnar, L. Fulanović, B. Malic, Large electrocaloric effect in grain-size-engineered 0.9Pb($Mg_{1/3}Nb_{2/3}$)O_3–0.1PbTiO_3, Journal of the European Ceramic Society 36 (2016) 75–80. doi:10.1016/j.jeurceramsoc.2015.09.031.

[80] Y. Bai, K. Ding, G.-p. Zheng, S.-q. Shi, L. Qiao, I. With, T. Fe, T. Ece, Entropy-change measurement of electrocaloric effect of BaTiO_3 single crystal, Phys. Status Solidi A 209 (2012) 941–944. doi:10.1002/pssa.201127695.

[81] T. M. Correia, J. S. Young, R. W. Whatmore, J. F. Scott, N. D. Mathur, Q. Zhang, Investigation of the electrocaloric effect in a Pb$Mg_{2/3}Nb_{1/3}O_3$ - PbTiO_3 relaxor thin film, Applied Physics Letters 95 (2009) 20–23. doi:10.1063/1.3257695.

[82] S. G. Lu, B. Rožič, Q. M. Zhang, Z. Kutnjak, X. Li, E. Furman, L. J. Gorny, M. Lin, B. Malič, M. Kosec, R. Blinc, R. Pirc, Organic and inorganic relaxor ferroelectrics with giant electrocaloric effect, Applied Physics Letters 97 (2010) 2–4. doi:10.1063/1.3501975.

[83] X. Li, X. S. Qian, H. Gu, X. Chen, S. G. Lu, M. Lin, F. Bateman, Q. M. Zhang, Giant electrocaloric effect in ferroelectric poly(vinylidenefluoride- trifluoroethylene) copolymers near a first-order ferroelectric transition, Applied Physics Letters 101 (2012). doi:10.1063/1.4756697.

[84] B. Peng, H. Fan, Q. Zhang, Giant Electrocaloric Effect in Nanoscale Antiferroelectric and Ferroelectric Phases Coexisting in a Relaxor Pb 0 . 8 Ba 0 . 2 ZrO 3 Thin Film at Room Temperature, Advanced Functional Materials 23 (2013) 2987–2892. doi:10.1002/adfm.201202525.

[85] H. Ye, X. Qian, D. Jeong, S. Zhang, Y. Zhou, W. Shao, L. Zhen, Giant electrocaloric effect in Ba$Zr_{0.2}Ti_{0.8}O_3$ thick film 105 (2014) 4–8. doi:10.1063/1.4898599.

[86] S. Crossley, T. Usui, B. Nair, X. Moya, S. Hirose, A. Ando, Direct electrocaloric measurement of 0.9Pb(Mg1/3Nb2/3)O3-0.1PbTiO3 films using scanning thermal microscopy, Applied Physics Letters 108 (2016) 0–5. doi:10.1063/1.4938758.

[87] Z. Kutnjak, B. Roz, Indirect and Direct Measurements of the Electrocaloric Effect, in: Electrocaloric Materials. Engineering Materials, vol 34 ed., Springer, Berlin, Heidelberg, 2014. doi:10.1007/978-3-642-40264-7.

[88] S. Pandya, J. D. Wilbur, B. Bhatia, A. R. Damodaran, A. Dasgupta, W. P. King, C. Dames, L. W. Martin, Direct Measurement of Pyroelectric and Electrocaloric Effects in Thin Films, Physical Review Applied 7 (2017). doi:10.1103/PhysRevApplied.7.034025.

[89] S. Pandya, J. Wilbur, J. Kim, R. Gao, A. Dasgupta, C. Dames, L. W. Martin, energy and power density in relaxor ferroelectric thin films, Nature Materials (2018). URL: http://dx.doi.org/10.1038/s41563-018-0059-8. doi:10.1038/s41563-018-0059-8.

[90] R. Faye, T. Usui, A. Torello, B. Dkhil, X. Moya, N. D. Mathur, S. Hirose, E. Defay, Heat

flow in electrocaloric multilayer capacitors, Journal of Alloys and Compounds 834 (2020). doi:10.1016/j.jallcom.2020.155042.

[91] T. Usui, S. Hirose, A. Ando, S. Crossley, B. Nair, X. Moya, N. D. Mathur, Effect of inactive volume on thermocouple measurements of electrocaloric temperature change in multilayer capacitors of 0.9Pb($Mg_{1/3}Nb_{2/3}$)O_3-0.1PbTiO_3, Journal of Physics D: Applied Physics 50 (2017). doi:10.1088/1361-6463/aa87a5.

[92] X. Moya, E. Defay, N. D. Mathur, S. Hirose, Electrocaloric effects in multilayer capacitors for cooling applications, MRS Bulletin 43 (2018) 291–294. doi:10.1557/mrs.2018.68.

[93] R. Faye, H. Strozyk, B. Dkhil, E. Defay, Large heat flux in electrocaloric multilayer capacitors, Journal of Physics D: Applied Physics 50 (2017). doi:10.1088/1361-6463/aa8d0f.

[94] T. Zhang, X. S. Qian, H. Gu, Y. Hou, Q. M. Zhang, An electrocaloric refrigerator with direct solid to solid regeneration, Applied Physics Letters 110 (2017) 1–5. doi:10.1063/1.4986508.

[95] Y. Meng, J. Pu, Q. Pei, Electrocaloric cooling over high device temperature span, Joule 5 (2021) 780–793. URL: https://www.sciencedirect.com/science/article/pii/S2542435120306176. doi:https://doi.org/10.1016/j.joule.2020.12.018.

[96] P. Blumenthal, A. Raatz, Classification of electrocaloric cooling device types, EPL (Europhysics Letters) 115 (2016) 17004. URL: https://doi.org/10.1209/0295-5075/115/17004. doi:10.1209/0295-5075/115/17004.

[97] K. K. Nielsen, J. Tusek, K. Engelbrecht, S. Schopfer, A. Kitanovski, C. R. Bahl, A. Smith, N. Pryds, A. Poredos, Review on numerical modeling of active magnetic regenerators for room temperature applications, International Journal of Refrigeration 34 (2011) 603–616. URL: http://dx.doi.org/10.1016/j.ijrefrig.2010.12.026. doi:10.1016/j.ijrefrig.2010.12.026.

[98] T. Gottschall, M. D. Kuz'Min, K. P. Skokov, Y. Skourski, M. Fries, O. Gutfleisch, M. G. Zavareh, D. L. Schlagel, Y. Mudryk, V. Pecharsky, J. Wosnitza, Magnetocaloric effect of gadolinium in high magnetic fields, Physical Review B 99 (2019) 1–7. doi:10.1103/PhysRevB.99.134429.

[99] K. Engelbrecht, J. Tušek, D. Eriksen, T. Lei, C. Y. Lee, J. Tušek, N. Pryds, A regenerative elastocaloric device: Experimental results, Journal of Physics D: Applied Physics 50 (2017). doi:10.1088/1361-6463/aa8656.

[100] J. Chen, L. Lei, G. Fang, Elastocaloric cooling of shape memory alloys: A review, Materials Today Communications 28 (2021) 102706. URL: https://www.sciencedirect.com/science/article/pii/S235249282100698X. doi:https://doi.org/10.1016/j.mtcomm.2021.102706.

[101] W. A. Steyert, Stirling-cycle rotating magnetic refrigerators and heat engines for use near room temperature, Journal of Applied Physics 49 (1978) 1216–1226. doi:10.1063/1.325009.

[102] J. A. Barclay, W. A. Steyert, Active magnetic regenerator, 1982. URL: https://patentimages.storage.googleapis.com/6a/12/44/22460fdd3f9faf/US4332135.pdf.

[103] A. Greco, C. Aprea, A. Maiorino, C. Masselli, A review of the state of the art of solid-state caloric cooling processes at room-temperature before 2019, Interna-

tional Journal of Refrigeration 106 (2019) 66–88. URL: https://www.sciencedirect.com/science/article/pii/S014070071930297X. doi:https://doi.org/10.1016/j.ijrefrig.2019.06.034.

[104] Y. Wang, D. E. Schwartz, S. J. Smullin, Q. Wang, M. J. Sheridan, Silicon Heat Switches for Electrocaloric Cooling, Journal of Microelectromechanical Systems 26 (2017) 580–587. doi:10.1109/JMEMS.2017.2676704.

[105] Y. Liu, J. F. Scott, B. Dkhil, Direct and indirect measurements on electrocaloric effect: Recent developments and perspectives, Applied Physics Reviews 3 (2016) 31102. URL: https://doi.org/10.1063/1.4958327. doi:10.1063/1.4958327.

[106] B. Rehm, D. Consultant, A. Haghshenas, A. S. Paknejad, J. Schubert, CHAPTER TWO - Situational Problems in MPD, in: B. Rehm, J. Schubert, A. Haghshenas, A. S. Paknejad, J. Hughes (Eds.), Managed Pressure Drilling, Gulf Publishing Company, 2008, pp. 39–80. URL: https://www.sciencedirect.com/science/article/pii/B9781933762241500085. doi:https://doi.org/10.1016/B978-1-933762-24-1.50008-5.

[107] X. Chen, X. Li, X. Qian, S. Wu, S. Lu, H. Gu, M. Lin, Q. Shen, Q. M. Zhang, A polymer blend approach to tailor the ferroelectric responses in P (VDF e TrFE) based copolymers, Polymer 54 (2013) 2373–2381. URL: http://dx.doi.org/10.1016/j.polymer.2013.02.041. doi:10.1016/j.polymer.2013.02.041.

[108] S. R. Annapragada, P. Verma, A. Sur, W. Xie, High-Efficiency Solid State Heat Pump Module, Technical Report, United Technologies Research Center (UTRC), 2018 [Online]. URL: https://www.osti.gov/servlets/purl/1456857.

[109] H. Uršič, M. Vrabelj, L. Fulanovič, A. Bradeško, S. Drnovšek, B. Malič, Specific heat capacity and thermal conductivity of the electrocaloric (1-x)Pb($Mg_{1/3}Nb_{2/3}$)O_3-xPbTiO_3 ceramics between room temperature and 300 °C, Informacije MIDEM 45 (2015) 260–265.

[110] S. R. Annapragada, P. Verna, A. Sur, W. Xie, High-Efficiency Solid State Heat Pump Module, Technical Report, United Technologies Research Center (UTRC), 2017.

[111] A. Bradeško, L. Fulanović, M. Vrabelj, A. Matavž, M. Otoničar, J. Koruza, B. Malič, T. Rojac, Multifunctional cantilevers as working elements in solid-state cooling devices, Actuators 10 (2021) 1–13. doi:10.3390/act10030058.

[112] H. Wang, Y. Meng, Z. Zhang, M. Gao, Z. Peng, H. He, Self-Actuating Electrocaloric Cooling Fibers 1903902 (2020) 1–6. doi:10.1002/aenm.201903902.

[113] A. Bradeško, D. Juričić, M. Santo Zarnik, B. Malič, Z. Kutnjak, T. Rojac, Coupling of the electrocaloric and electromechanical effects for solid-state refrigeration, Applied Physics Letters 109 (2016). URL: http://dx.doi.org/10.1063/1.4964124. doi:10.1063/1.4964124.

[114] Q. Li, J. Shi, D. Han, F. Du, J. Chen, X. Qian, Concept design and numerical evaluation of a highly efficient rotary electrocaloric refrigeration device, Applied Thermal Engineering 190 (2021) 116806. URL: https://www.sciencedirect.com/science/article/pii/S135943112100257X. doi:https://doi.org/10.1016/j.applthermaleng.2021.116806.

[115] S. J. Smullin, Y. Wang, D. E. Schwartz, System optimization of a heat-switch-based

electrocaloric heat pump, Applied Physics Letters 107 (2015) 93903. URL: https://doi.org/10.1063/1.4928716. doi:10.1063/1.4928716.

[116] C. Aprea, A. Greco, A. Maiorino, C. Masselli, A comparison between different materials in an active electrocaloric regenerative cycle with a 2D numerical model, International Journal of Refrigeration 69 (2016) 369–382. URL: https://www.sciencedirect.com/science/article/pii/S0140700716301803. doi:https://doi.org/10.1016/j.ijrefrig.2016.06.016.

[117] C. Aprea, A. Maiorino, I. Andri, J. Ii, A two-dimensional model of a solid-state regenerator based on combined electrocaloric-elastocaloric effect, Energy Procedia 126 (2017) 337–344. URL: https://doi.org/10.1016/j.egypro.2017.08.225. doi:10.1016/j.egypro.2017.08.225.

[118] C. Aprea, A. Greco, A. Maiorino, C. Masselli, Solid-state refrigeration: A comparison of the energy performances of caloric materials operating in an active caloric regenerator, Energy 165 (2018) 439–455. URL: https://www.sciencedirect.com/science/article/pii/S0360544218318784. doi:https://doi.org/10.1016/j.energy.2018.09.114.

[119] C. Aprea, A. Greco, A. Maiorino, C. Masselli, The employment of caloric-effect materials for solid-state heat pumping, International Journal of Refrigeration 109 (2020) 1–11. URL: https://www.sciencedirect.com/science/article/pii/S0140700719303962. doi:https://doi.org/10.1016/j.ijrefrig.2019.09.011.

[120] C. Aprea, A. Greco, A. Maiorino, C. Masselli, A Numerical Investigation on a Caloric Heat Pump Employing Nanofluids, International Journal of Heat and Technology 37 (2019) 675–681.

[121] R. I. Epstein, K. J. Malloy, Electrocaloric devices based on thin-film heat switches, Journal of Applied Physics 106 (2009) 64509. URL: https://doi.org/10.1063/1.3190559. doi:10.1063/1.3190559.

[122] D. Feng, S. C. Yao, T. Zhang, Q. Zhang, Modeling of a smart heat pump made of laminated thermoelectric and electrocaloric materials, Journal of Electronic Packaging, Transactions of the ASME 138 (2016) 1–9. doi:10.1115/1.4034751.

[123] S. Hirasawa, T. Kawanami, K. Shirai, Electrocaloric Refrigeration using Multi-Layers of Electrocaloric Material Films and Thermal Switches, volume 39, 2018. doi:10.1080/01457632.2017.1358490.

[124] J. Gong, A. J. H. McGaughey, Device-level thermodynamic model for an electrocaloric cooler, International Journal of Energy Research 44 (2020) 5343–5359. URL: https://onlinelibrary.wiley.com/doi/abs/10.1002/er.5284. doi:https://doi.org/10.1002/er.5284.

[125] E. Stern-taulats, A. Gràcia-condal, A. Planes, P. Lloveras, M. Barrio, J.-l. Tamarit, Reversible adiabatic temperature changes at the magnetocaloric and barocaloric effects in Fe49Rh51 Reversible adiabatic temperature changes at the magnetocaloric and barocaloric effects in Fe 49 Rh 51 m (2015). URL: http://dx.doi.org/10.1063/1.4933409. doi:10.1063/1.4933409.

[126] C. R. Bahl, T. F. Petersen, N. Pryds, A. Smith, A versatile magnetic refrigeration test device, Review of Scientific Instruments 79 (2008). doi:10.1063/1.2981692.

[127] A. Rowe, A. Tura, Experimental investigation of a three-material layered active magnetic regenerator, International Journal of Refrigeration 29 (2006) 1286–1293. doi:`10.1016/j.ijrefrig.2006.07.012`.

[128] G. H. Yao, M. Q. Gong, J. F. Wu, Experimental study on the performance of a room temperature magnetic refrigerator using permanent magnets, International Journal of Refrigeration 29 (2006) 1267–1273. doi:`10.1016/j.ijrefrig.2006.07.010`.

[129] D. S. Arnold, A. Tura, A. Rowe, Experimental analysis of a two-material active magnetic regenerator, International Journal of Refrigeration 34 (2011) 178–191. URL: `http://dx.doi.org/10.1016/j.ijrefrig.2010.08.015`. doi:`10.1016/j.ijrefrig.2010.08.015`.

[130] M. Nickolay, H. Martin, Improved approximation for the Nusselt number for hydrodynamically developed laminar flow between parallel plates, International Journal of Heat and Mass Transfer 45 (2002) 3263–3266. doi:`10.1016/S0017-9310(02)00028-5`.

[131] K. Engelbrecht, A numerical model of an active magnetic regenerator refrigerator with experimental validation, Phd thesis, University of Wisconsin, Madison, USA, 2008.

[132] C. P. Jeffreson, Prediction of breakthrough curves in packed beds, AIChE J. 18 (1972) 409–420.

[133] K. L. Engelbrecht, G. F. Nellis, S. A. Klein, The effect of internal temperature gradients on regenerator matrix performance, Journal of Heat Transfer 128 (2006) 1060–1069. doi:`10.1115/1.2345428`.

[134] A. Šarlah, J. Tušek, A. Poredoš, Comparison of thermo-hydraulic properties of heat regenerators applicable to active magnetic refrigerators, Strojniski Vestnik/Journal of Mechanical Engineering 58 (2012) 16–22. doi:`10.5545/sv-jme.2010.250`.

[135] T. Lei, K. Engelbrecht, K. K. Nielsen, C. T. Veje, Study of geometries of active magnetic regenerators for room temperature magnetocaloric refrigeration, Applied Thermal Engineering 111 (2017) 1232–1243. URL: `http://dx.doi.org/10.1016/j.applthermaleng.2015.11.113`. doi:`10.1016/j.applthermaleng.2015.11.113`.

[136] R. Bjørk, C. R. Bahl, M. Katter, Magnetocaloric properties of $\mathrm{LaFe}_{13-x-y}\mathrm{Co}_x\mathrm{Si}_y$ and commercial grade Gd, Journal of Magnetism and Magnetic Materials 322 (2010) 3882–3888. doi:`10.1016/j.jmmm.2010.08.013`.

[137] S. Yu. Dan'kov, A. M. Tishin, V. K. Pecharsky, K. A. Gschneidner, Magnetic phase transitions and the magnetothermal properties of gadolinium, Physical Review B 57 (1998) 3478–3490.

[138] K. Engelbrecht, C. R. Bahl, K. K. Nielsen, Experimental results for a magnetic refrigerator using three different types of magnetocaloric material regenerators, International Journal of Refrigeration 34 (2011) 1132–1140. URL: `http://dx.doi.org/10.1016/j.ijrefrig.2010.11.014`. doi:`10.1016/j.ijrefrig.2010.11.014`.

[139] J. Tušek, A. Kitanovski, U. Tomc, C. Favero, A. Poredoš, Experimental comparison of multilayered La-Fe-Co-Si and single-layered Gd active magnetic regenerators for use in a room-temperature magnetic refrigerator, International Journal of Refrigeration 37 (2014) 117–126. URL: `http://dx.doi.org/10.1016/j.ijrefrig.2013.09.003`. doi:`10.1016/j.ijrefrig.2013.09.003`.

[140] P. Clot, D. Viallet, F. Allab, A. Kedous-Lebouc, J. M. Fournier, J. P. Yonnet, A Magnet-Based

Device for Active Magnetic Regenerative Refrigeration, IEEE Transactions on Magnetics 39 (2003) 3349–3351. doi:10.1109/TMAG.2003.816253.

[141] P. V. Trevizoli, J. R. Barbosa, R. T. Ferreira, Experimental evaluation of a Gd-based linear reciprocating active magnetic regenerator test apparatus, International Journal of Refrigeration 34 (2011) 1518–1526. doi:10.1016/j.ijrefrig.2011.05.005.

[142] M. Balli, O. Sari, C. Mahmed, C. Besson, P. Bonhote, D. Duc, J. Forchelet, A pre-industrial magnetic cooling system for room temperature application, Applied Energy 98 (2012) 556–561. URL: http://dx.doi.org/10.1016/j.apenergy.2012.04.034. doi:10.1016/j.apenergy.2012.04.034.

[143] X. N. He, M. Q. Gong, H. Zhang, W. Dai, J. Shen, J. F. Wu, Design and performance of a room-temperature hybrid magnetic refrigerator combined with Stirling gas refrigeration effect, International Journal of Refrigeration 36 (2013) 1465–1471. doi:10.1016/j.ijrefrig.2013.03.014.

[144] S. N. N. Hirano, S. Nagaya, M. Takahashi, T. Kuriyama, K. Ito, Development of magnetic refrigerator for room temperature application, in: AIP Conference Proceedings, volume 613, 2002. URL: http://dx.doi.org/10.1063/1.1472125. doi:10.1063/1.1472125.

[145] S. Hirano, T. Kawanami, K. Nakamura, A development of spherical-shaped magnetocaloric materials using powder coating method, Third IIF-IIR international conference on magnetic refrigeration at room temperature, Thermag I, Des Moines, Iowa, USA 97 (2009) 457–464.

[146] L. A. Tagliafico, F. Scarpa, F. Valsuani, G. Tagliafico, Preliminary experimental results from a linear reciprocating magnetic refrigerator prototype, Applied Thermal Engineering 52 (2013) 492–497. doi:10.1016/j.applthermaleng.2012.12.022.

[147] J. Tušek, A. Kitanovski, A. Poredoš, Geometrical optimization of packed-bed and parallel-plate active magnetic regenerators, International Journal of Refrigeration 36 (2013) 1456–1464. doi:10.1016/j.ijrefrig.2013.04.001.

[148] C. Aprea, A. Greco, A. Maiorino, C. Masselli, The energy performances of a rotary permanent magnet magnetic refrigerator, International Journal of Refrigeration 61 (2016) 1–11. URL: http://dx.doi.org/10.1016/j.ijrefrig.2015.09.005. doi:10.1016/j.ijrefrig.2015.09.005.

[149] K. Engelbrecht, D. Eriksen, C. R. Bahl, R. Bjørk, J. Geyti, J. A. Lozano, K. K. Nielsen, F. Saxild, A. Smith, N. Pryds, Experimental results for a novel rotary active magnetic regenerator, International Journal of Refrigeration 35 (2012) 1498–1505. doi:10.1016/j.ijrefrig.2012.05.003.

[150] A. Tura, A. Rowe, Permanent magnet magnetic refrigerator design and experimental characterization, International Journal of Refrigeration 34 (2011) 628–639. URL: http://dx.doi.org/10.1016/j.ijrefrig.2010.12.009. doi:10.1016/j.ijrefrig.2010.12.009.

[151] O. Ando Junior, A. Maran, N. Henao, A review of the development and applications of thermoelectric microgenerators for energy harvesting, Renewable and Sustainable Energy Reviews 91 (2018) 376–393. URL: https://www.sciencedirect.com/science/article/pii/S1364032118301394. doi:https://doi.org/10.1016/j.rser.2018.03.052.

[152] Photovoltaic materials: Present efficiencies and future challenges, Science 352 (2016) aad4424. URL: https://www.science.org/doi/

abs/10.1126/science.aad4424. doi:10.1126/science.aad4424. arXiv:https://www.science.org/doi/pdf/10.1126/science.aad4424.

[153] A. LaPotin, K. L. Schulte, M. A. Steiner, K. Buznitsky, C. C. Kelsall, D. J. Friedman, E. J. Tervo, R. M. France, M. R. Young, A. Rohskopf, S. Verma, E. N. Wang, A. Henry, Thermophotovoltaic efficiency of 40%, Nature 604 (2022) 287–291. URL: https://doi.org/10.1038/s41586-022-04473-y. doi:10.1038/s41586-022-04473-y.

[154] S. P. Alpay, J. Mantese, S. Trolier-Mckinstry, Q. Zhang, R. W. Whatmore, Next-generation electrocaloric and pyroelectric materials for solid-state electrothermal energy interconversion, MRS Bulletin 39 (2014) 1099–1109. doi:10.1557/mrs.2014.256.

[155] G. Sebald, S. Pruvost, D. Guyomar, Energy harvesting based on Ericsson pyroelectric cycles in a relaxor ferroelectric ceramic, Smart Materials and Structures 17 (2007) 15012. URL: https://doi.org/10.1088/0964-1726/17/01/015012. doi:10.1088/0964-1726/17/01/015012.

[156] D. G. Frood, A NOTE ON THE USE OF THE TITANATES AS THERMOELECTRIC TRANSDUCERS, Canadian Journal of Physics 32 (1954) 313–317. URL: https://doi.org/10.1139/p54-029. doi:10.1139/p54-029.

[157] R. B. Olsen, D. Evans, Pyroelectric energy conversion: Hysteresis loss and temperature sensitivity of a ferroelectric material, Journal of Applied Physics 54 (1983) 5941–5944. URL: https://doi.org/10.1063/1.331769. doi:10.1063/1.331769.

[158] K. Song, R. Zhao, Z. L. Wang, Y. Yang, Conjuncted pyro-piezoelectric effect for self-powered simultaneous temperature and pressure sensing, Advanced Materials 31 (2019) 1902831. URL: https://onlinelibrary.wiley.com/doi/abs/10.1002/adma.201902831. doi:https://doi.org/10.1002/adma.201902831. arXiv:https://onlinelibrary.wiley.com/doi/pdf/10.1002/adma.201902831.

[159] K. Song, N. Ma, Y. K. Mishra, R. Adelung, Y. Yang, Achieving light-induced ultrahigh pyroelectric charge density toward self-powered uv light detection, Advanced Electronic Materials 5 (2019) 1800413. URL: https://onlinelibrary.wiley.com/doi/abs/10.1002/aelm.201800413. doi:https://doi.org/10.1002/aelm.201800413. arXiv:https://onlinelibrary.wiley.com/doi/pdf/10.1002/aelm.201800413.

[160] K. Zhang, Y. Wang, Z. L. Wang, Y. Yang, Standard and figure-of-merit for quantifying the performance of pyroelectric nanogenerators, Nano Energy 55 (2019) 534–540. URL: https://www.sciencedirect.com/science/article/pii/S2211285518308322. doi:https://doi.org/10.1016/j.nanoen.2018.11.020.

[161] Y. Xu, Ferroelectric materials and their applications, Elsevier, 2013.

[162] A. Khodayari, S. Pruvost, G. Sebald, D. Guyomar, S. Mohammadi, Nonlinear pyroelectric energy harvesting from relaxor single crystals, IEEE transactions on ultrasonics, ferroelectrics, and frequency control 56 (2009) 693–699. doi:10.1109/TUFFC.2009.1092.

[163] A. Navid, L. Pilon, Pyroelectric energy harvesting using Olsen cycles in purified and porous poly(vinylidene fluoride-trifluoroethylene) [P(VDF-TrFE)] thin films, Smart Materials and Structures 20 (2011) 25012. URL: https://doi.org/10.1088/0964-1726/20/2/025012. doi:10.1088/0964-1726/20/2/025012.

[164] J. Kim, S. Yamanaka, I. Murayama, T. Katou, T. Sakamoto, T. Kawasaki, T. Fukuda, T. Sekino,

T. Nakayama, M. Takeda, M. Baba, H. Tanaka, K. Aizawa, H. Hashimoto, Y. Kim, Pyroelectric power generation from the waste heat of automotive exhaust gas, Sustainable Energy Fuels 4 (2020) 1143–1149. URL: http://dx.doi.org/10.1039/C9SE00283A. doi:10.1039/C9SE00283A.

[165] F. Y. Lee, S. Goljahi, I. M. McKinley, C. S. Lynch, L. Pilon, Pyroelectric waste heat energy harvesting using relaxor ferroelectric 8/65/35 PLZT and the Olsen cycle, Smart Materials and Structures 21 (2012) 25021. URL: https://doi.org/10.1088/0964-1726/21/2/025021. doi:10.1088/0964-1726/21/2/025021.

[166] R. B. Olsen, D. A. Bruno, J. M. Briscoe, J. Dullea, Cascaded pyroelectric energy converter, Ferroelectrics 59 (1984) 205–219. URL: https://doi.org/10.1080/00150198408240091. doi:10.1080/00150198408240091.

[167] Q. M. Zhang, T. Zhang, The refrigerant is also the pump, Science 357 (2017) 1094–1095. URL: https://www.science.org/doi/abs/10.1126/science.aao2438. doi:10.1126/science.aao2438. arXiv:https://www.science.org/doi/pdf/10.1126/science.aao2438.

[168] L. Fulanović, J. Koruza, N. Novak, F. Weyland, B. Malič, V. Bobnar, Fatigue-less electrocaloric effect in relaxor $Pb(Mg_{1/3}Nb_{2/3})O_3$ multilayer elements, Journal of the European Ceramic Society 37 (2017) 5105–5108. URL: https://www.sciencedirect.com/science/article/pii/S095522191730434X. doi:https://doi.org/10.1016/j.jeurceramsoc.2017.06.011.

[169] M. G. Del Duca, J. Tušek, A. Maiorino, L. Fulanović, A. Bradeško, U. Plaznik, B. Malič, C. Aprea, A. Kitanovski, Comprehensive evaluation of electrocaloric effect and fatigue behavior in the 0.9pb(mg1/3nb2/3)o3–0.1pbtio3 bulk relaxor ferroelectric ceramic, Journal of Applied Physics 128 (2020) 104102. URL: https://doi.org/10.1063/5.0003250. doi:10.1063/5.0003250. arXiv:https://doi.org/10.1063/5.0003250.

[170] G. Zhang, L. Weng, Z. Hu, Y. Liu, R. Bao, P. Zhao, H. Feng, N. Yang, M.-Y. Li, S. Zhang, S. Jiang, Q. Wang, Nanoconfinement-induced giant electrocaloric effect in ferroelectric polymer nanowire array integrated with aluminum oxide membrane to exhibit record cooling power density, Advanced Materials 31 (2019) 1806642. URL: https://onlinelibrary.wiley.com/doi/abs/10.1002/adma.201806642. doi:https://doi.org/10.1002/adma.201806642. arXiv:https://onlinelibrary.wiley.com/doi/pdf/10.1002/adma.201806642.

[171] H. Cui, Q. Zhang, Y. Bo, P. Bai, M. Wang, C. Zhang, X. Qian, R. Ma, Flexible microfluidic electrocaloric cooling capillary tube with giant specific device cooling power density, Joule 6 (2022) 258–268. URL: https://www.sciencedirect.com/science/article/pii/S2542435121005791. doi:https://doi.org/10.1016/j.joule.2021.12.010.